DISSERTATION

ACTIVE RADIATION DETECTORS FOR USE IN SPACE BEYOND LOW EARTH ORBIT: SPATIAL AND ENERGY RESOLUTION REQUIREMENTS AND METHODS FOR HEAVY ION CHARGE CLASSIFICATION

Submitted by

Rafe A. McBeth

Department of Environmental and Radiological Health Sciences

In partial fulfillment of the requirements

For the Degree of Doctor of Philosophy

Colorado State University

Fort Collins, Colorado

Summer 2017

Doctoral Committee:

Advisor: Thomas Borak

Alexander Brandl
Andrew Ray
Darren Homrighausen

ABSTRACT

ACTIVE RADIATION DETECTORS FOR USE IN SPACE BEYOND LOW EARTH ORBIT: SPATIAL AND ENERGY RESOLUTION REQUIREMENTS AND METHODS FOR HEAVY ION CHARGE CLASSIFICATION

Space radiation exposure to astronauts will need to be carefully monitored on future missions beyond low earth orbit. NASA has proposed an updated radiation risk framework that takes into account a significant amount of radiobiological and heavy ion track structure information. These models require active radiation detection systems to measure the energy and ion charge Z.

However, current radiation detection systems cannot meet these demands. The aim of this study was to investigate several topics that will help next generation detection systems meet the NASA objectives. Specifically, this work investigates the required spatial resolution to avoid coincident events in a detector, the effects of energy straggling and conversion of dose from silicon to water, and methods for ion identification (Z) using machine learning.

The main results of this dissertation are as follows: 1. Spatial resolution on the order of 0.1 cm is required for active space radiation detectors to have high confidence in identifying individual particles, i.e., to eliminate coincident events. 2. Energy resolution of a detector system will be limited by energy straggling effects and the conversion of dose in silicon to dose in biological tissue (water). 3. Machine learning methods show strong promise for identification of ion charge (Z) with simple detector designs.

ACKNOWLEDGEMENTS

I would like to thank Dr. Thomas Borak for allowing me to participate in his group at Colorado State University. Dr. Borak has forever changed my life and greatly contributed to my scientific development. He inspires me to be a better scientist and it has been a great honor to work with him over these years. I would also like to thank Dr. Alexander Brandl for always being there for me to talk with and for his very careful and thoughtful review of this dissertation. I also want to thank Dr. Thomas Johnson for his constant support over my graduate school career. He always found a way to help me, even when he told me he might not be able to. Finally, I would like to thank Dr. Susan LaRue for allowing me to work with her group in the Radiation Oncology Department at the CSU Veterinary Teaching Hospital. My time with Dr. LaRue confirmed and grew my passion for medical physics and I wouldn't be on the path I am without her help.

A special thanks to my wife, Carly, who has stood by my side for all of this journey. We have built a beautiful family over these years and I will never forgot all the fun we had together in Fort Collins. To my daughter, Emery for always making me smile and laugh when I was at home, and to our newest addition Harlow for giving me strong motivation to finish this project before she arrived.

I would also like to thank my parents, Roger and Kathy, for their constant support over the years. You have always believed in my abilities and gave me the confidence to chase my dreams. To my extended family, you have all helped to mold who I am as a person in your own way. Although I often lose myself in my work, you are always in my thoughts and I'm thankful to have you in my life.

I am also very grateful to all the students and staff in the ERHS department that I have worked with over the years. You have all contributed to my growth in one way or another. I am particularly grateful for John Brogan and the friendship we have built over the years. Beating you at video games and basketball has always been great fun and a welcome distraction from hard work.

DEDICATION

To my amazing wife, Carly, for her unwavering support, it would have been impossible to complete this without you by my side. To my daughters, Emery and Harlow, being your dad will always be my greatest achievement.

TABLE OF CONTENTS

LIST OF TABLES

LIST OF FIGURES

Chapter 1

Introduction

Long duration missions in space, such as a mission to Mars, will expose astronauts to radiation from high energy (E $>$ 20 MeV/n) and high atomic number (Z $\geq$ 2) heavy ions (HZE) at historically high levels. Heavy ion radiotherapy is also being used increasingly to treat malignant tumors using a subset of HZE particles. As these ions pass through materials, they deposit energy in complex ways. Radiation detection systems that accurately measure HZE ions to determine radiation dose to astronauts or patients are essential for future space missions and the expansion of heavy ion therapy treatments. In fact, NASA has defined the development of a compact radiation detector capable of determining energy and charge of incident radiation as a major technical challenge for future manned space missions (Hurlbert et al., 2012).

The radiation environment in space is composed of two major components, solar particle events (SPE) and galactic cosmic rays (GCR). SPE are composed of 98% protons, 1% helium and 1% other HZE ions and their flux can vary significantly over time. GCR are composed of 87% protons, 12% helium ions and 1% HZE ions. GCR orginate from outside the solar system and will be omnidirectionally incident on astronauts. While the fluence of ions in space with charge $Z > 2$ is only 1% of the GCR spectrum, these high Z ions contribute significantly to the radiation dose. The high Z ion component of the radiation environment in space is the primary focus of this study.

As heavy ions travel through a medium they transfer energy primarily through electromagnetic interaction. Ionization and excitation are the two main electromagnetic processes by which space radiation loses energy. Ionization occurs when an incident heavy ion transfers sufficient energy to strip an orbiting electron from an atom or molecule in a material. Energy transferred below the threshold for ionization excites the atom or molecule in the target material and can lead to subsequent de-excitation. For HZE ions, nuclear (strong force) interactions with the nuclei of the target material are also possible. Nuclear interactions produce many secondary fragments that originate from the incident ion (projectile) or the target material. Although the probability of nuclear in-

teraction is low, when compared to electromagnetic interaction, the effects of fragmentation on the radiation field can be significant. In hadron radiation therapy applications, up to 80% of an incident carbon ion beam has fragmented by the time it reaches a depth of 10 cm in water (McBeth and Borak, 2015). For space applications, Le Tessa et al. found that 68% of a 1 GeV/nucleon iron beam has fragmented after 9.6 cm of aluminum (La Tessa et al., 2005).

HZE ions are believed to have qualitatively and quantitatively different effects on biological systems when compared to the natural radiation background found on earth (Durante, 2014). Moreover, less information is available about the effects that space radiation has on humans due to the small number of individuals exposed. An important risk to astronauts from space radiation is the induction of cancer. Non-cancer effects, such as damage to the central nervous system (CNS) and late cardiovascular disease are of increasing concern and have large uncertainties in the estimated risk (Durante and Cucinotta, 2008). Data also suggest that heavy ions cause damage through non-targeted effects (Durante, 2012). The assessment of radiation risk for both acute and late effects, will be essential for ensuring the health and safety of astronauts. The National Committee on Radiation Protection (NCRP) and NASA have published many documents on the appropriate methods for radiation protection in space (Cucinotta et al., 2013; NCRP, 1989, 2002, 2006, 2014).

Radiation protection in space is focused on ensuring short and long term effects of radiation are limited to acceptable levels. A quality factor, Q, is a factor that modifies the absorbed radiation dose based on biological effectiveness, and is an important concept in radiation protection. Historically Q has depended on the measured spectra of linear energy transfer (LET). In preparation for space missions beyond low earth orbit, significant efforts have been directed towards updating quality factors to more accurately reflect the biological damage HZE particles cause (Cucinotta et al., 2013). This revised quality factor, Q_{NASA}, requires future detection systems to not only measure the LET but also the charge Z and velocity β of HZE ions. However, detector systems deployed into space have a limited ability to measure individual particle charge and velocity, and do not provide sufficient information for the accurate determination of radiation risk to astronauts under the new NASA paradigm.

To meet the requirements of the new NASA quality factor, future detection systems will need to have appropriate spatial resolution to ensure properties of individual particles, such as LET or the charge Z, are correctly identified. In practice, the spatial resolution of a detection system will be defined by the segmentation or pixelation of the detector e.g., a detector with a pixel size of 1 cm will also have a spatial resolution of 1 cm. Coincident events from the primary GCR spectrum are rare, due to the low fluence, but secondary projectile fragments emerge from shielding with similar velocities and are grouped in space and time. Grouped particles intercepting a radiation detector simultaneously will register the sum of the energy deposition, introducing errors into the measured energy spectrum. A detection system must have the spatial resolution capable of ensuring that only single heavy ion events are recorded. The ability of a detector to identify individual particles will be defined as the spatial resolution in this paper.

A radiation detector with sufficient spatial resolution to measure individual particles will also require sufficient energy resolution. Detection systems that use thin silicon radiation detectors, such as the Radiation Assessment Detector (RAD) currently mounted on the Mars Curiosity rover and the detector system evaluated in this study, will have limited energy resolution. This limited energy resolution is due to the statistical variation in energy deposited as a heavy ion passes through a thin detector. Although small energy transfers in a thin detector are most common, infrequent large energy transfers can result in significant energy loss and add large uncertainty to the determination of particle stopping power. This phenomenon is referred to as energy straggling. Energy straggling will limit the ability of a detector to identify a particles' charge (Z) and velocity (β) as required by the NASA quality factor.

In addition to spatial and energy resolution of a detector system, conversion of measured energy deposition in a detector to biologically relevant materials must be considered. Specifically, a silicon radiation detection system that measures stopping power will have to be converted to stopping power in water. Historically, radiation detection systems have used a single factor to scale stopping power in Si to LET in water (Zeitlin et al., 2013). Uncertainties that result from this conversion will propagate to the dose, dose equivalent values and ultimately assessment of risk.

To investigate the spatial resolution, energy resolution, and stopping power conversion factors required, experiments were simulated using Monte Carlo radiation transport methods. For these studies a subset of the space radiation spectrum, specifically He, C, Si, and Fe, were directed at aluminum shields of varying thickness, 2, 5, and 10 cm. To investigate the spatial resolution required for detectors used beyond low Earth orbit, a idealized detector system with a virtual detector was used, while a physical detector system, using a 300 μm silicon real detector, was used for the study of energy resolution and stopping power conversion factors.

A virtual detector in this context is a plane downstream from the shielding that scores the primary and fragment ions as they intercept the plane, but do not interact with the particles. Incident ions are directed normally at the shield and the position of the transmitted are recorded as they intercept the virtual detector. A novel analysis method, leading to proximity distributions, was used to evaluate the data and determine what spatial resolution requirements are necessary to satisfy the demands of the mission. Proximity distributions provide the probability that more than one particle will intercept the same pixel for a given pixel size. These distributions can then be used to determine the pixel size necessary to achieve a desired level of confidence in measuring individual particles. The stopping power distributions of the virtual detector system and an unsegmented detector system are presented to assess the impact that coincident events may have had on non pixelated detectors in the past.

The next step was to investigate the effects of energy straggling, assuming the detection system is appropriately segmented. Simulations were performed with a physical detector system, i.e., a 300 μm thin silicon real detector. Stopping power distributions are created that show the difference between the idealized detector system and the physical detector system, with energy straggling. Additionally, metrics such as the dose mean stopping power are compared to evaluate the difference between an ideal detection system and a real detection system. Energy straggling in a thin detector system cannot be mitigated. Thus, a thorough understanding of energy straggling will be necessary for the identification of the distribution of Z and β in the radiation environment.

The next goal of this work was to determine if it is possible, using the simplistic detector design of the energy straggling studies, to accurately identify the charge Z of ions in the radiation environment. To do this, methods of the fast growing field of machine learning were used. A machine learning algorithm is a computational process that attempts to "learn" how to achieve the desired goal. These algorithms emulate human intelligence by learning from its surroundings and have become crucial in the era of "big data". These techniques have been successfully applied to self-driving cars, robot tasks, pattern recognition, computer vision, finance, computational biology, and medical applications. In this paper, we present applications of machine learning techniques to the problem of ion classification.

To summarize, this paper provides results for four main questions about the general characteristics a detection system will need to identify Z, β, and the linear energy transfer of individual particles that contribute to space radiation dose. The questions are:

1. What spatial resolution (pixel size) is required for a radiation detection system to have high confidence that only one heavy ion is measured?

2. To what extent does energy straggling change the measurement of stopping power spectra?

3. Is a single scaling factor appropriate for converting stopping power in a Si detector to stopping power in water?

4. Is it possible to use machine learning techniques to identify the charge Z of individual particles using a simplistic radiation detection system?

Outline of Dissertation

- The basic principles of radiation interaction and the fundamentals of radiation protection are discussed in Chapter 2. These sections also introduce radiation detection methods that have been used in previous missions.

- Monte Carlo radiation transport techniques and the general experimental design used for these simulations are described in Chapter 3.

- Simulation output analysis methods and results for the determination of optimum radiation detector pixel size are discussed in Chapter 4.

- Energy resolution for a basic detection system is analyzed in Chapter 5. This includes how energy straggling affects estimates of LET, and issues that arise from the conversion of stopping power in silicon to stopping power in water.

- Machine learning methods for ion classification, i.e., identification of Z, are discussed in Chapter 6.

Chapter 2

Space radiation physical principles and protection

2.1 Physical principles of radiation

As radiation interacts with a medium, it can lose energy in numerous ways depending on the type of incident radiation. X, γ, and heavy ion radiation transfer energy to the medium by the process of excitation and ionization. Ionization is the removal of bound electrons from the target atoms or molecules. Excitation is process of the incident radiation imparting energy on an atom or molecule and leaving it in a excited state.

Ionization can be indirect or direct. Indirect ionization occurs when non charged radiation, such as photons and neutrons, liberate charged particles such as electrons. It is also possible for these ionized electrons to create their own ionizations. When electrons act as ionizing particles they are often called delta rays. Charged particles such as electrons, protons, alpha particles, and heavier nuclei are directly ionizing. The rate at which heavy charged particles lose energy per unit length (dE/dx) is the stopping power (S), and is discussed in detail in Section 2.1.2. Linear energy transfer (LET) is related to stopping power but has the distinct difference that it is a measure of the energy absorbed in a medium, not the energy lost by the particle, as in the definition of stopping power. LET is discussed in more detail in Section 2.1.3.

2.1.1 Fundamental Quantities

Several fundamental quantities have been defined to quantify the physical nature of radiation. Quantities have also been developed to quantify how radiation interacts with a medium such as human tissue.

The amount of radiation incident on an object is described using the fluence. Fluence, Φ, is defined as:

$$\Phi = \frac{dN}{da}. \tag{2.1}$$

Where dN is the number of particles incident on a sphere of cross-sectional area da and the unit is often given in particles cm^{-2} (ICRU, 1993). The rate at which particles are incident is the fluence rate and is the fluence of particles per unit time,

$$\dot{\Phi} = \frac{\Phi}{dt} = \frac{dN}{dadt}, \tag{2.2}$$

where dt is a unit time, such as 1 hour. The unit of fluence rate is particles $\mathrm{cm}^{-2}\,\mathrm{s}^{-1}$.

Over the years, methodologies to describe the effects of radiation and the associated risk have been developed. Two fundamental ideas are the constructs of absorbed dose and dose equivalent.

Absorbed dose is a fundamental concept of radiation dosimetry and is a measure of the amount of energy imparted to a medium by all types of radiation. The absorbed dose, D, is defined as the average energy absorbed per unit mass of a target for ionizing radiation (ICRU, 2011). The SI unit for absorbed dose is $\mathrm{J\,kg}^{-1}$ and has the special name gray (Gy) or the traditional name rad. The relationship between gray (Gy) and rad is

$$1\,\mathrm{Gy} = 100\,\mathrm{rad}. \tag{2.3}$$

Absorbed dose is a point function, has a value at every position in an irradiated volume and is the quotient of $d\bar{\epsilon}$ by dm,

$$D = \frac{d\bar{\epsilon}}{dm}, \tag{2.4}$$

where $d\bar{\epsilon}$ is the mean energy imparted by ionizing radiation to matter of mass dm (ICRU, 1993). Alternatively, the absorbed dose can be written as

$$D = \Phi \cdot \frac{\mathrm{LET}}{\rho}, \tag{2.5}$$

where Φ is the fluence, LET is the linear energy transfer of the ion, and ρ is the density of the medium. In this alternative form, the units in the equation need to be appropriately converted to get to the unit of gray.

Dose equivalent, H, is an additional construct that takes into account the fact that some particles are more damaging and have higher associated risk than the standard radiation, 200 keV photons. Dose equivalent is defined as the product of absorbed dose, D, and a dimensionless quality factor Q,

$$H = D \cdot Q. \tag{2.6}$$

The concept of dose equivalent is applicable only to human beings and has the same physical dimensions as absorbed dose, $\mathrm{J\,kg^{-1}}$, but has the different SI unit of the sievert (Sv) or the traditional unit rem. The relationship between sievert (Sv) and rem is

$$1\,\mathrm{Sv} = 100\,\mathrm{rem} \tag{2.7}$$

The quality factor and associated radiation protection limits will be discussed in more detail in Section 2.3.

2.1.2 Stopping power

Hadrons, such as the heavy ions found in GCR, lose their energy primarily by Coulomb force interaction (ionizations and excitations) but also have the potential to have nuclear reactions. The rate at which heavy charged particles lose energy per unit length (dE/dx) by interaction with electrons of the medium is defined as the stopping power (S) and to a first approximation is given by the Bethe-Bloch equation:

$$S = -\frac{dE}{dx} = \frac{4\pi k_0^2 Z^2 e^4 n}{mc^2\beta^2}\left[\frac{2mc^2\beta^2}{I(1-\beta^2)} - \beta^2\right]. \tag{2.8}$$

In equation 2.8

$$k_0 = 8.99 \times 10^9\,\mathrm{N\,m^2C^{-2}},$$

$Z =$ atomic number of heavy ion,

$e =$ electron charge,

$n =$ electrons per unit volume of medium,

$m =$ electron rest mass,

$c =$ speed of light in vacuum,

$\beta = V/c =$ speed of particle relative to c

$I =$ mean excitation energy of the medium

Equation 2.8 shows that the stopping power is dependent on the velocity (β) and charge (Z) of the incident ion and the properties of the medium. Equation 2.8 considers the energy lost by ionization but does not consider nuclear interactions.

2.1.3 Linear Energy Transfer (LET)

Linear energy transfer (LET) is distinctly different from stopping power discussed in Section 2.1.2. While stopping power is the energy lost by the particle as it travels through a medium, dE/dx, LET can be considered as the energy absorbed by the medium. Original definitions of LET only considered the radiation absorbed within a specific radial distance or maximum electron energy. This definition of LET excluded the contribution of delta rays that deposit dose at a distance from the central track of a heavy ion. For large volumes where these secondary high energy delta rays (electrons) are fully absorbed, LET and stopping power are equivalent. In smaller volumes, such as biological cells, the difference between the energy lost by an incoming ion and the energy deposited in the small volume can be significant. Additionally, similar to stopping power, the LET is considered to be an averaged quantity at a point, and thus is not representative of statistical fluctuations in the deposited energy.

LET or linear energy transfer is generally defined as the energy transferred per unit path length of the track. However the definition has undergone subtle changes over the years. The 1970 ICRU report no. 16 titled Linear Energy Transfer ICRU (1970) defined it as:

> The linear energy transfer or restricted linear collision stopping power (L_Δ) of charged particles in a medium is the quotient of dE by dl, where dl is the distance traversed by the particle and dE is the mean energy-loss due to collisions with energy transfers less than some specified value Δ.

$$L_\Delta = \left(\frac{dE}{dl}\right)_\Delta$$

ICRU Report 85a (ICRU, 2011) defines the linear energy transfer or restricted linear electronic stopping power, L_Δ, of a material as

$$L_\Delta = \frac{dE_\Delta}{dl}.$$

Where dE_Δ is the mean energy lost by the charged particles due to electronic interactions in traversing a distance dl, minus the mean sum of the kinetic energies in excess of Δ of all the electrons released by the charged particles. This can also be written as

$$L_\Delta = S_{el} - \frac{dE_{ke,\Delta}}{dl},$$

where S_{el} is the linear electronic stopping power, and $dE_{ke,\Delta}$ is the mean sum of the kinetic energies, greater than Δ, of all the electrons released by the charged particle in traversing a distance dl. It is important to note that the binding energies for all collisions are included in the definition. ICRU report 85a further describes the energy balance as:

> Energy lost by the primary charged particle in interactions with electrons, along a distance dl, minus the energy carried away by energetic secondary electrons having initial kinetic energies greater than Δ, equals energy considered as "locally transferred".

The unrestricted LET, L_∞, is the linear energy transfer considering no energy cutoff. This is equivalent to the electronic stopping power. LET is used to determine the quality or effectiveness of radiation in the human body and is a dependent variable in the concept of Relative Biological Effectiveness (RBE).

2.1.4 Nuclear fragmentation

High energy ions have sufficient energy to overcome Coulomb forces and interact with the nucleus of target material atoms. The nuclear cross section for these interactions is small and negligible in thin materials. However, for thick materials, such as space craft, habitat shielding, or patients in heavy ion therapy, nuclear reactions cannot be ignored. Nuclear fragmentation is the process by which heavy ions interact with a medium and produce secondary nuclei (fragments). Fragments can originate from both the incident ion and the target material. These fragments will be grouped temporally and spatially.

Fragments simultaneously impacting a detection system will register as a single event and distort the resultant distributions of stopping power and estimates of risk. Future detection systems should be designed to eliminate these simultaneous or coincident events and accurately measure individual particles.

2.1.5 Energy straggling

As described in Section 2.1.2, stopping power is an averaged quantity and does not include the statistical fluctuations in energy lost. For thick absorbers, the variation in energy loss can be described by a symmetric distribution. In thin absorbers, where the energy lost in the material is small in comparison to the total energy of the incident particles, the distribution can be highly skewed. The energy lost in a collision with a single electron, ϵ, is proportional to $1/\epsilon^2$. This implies that small energy transfers are far more common than large energy transfers. Although large energy transfers are infrequent, they can account for a large proportion of the total energy loss.

There are several theories that describe the probability distribution of energy loss when heavy charged particles pass through a thin absorber. The various theories for energy straggling are summarized well in a paper by Maccabee et al. (Maccabee et al., 1968). When the the number of collisions of a heavy ion in an absorber is large, i.e., a thick absorber, Bohr showed that the energy loss probability distribution is Gaussian (Bohr, 1915). The mean of this distribution is given by the Bethe-Bloch function, Equation 2.8 of Section 2.1.2. The variance for this Gaussian distribution is given by

$$\sigma^2 = 4\pi e^4 Z^2 N z x, \tag{2.9}$$

where e is the electron charge, Z is the incident heavy ion charge number, N is the number of atoms/cm^3 of the absorber material, z is the atomic number of the material and x is the absorber thickness. Equation 2.9 is appropriate when the number of energy deposition events in each possible energy range is large. Mathematically Equation 2.9 is valid when

$$\xi/\epsilon_{\text{max}} >> 1, \tag{2.10}$$

where

$$\xi = 2\pi e^4 Z^2 N z x / m v^2, \tag{2.11}$$

and m is the electron mass, v is the particle velocity and ϵ_{max} is the maximum possible energy transfer in a heavy ion-electron collision. Non-relativistically the maximum possible energy a heavy ion can transfer to an electron is

$$\epsilon_{\text{max}} = 2mv^2/(1-\beta^2), \tag{2.12}$$

where $\beta = v/c$.

The opposite case is when the number of collisions in the highest energy range is small, i.e.,

$$\xi/\epsilon_{\text{max}} << 1. \tag{2.13}$$

Landau solved this case in 1944 and showed that the probability distribution of energy losses is highly asymmetric with a broad peak around the most probable energy loss and a long tail (Landau, 1944). The full width at half-maximum (FWHM) was given as

$$FWHM = 3.98\xi. \tag{2.14}$$

In these cases the most probable energy loss, Δ_{mp}, is much lower than the average energy loss, Δ_{av}, given by Bohr. The most probable energy loss is given as

$$\Delta_{mp} = \xi \ln[2mv^2\xi/I^2(1-\beta^2)] - \beta^2 + 0.37, \tag{2.15}$$

where I is the mean excitation potential of the material. For reference, the mean excitation relevant to this work are 75 eV for water and 173 eV for silicon.

Vavilov treated the case in between Landau and Bohr in 1957 (Maccabee et al., 1968; Vavilov, 1957). Vavilov's method gave a family of curves based on the parameter κ, which was dependent on β^2 and Z and is defined as

$$\kappa = \xi/\epsilon_{\text{max}} = 0.150 s Z^2 z(1-\beta^2)/A\beta^4, \tag{2.16}$$

where Z is the charge of the incident particle, β is the velocity of the particle, s is the absorber thickness in g/cm^2, z is the atomic number of the material and A is the atomic weight.

2.2 Biological effects of radiation

The long term effects on humans from GCR, when compared to terrestrial radiation, are suspected to be quantitatively and qualitatively different (Cucinotta, 2014). A main health concern for these particles is increased fatal cancer risk of the astronaut once they return to earth. Additional non-cancer risks include damage to the central nervous system (CNS), cardiovascular disease and

cataracts. Acute neurological effects could affect how the astronauts perform during important missions. In extreme cases, a large solar particle event could cause radiation sickness and death.

Relative Biological effectiveness (RBE) has been used in radiation oncology, radiobiology, and radiation protection to compare the damage done by different types of radiation. In radiobiology, RBE is defined as the inverse ratio of the doses of two kinds of radiation that produce the same biological effect (Committee et al., 1963). The biological system, endpoint, reference radiation used, dose-rate, fractionation must be well defined in a statement of RBE. For radiation protection purposes, RBE is only used in terms of derived quantities such as quality factor, $Q(LET)$.

2.3 Quality Factor and Radiation Protection

The definition of the quality factor Q has undergone several changes since its introduction in 1977 by the Internation Commission on Radiologial Protection (ICRP). ICRP publication 26, published in 1977, defined the quality factor in terms of the unrestricted stopping power in water at a point, LET_∞. The relationship between LET_∞ and Q is shown in Table 2.1 and Figure 2.1 (ICRP, 1977). The relationship between quality factor and LET was somewhat arbitrary and was not meant to be a quantity with high precision. In 1990 the ICRP revised the LET dependent quality factor to take into account new biological information. The updated quality factor is given in Table 2.2 and shown in Figure 2.1 (ICRP, 1990).

Table 2.1: ICRP 26, 1977, Quality factor as a function of LET_∞

LET (keV/μm in water)	Quality factor
< 3.5	1
7	2
23	5
53	20
> 175	20

The concept of dose equivalent, H, which is the absorbed dose scaled by the quality factor (2.6), was used to define radiation protection standards. Radiation dose limits for terrestrial activities

Table 2.2: ICRP 60, Quality factors as a function of LET_∞

LET (keV/μm in water)	Quality factor
< 10	1
10 - 100	$0.32L - 2.2$
> 100	$300/\sqrt{LET}$

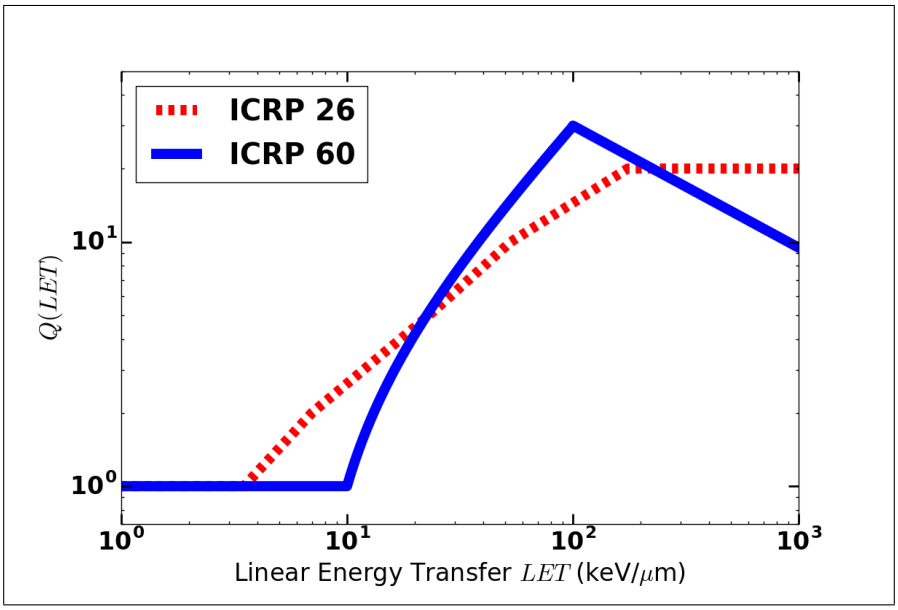

Figure 2.1: Graphical representation of the quality factor as defined by the ICRP 26 (Table 2.1) and ICRP 60 (Table 2.2). Quality factor is shown as a function of unrestricted LET, LET_∞. Adapted from ICRP 92 Figure 1.1 (ICRP, 2003)

have been proposed in numerous reports (ICRP, 1977, 1990, 2003; NCRP, 1993). In 1977, ICRP recommended an annual whole body dose equivalent limit of 50 mSv (5 rem) to reduce stochastic effects (ICRP, 1977). In 1990, ICRP revised the whole body dose limits to include stochastic and non-stochastic effects, setting the recommended limit at 20 mSv/yr effective dose (ICRP, 1990). Regulatory agencies base their radiation dose limits on these reports for terrestrial radiation safety.

2.4 Space Radiation Environment

The radiation environment outside of the Earth's atmosphere is unique and complex, consisting of three major components: solar particle event (SPE), galactic cosmic radiation (GCR), and trapped radiation belts. Trapped radiation belts are predominantly protons and electrons trapped

by the Earth's magnetic field. These radiation belts are directed to the poles of Earth and are the source of particles for the polar auroras. As astronauts travel beyond low Earth orbit (LEO), the radiation environment consists of only two primary components; galactic cosmic radiation (GCR) and solar particle event (SPE).

2.4.1 Solar Particle Event (SPE)

SPE are primarily composed of protons with energies in the range of one to several hundred MeV. SPE originate from the sun and are caused by coronal mass ejections and solar flares (NCRP, 2006). SPE frequency varies with solar cycle with most occurring during solar maximum. On average 5 to 10 events per year are observed from LEO. SPE can cause potentially lethal radiation exposures to astronauts and are difficult to predict.

Solar particle events can vary greatly in duration and fluence. SPE with proton energies greater than 30 MeV and fluences of 10^7 per cm^2 are of importance for radiation protection (Cucinotta et al., 2013). Over a 60 year period there were 13 SPE with protons exceeding 30 MeV and with fluences of 10^9 protons per cm^2 (Cucinotta et al., 2013).

While most SPE have low dose rates, rare SPE have been observed that are capable of delivering dose rates to astronauts on interplanetary missions over the low dose rate criteria of $< 0.1\ \mathrm{Gy\,hr^{-1}}$, established by the International Commission of Radiological Protection (ICRP) (Parsons and Townsend, 2000).

2.4.2 Galactic Cosmic Rays (GCR)

Galactic cosmic radiation originates from outside the solar system and will be incident on astronauts isotropically, i.e. the fluence does not vary according to the direction of measurement. This galactic cosmic radiation consists primarily of ionized particles from Hydrogen (Z=1) to Iron (Z=26) and energies up to 50 GeV/n, shown in Figure 2.2 (Durante and Cucinotta, 2011; Grahn, 1973). While the fluence of ions in space above Z=2 is only 1% of the GCR spectrum, these high Z ions contribute significantly to the radiation dose and dose equivalent.

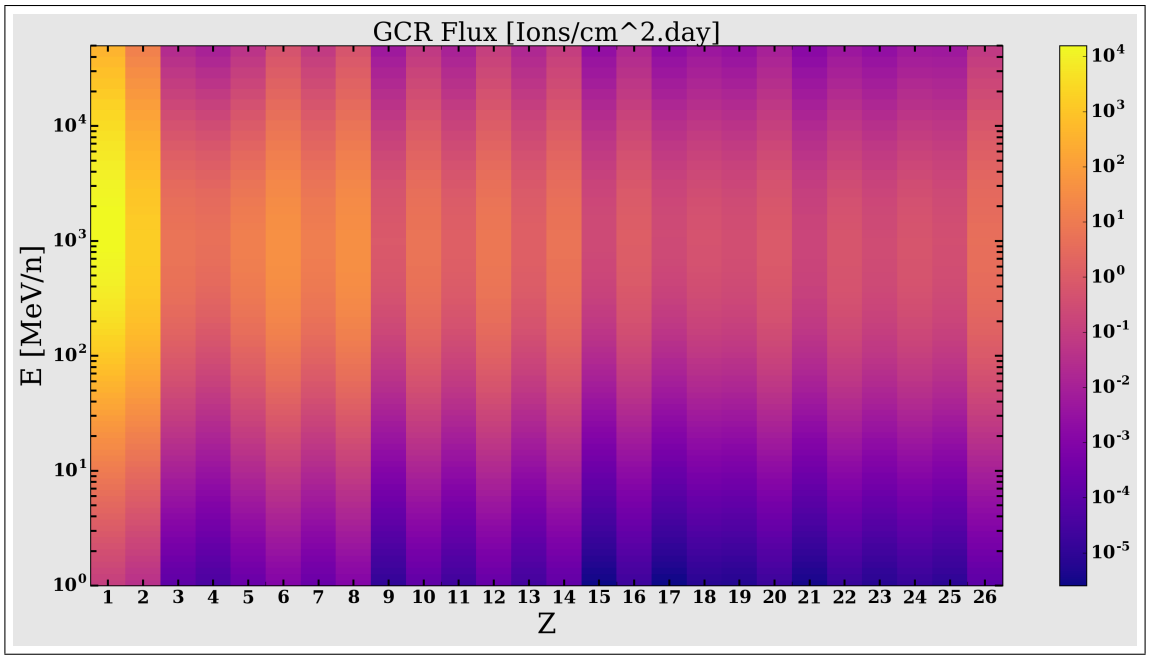

Figure 2.2: Galactic Cosmic Radiation (GCR) spectrum in free space. The abscissa of the plot is the ion charge Z ranging from proton (Z = 1) to Iron (Z = 26). The ordinate is the energy of the ions in MeV per nucleon. The colors represent the fluence rate of particles.

High Z ions contribute more to the total absorbed radiation dose due to their higher stopping power. Figure 2.3, shows the radiation dose from GCR as a function of energy and ion charge Z. The dose plot of Figure 2.3 was created by multiplying the fluence of particles by their representative stopping power in water. The relative dose contribution from protons, the largest fraction of the GCR fluence, is reduced when converted to absorbed dose. When compared to the fluence plot of Figure 2.2, the dose from higher Z ions, such as oxygen (Z=8) and iron (Z=26), is enhanced.

2.4.3 Radiation protection and quality factors for space

The astronaut occupation is exceptional and risk related to travel from Earth to space is far from negligible. However, it was formally recognized as early as 1969 that the effects of long duration radiation exposure during inter-planetary missions and extended stays at space stations needed to be studied. In 1989, the NCRP published specific recommendations for space activities in Report 98 Guidance on Radiation Received in Space Activities (NCRP, 1989). Career limits for exposure to radiation for astronauts were suggested that would limit the probability of developing

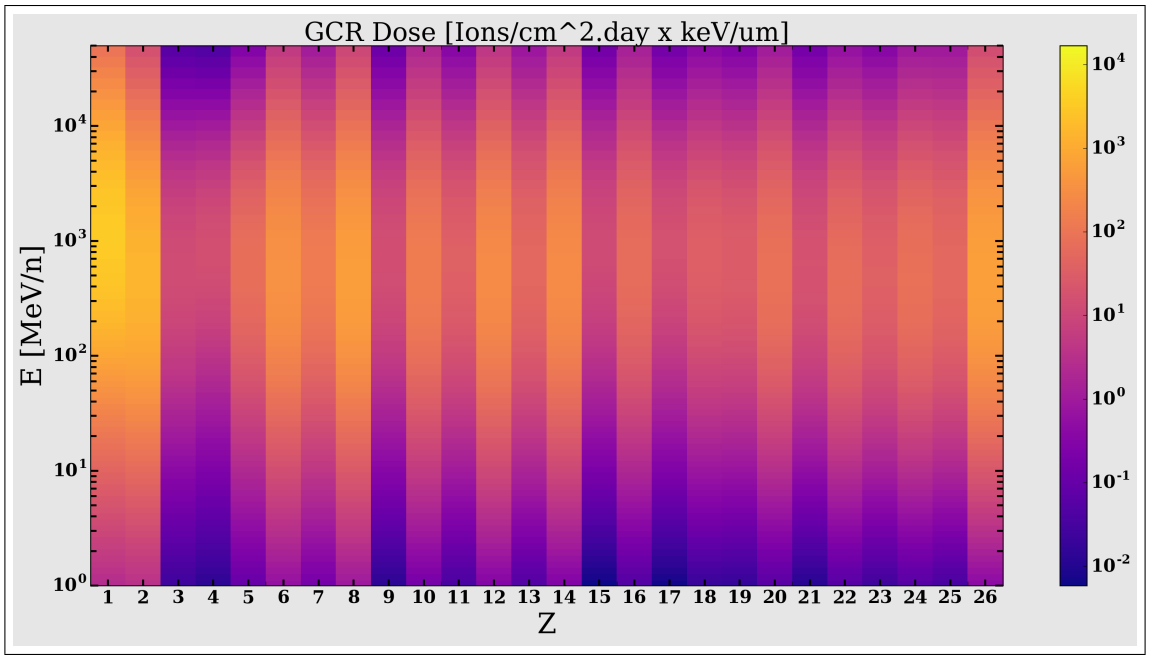

Figure 2.3: Contribution of absorbed dose from Galactic Cosmic Radiation (GCR) spectrum in free space. The abscissa of the plot is the ion charge Z ranging from proton (Z = 1) to Iron (Z = 26). The ordinate is the energy of the ions in MeV per nucleon. The colors represent the contribution to radiation dose. Note, the units for this plot are a surrogate for radiation dose and are not converted to J/kg in tissue.

fatal cancer to an absolute excess risk of 3%. This limit was translated into dose equivalent and based on age and gender for the first time (Table 2.3). Short term limits were also recommended for protection against deterministic (non-stochastic) effects to parts of the body such as the blood forming organs (BFO), lens of the eye and skin and are shown in Table 2.4. However, these limits were meant to be applied to exposures in low earth orbit and not other space situations, such as a mission to Mars (NCRP, 2000).

Table 2.3: Career whole body dose equivalent limits based on a lifetime excess risk of cancer mortality of 3×10^{-2}

Age (Years)	Female (Sv)	Male (Sv)
25	1.0	1.5
35	1.75	2.5
45	2.5	3.2
55	3.0	4.0

Table 2.4: Short term dose equivalent and career limits for protection against non-stochastic effects (Sv) to the blood forming organs (BFO), lens of the eye and the skin.

Time Period	BFO	Lens of the Eye	Skin
30 day	0.25	1.0	1.5
Annual	0.5	2.0	3.0
Career	See Table 2.3	4.0	6.0

The information needed to provide recommendations for missions beyond low-earth orbit was discussed in NCRPs report No. 153 and commentary 23 (NCRP, 2006, 2014). NCRP commentary 23 stated that it is reasonable to use the low earth orbit guidelines of 3% limit on the risk of exposure-induced death (REID), evaluated at the 95% confidence interval of the risk probability distribution function (PDF), as a starting point for future guidelines (NCRP, 2014). However, no specific recommendations were made for radiation protection limits of exploratory missions, due to the large uncertainty in REID and potential cardiovascular and central nervous system (CNS) effects.

Cucinotta et al. introduced revised quality factors based on available radiobiology data and heavy ion track structure based models (Cucinotta et al., 2013). These quality factors take into account more ion track structure and radiobiological information then the LET based ICRP quality factor. The NASA proposed quality factor for space radiation with atomic number Z and velocity β, is given as:

$$Q_{NASA}(Z,\beta) = (1 - P(Z,\beta)) + \frac{6.24\,(\Sigma_0/\alpha_\gamma)}{LET} \cdot P(Z,\beta), \tag{2.17}$$

where

$$P(Z,\beta) = \left(1 - e^{\frac{-(Z^*/\beta)^2}{\kappa}}\right)^m \cdot P_{TD}, \tag{2.18}$$

$$Z^* = Z(1 - e^{-\frac{1.25\cdot\beta}{Z^{2/3}}}), \tag{2.19}$$

and

$$P_{TD} = (1 - e^{-\frac{E}{E_{TD}}}). \tag{2.20}$$

The NASA quality factor also takes into account the different RBE for induction of leukemia and solid cancers using the parameters m, κ, Σ_0, and α_γ.

The dose equivalent contribution based on the updated NASA quality factor is shown in Figure 2.4. Implementation of the above NASA quality factor will introduce significant challenges to the development of radiation detectors. These revised quality factors challenge current systems primarily due to the complexities of identifying particle charge Z and energy E. While measurement of particles properties are possible on earth, it becomes significantly more challenging under the size, weight, and data bandwidth constraints of space.

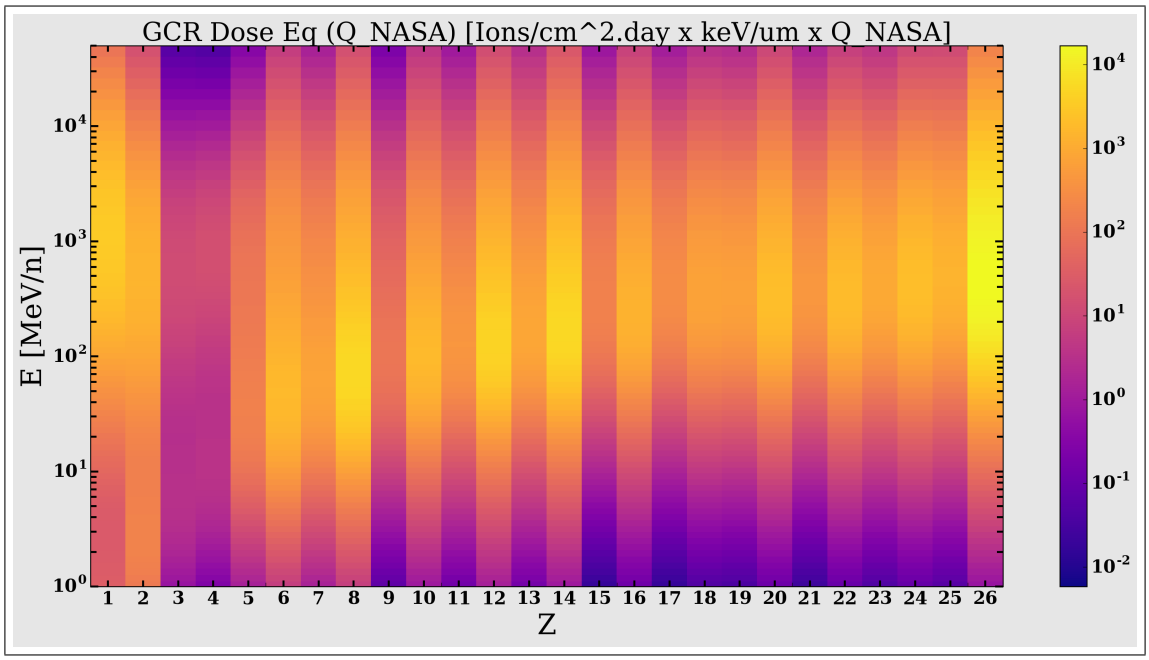

Figure 2.4: Contribution of dose equivalent from Galactic Cosmic Radiation (GCR) spectrum in free space. The abscissa of the plot is the ion charge Z ranging from proton (Z = 1) to Iron (Z = 26). The ordinate is the energy of the ions in MeV per nucleon. The colors represents the contribution to radiation dose equivalent. Note, the units for this plot are a surrogate for radiation dose equivalent and are not converted to the unit of Sv.

The challenge of creating a radiation detector compatible with the revised NASA quality factor has motivated several different solutions. One solution, proposed by Borak et al., was to keep all of the features of the NASA quality factor but retain the dependence solely on LET (Borak et al., 2014). The quality factor of Borak et al. is given as:

$$Q_{\text{Borak}}(LET) = (1 - P(LET)) + \frac{\Sigma_L}{LET} \cdot P(LET), \tag{2.21}$$

where

$$P(LET) = (1 - e^{-\frac{LET}{\Lambda}})^m. \tag{2.22}$$

The coefficients Σ_L, Λ and m are new model parameters, defined for both leukemias and solid cancers, and selected to closely agree with the NASA quality factors. Another potential solution has been proposed by Pinsky et al. that utilizes a complex radiation detector capable of track imaging to acquire the information necessary for the NASA quality factor (Pinsky and Chancellor, 2007).

2.5 Active radiation detectors

Many active radiation detectors have been used by the United States space program to measure the radiation environment in space (Badhwar, 2004; Hassler et al., 2012; Spence et al., 2010; Zeitlin et al., 2004). Active radiation detectors provide near real time results as opposed to passive detection systems that have to be evaluated at a later time. Additionally, active radiation detectors are capable of providing spatial and temporal information about the environment. A brief review of compact, low power consumption, active radiation detection systems used or proposed for use outside of low-earth orbit follows.

The Martian Radiation Environment Experiment (MARIE) was the first active radiation detector specifically designed to measure the radiation exposures astronauts would receive on Mars (Zeitlin et al., 2004). MARIE was one of the three instruments aboard the 2001 Mars Odyssey spacecraft injected into the orbit of Mars in October 2001. MARIE consisted of eight silicon detectors of varying thickness; a pair of 1 mm, four 5 mm and a pair of 300 μm. Particles between helium $Z = 2$ and neon $Z = 10$ are accurately measured over an energy range of 70 MeV/n to 500 MeV/n (Zeitlin et al., 2003). Additionally, protons are measured in the energy range of 30 to 100 MeV. The detector system had a mass of 3.3 kg and power consumption of 4 W. Particles with LET above 30 keV/μm were registered but no additional information was registered due to satura-

tion of the detector. Algorithms for particle identification based on MARIE data were mentioned but documentation on specific results of the classification effectiveness was not found (Lee et al., 2003).

The Radiation Assessment Detector (RAD) was deployed to Mars as a part of the Mars Science Laboratory (MSL) spacecraft (Hassler et al., 2012). The RAD was mounted on the top deck of the Curiosity rover and took radiation measurements inside the MSL during its 253 day cruise to Mars (Zeitlin et al., 2013). RAD consists on three 300 μm thick silicon detectors as well as scintillators to measure neutrons, not discussed in this work. The RAD detector is very compact with a total volume of 240 cm^3 and mass of 1.56 kg. RAD was designed with some basic segmentation that allowed the detector to only measure (accept) ions that traveled a well defined path in the detector. This technology utilized the coincidence and anti-coincidence concepts and also allowed for the measurement of neutrons. RAD was also designed to provide some of the necessary information of the revised quality factors of NASA that require knowledge of the Z and E of the incident particles. RAD was capable of measuring the total energy E for protons up to 100 MeV, carbon ions up to 200 MeV/n, iron ions up to 500 MeV/n and LET of charged particles over the range 0.2 to 1000 keV/μm (Zeitlin et al., 2013).

The Timepix is a position sensitive pixelated detector developed at CERN under the Medipix collaboration (CERN; Llopart et al., 2001, 2007). The Medipix family of detectors, including the Timepix, was developed to meet the needs of the complex Large Hadron Collider experiment. The Timepix detector consists of 256 x 256 55 μm square pixels for a total detection area of 2 cm^2 (Pinsky et al., 2011a). Similar to RAD, the sensor layer of the Timepix detector is made of silicon and is 300 μm thick. The unit weighs approximately 20 g and has dimensions of 8.6 x 2.1 x 1.0 cm^3. Power for the unit is supplied by a standard USB port on a laptop within the spacecraft or habitat and power requirements are below 2 W (Vykydal and Jakubek, 2011).

An attractive property of the Timepix detector is that radiation tracks of incident particles can be visualized (Hoang et al., 2014; Pinsky et al., 2011a). Initial results have been published documenting the challenges and potential benefits for ion charge and energy discrimination with the

Timepix detector (Pinsky et al., 2011b; Stoffle et al., 2012). However, these results do not clearly state the true positive rate, false positive rate, or other similar metrics for charge classification of heavy ions. Vilalta et al. published on the use of various machine learning techniques for classification of Si, Fe, O, N and Ne ions of similar LETs and concluded that a predictive accuracy of 81% was possible (Vilalta et al., 2011). However, classification accuracy for individual particles was not presented. Hoang et al. showed that it was possible to determine the angle of incidence and LET for heavy ions based on analysis of track images from the Timepix detector (Hoang et al., 2012, 2014). Additionally, Hoang showed that it was possible to distinguish between protons (Z=1) and helium ions (Z=2) using a variety of machine learning techniques (Hoang, 2013).

Despite all the research in this area, current detector systems and analysis methods have limited capabilities in identification of individual ion charge values (Z). Chapter 6 will present results from the use of a machine learning algorithm to classify ion charge in a space radiation field.

2.6 Conversion of stopping power in silicon to stopping power in water

Energy deposition in silicon detector systems is not equivalent to energy that would be deposited in tissue equivalent materials (e.g., water). Biological effectiveness of heavy ions is studied using the concepts of LET in water. Therefore, conversion of energy deposition in silicon to that in water is required for the use of quality factors and relative biological effectiveness. In 1998, Bradley et al. performed Monte Carlo studies to determine the appropriate factor for converting energy deposition in silicon to deposition in tissue and arrived at a factor of 0.63 (Bradley and Rosenfeld, 1998). The study of Bradley et al. was related to boron neutron capture therapy and a specific geometric setup and is not directly applicable to the GCR component of space radiation in this study. In 2008, Guatelli et al. also performed Monte Carlo studies and determined a ratio of 0.56 was appropriate for converting energy deposition in silicon to water (Guatelli et al., 2008). Guatelli et al. specifically focused on the conversion factor for high energy protons with energies similar to those associated with SPE events in LEO.

A GCR specific conversion factor was found in two different articles by Zeitlin. In 2010, Zeitlin et al reported that stopping power (dE/dx) in silicon is approximately related to LET in water by the constant 0.56 (Zeitlin et al., 2010). The conversion factor of Zeitlin et al. was reported in measurement data of the MARIE detector and agreed with the results of Guatelli et al. In 2013, Zeitlin et al. again reported a conversion factor in results of the RAD detector measurement on a trip to Mars. In this paper, Zeitlin et al. indicated the average value of the ratio LET in water to dE/dx in silicon is 0.625 for GCRs, with an associated uncertainty of 15% (Zeitlin et al., 2013). This 2013 conversion factor agreed with the results of Bradley et al. Results from this study on the appropriate ratio are presented in Section 5.2.2.

Chapter 3

Radiation transport methods and simulation designs

Modeling the passage of radiation through a medium has numerous applications in space radiation and hadron therapy. In space, understanding the impact of radiation on electronics, habitat materials and crew are important. For hadron therapy, accurate dosimetry is essential for treatment planning and only possible via computational models. Additionally, physical radiation detection systems have limited capability to measure patterns of energy deposition on the nanometer scale and studies at this scale are only possible computationally. The widely used method for computational modeling of radiation transport is the Monte Carlo method.

Monte Carlo methods are a statistical technique that have been used extensively to solve problems in areas of math, physics, biology, finance and economics. The modern Monte Carlo method was invented in 1946 by Stanislaw Ulam while he was at Los Alamos National Laboratory working on the nuclear weapons projects (Metropolis, 1987). The dramatic increase in computational power and corresponding decrease in cost have made Monte Carlo methods an important tool. Furthermore, Monte Carlo based simulations can provide more geometric flexibility and rapid progress than physical experiments. This work focuses on Monte Carlo methods to simulate complex radiation interactions and detector designs.

3.1 Radiation Transport and Monte Carlo methods

The Monte Carlo process can be understood by considering a hypothetical particle that interacts via two processes (Kawrakow, 1999). The two processes to consider are: absorption with total cross section σ_a and elastic scattering with total cross section σ_e. The generation of particle trajectories through a medium can then be computed using the following steps:

1. Particle starts with its initial conditions, e.g., energy, velocity, direction, and charge.

2. Sample a random distance to the next interaction from a probability distribution function (pdf).

3. Transport the particle to the new interaction coordinate.

4. Select the interaction type based on the probability of absorption, $\sigma_a/(\sigma_a + \sigma_e)$, and the probability of scattering $\sigma_e/(\sigma_a + \sigma_e)$

5. Compute or sample the selected interaction.

6. If secondary particles are created at this step they are introduced into the simulation and their trajectories will progress in the same manner.

7. Repeat steps 1 - 4 above until the boundaries of the problem are satisfied.

Radiation transport of real world scenarios are significantly more complex than the hypothetical particle presented. Large collaborations of scientists and software engineers have developed programs to handle the complexity of these simulations. Geant4, a toolkit for simulating the passage of particles through matter, is arguably one of the largest and most ambitious Monte Carlo projects (Geant4).

3.2 Geant4 Monte Carlo Toolkit

The Geant4 Monte Carlo toolkit, with its building block design, was chosen for this project (Agostinelli et al., 2003; Allison et al., 2016, 2006). With this software, space radiation detector experiments can be carried out virtually, without the use of expensive ground-based accelerator facilities. New detector designs can be validated virtually before costly construction. These simulations are only as good as their design, and each component of the radiation transport simulation and analysis methods must be carefully selected and well defined. In the following sections, the physics models and associated simulation parameters are described.

3.2.1 Physics list selection

In Geant4, the physics models used in the simulation need to be defined before the code can be run. Individual physics models that take into account specific physical interactions are defined and grouped into "lists" to cover a wide range of interactions types and energy ranges. Appropriate selection of the physics models is of great importance for accurate simulations. Based on the work by Ivantchenko et al. the QBBC physics list was chosen for these simulations (Ivantchenko et al., 2012). This physics list includes many different models and seeks high precision in many hadron-ion and ion-ion interactions over a wide energy range.

In Geant4, "energy thresholds" are defined along with the physics list and are used to control the simulations. Simulating every possible particle until they have lost all their energy is computationally impractical and time consuming. Energy thresholds allow the user to quickly modify which particles Geant4 decides to simulate.

Which particles Geant4 simulates, based on the energy threshold defined by the user, can be described in two steps. First, a physical interaction between a particle and its target is simulated and potential secondary particles are stored. Second, the Geant4 code checks the energy thresholds defined before determining which secondary particles are introduced back into the simulation and transported. If the kinetic energy of a particle is less than the threshold energy, it is not created and the energy of that particle is deposited at the location of interaction. The primary particles and higher order particles generated, above the threshold, are transported until they lose all of their energy.

In Geant4, energy thresholds are implemented as range cuts. The range of a potential secondary particle, in the material of interest, is computed. If the range is below the range cut, the particle is not generated and energy is deposited locally. Table 3.1 shows the range cut and energy threshold values used in these simulations. It is important to note that heavy ions range cuts are not included in Table 3.1. Heavy ions have no lower limit of production other than the physical constraints on the interaction and are simulated to zero range after they are produced.

Table 3.1: Geant4 simulation settings: range cuts and energy production thresholds for various particles in water and silicon

Particle	Range cut	Energy threshold (water)	Energy threshold (silicon)
gammma	1 km	10 GeV	10 GeV
e-	1 km	10 GeV	10 GeV
e+	1 km	10 GeV	10 GeV
proton	700 µm	70 keV	70 keV

3.2.2 Computer hardware and data size

All simulations were performed using a high-performance cloud-based Linux cluster available through the Amazon Elastic Compute service. Output data from the simulations were analyzed using custom software written in the Python programming language. Separate computation optimized and memory optimized clusters were used for the Geant4 simulations and data analysis respectively. Monte Carlo output datasets were 2 - 5 Gb in size and dependent on shielding and detector type, with 50 Gb total of simulation data analyzed.

3.3 Simulation design

For this study, three different simulations were created: 1) idealized detector system, 2) real detector system and 3) particle identification system. The similarities between the systems will be discussed first. Section 3.3.1 describes the general geometric setup that all the simulations have in common. Section 3.3.2 describes the incident spectrum of particles used, while Section 3.3.3 provides the general method for recording simulation results including the format of the simulation output data.

The unique features of each system are discussed in the appropriate sections that follow. Section 3.3.4 discusses the specific geometry of the idealized detector system used to determine appropriate detector spatial resolution. Section 3.3.5 discusses the specific geometry of the real detector system used to investigate the energy resolution of a detector system. Section 3.3.6 discusses the unique geometric features of the particle identification system.

3.3.1 General geometric setup

The geometric setup was designed to replicate the environmental conditions of a space-based detector system and is represented in Figure 3.1. Spacecraft shielding is often composed of aluminum due to its strength and low weight. Aluminum shielding, of thickness $2\,\mathrm{cm}$, $5\,\mathrm{cm}$ and $10\,\mathrm{cm}$, was placed downstream from an ion beam directed at the center of the shield and normal to the surface. The coordinate system of the simulation was defined with the x and y dimensions of the system extending laterally and the positive z direction extending downstream. The origin of the simulation, (x=0, y=0, z=0), is defined as the center of the detector at the back of the shielding. Positive z values start at the back of the shielding and extend downstream from the location primary ions are generated.

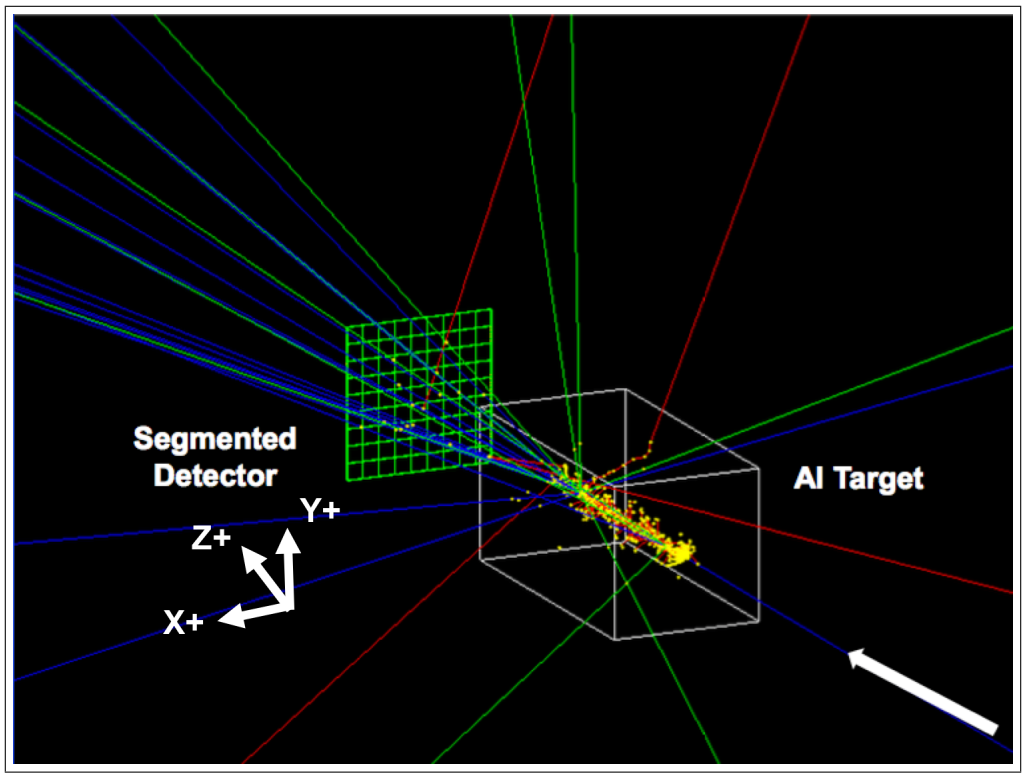

Figure 3.1: Geometric setup for experiment showing ion normally incident on shielding material with detector downstream. The detector segmentation and size shown are representative and were not used in the final design, discussed later in this paper.

Three different detector geometries were used and placed $10\,\mathrm{cm}$ downstream from the aluminum shielding:

1. A virtual detector for the idealized detector system, used to investigate spatial resolution.

2. A real detector to simulate a physical detector system, used to investigate energy straggling.

3. Two real detectors for simulating a particle identification detector system.

The first detector system, the idealized detector system, consisted of a virtual plane that scored the intersection of particles with the plane, but did not interact with the ions in the simulation. The seconded detector system, a physical detector system, replaced the virtual detector with a real detector, simulating a $300\,\mu\mathrm{m}$ silicon detector. The third detector system, used for particle identification, expanded on the physical detector system and used two $300\,\mu\mathrm{m}$ silicon real detectors. The Geant4 material G4Galactic, density $1 \times 10^{-25}\,\mathrm{g/cm^3}$, was selected for the free space surrounding the shielding and detector. Detector lateral dimensions were large, 3 m, to ensure all fragments created intercepted the detection plane.

In the idealized detector system, virtual detectors are used to identify the lateral position of the particles at various locations downstream from shielding. In the physical detector system, a thin silicon real detector replaces the virtual detector to simulate actual energy deposition. Primary particles are directed at the aluminum shielding, interact with the material and all primary and secondary fragments emerge downstream from the shielding. After interaction, the energy, position, direction, and ion species are scored by the detectors downstream. The output also identifies the mass, charge, and if the particles are primary, secondary or higher order. For the idealized detector system, the stopping power in water and silicon, based on the Bethe-Bloch formalism, is recorded as the particles intercept the virtual detector. In the physical detector system, the energy deposited as particles pass through the detector is recorded. The particle identification detector system used recorded information in the same way as the physical detector system but was modified to include energy deposition in a second real detector.

3.3.2 Spectrum incident on shielding

As discussed, galactic cosmic rays are composed of a broad range of ions and energies and can significantly increase the complexity of any experiments performed in this field. For this study only ions of He, C, Si and Fe at energies of 300, 900 and 2400 MeV/n were generated and directed at the detector, normal to the surface. These energies represent the approximate 25, 50 and 75 quantiles of the GCR spectra as illustrated by the inverse cumulative energy distribution in Figure 3.2. For each detector system, 12 million incident particles were simulated, i.e., 1 million particles per incident ion and energy. While these four ions were the only particles incident on the shield, all secondary ions were created and tracked.

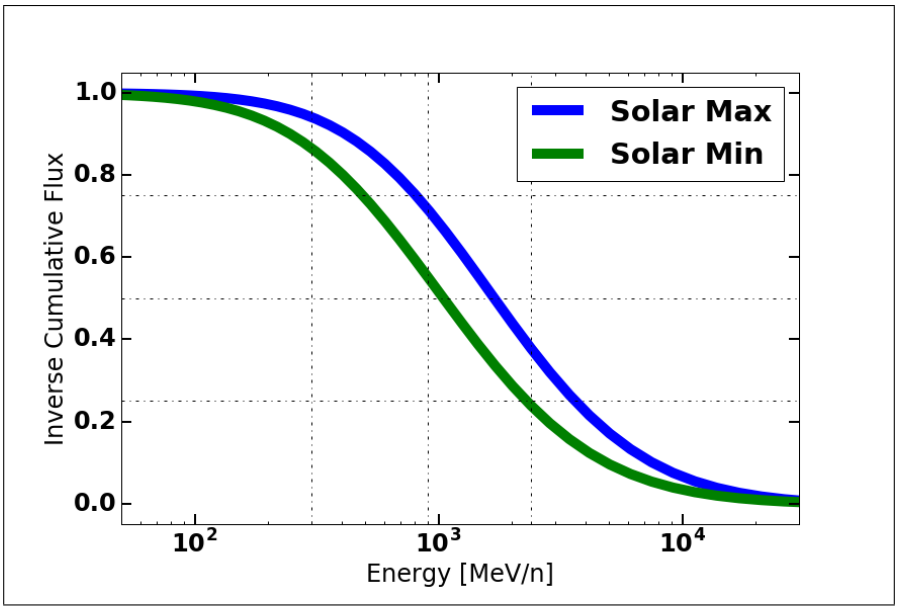

Figure 3.2: Inverse cumulative flux of GCR ions in free space. Based on the Badhwar-O'neill 2010 GCR model. Solar minimum and solar maximum values are based on 2010 and 2001 solar cycle respectively. Vertical dashed lines show the energy selections for this project. Horizontal dashed lines show the 75, 50 and 25 percentile.

3.3.3 Particles tracked

The focus of this work was to look at the response of the detectors for the incident primary and all fragments emerging from the target. For these studies, this was determined to be all ions

from protons (Z=1) to iron (Z=26). Sparsely ionizing particles such as electrons, pions, and muons were tracked, but for simplicity were removed from the simulation output. Additional processing of the simulated output data was performed to filter the data set to include only particles with solid angle defined by cosine(θ) greater than 0.9, i.e. $\theta < 25$ degrees. Filtering of data based on the z-directional cosine was done to represent a typical detector acceptance angle. Particles having a terminal range, after emerging from the shield, of less than 300 μm in silicon were also removed from the data set.

3.3.4 Idealized system

As described in the general geometric setup, Section 3.3.1, the basic idealized detector system consisted of a virtual detector placed $10\,\mathrm{cm}$ downstream from an aluminum shield. In addition, the idealized detector system, also consisted of two additional virtual detectors placed at $20\,\mathrm{cm}$ and $50\,\mathrm{cm}$ downstream. These additional virtual detectors were used to analyze how the proximity function changes as distance from the shielding increases. The methods of this analysis and results are presented in Chapter 4.

The stopping power of ions as they crossed the virtual detectors was obtained from Geant4 tables using the *emCalculator.ComputedTotalDEDX* method. The stopping power for silicon and water was recorded for every ion that crossed the virtual detectors. To use the *emCalculator.ComputedTotalDEDX* method small volumes of silicon and water had to be added to the simulation. These small volumes were placed upstream, in the negative z-direction, from the shielding and far away from the central axis of the geometry to reduce any possible scatter effects.

3.3.5 Real detector system

As described in the general geometric setup, Section 3.3.1, the physical detector system consisted of a real detector placed $10\,\mathrm{cm}$ downstream from an aluminum shield. In addition to the features of the idealized detector system, the physical detector system added the ability to record energy deposited in the real detector. Inside the real detector Geant4 records energy deposition per step size. Step size is determined internally by Geant4 based on the physics selections. For

the simulations in this work, the Geant4 default step size was used. The estimate of stopping power (LET) for the incident particle in Si was obtained by taking the total energy deposited in the detector per particle and dividing by the nominal thickness of $300\,\mu\mathrm{m}$.

This simulation setup was also used to investigate an appropriate factor for converting energy deposited in silicon to energy deposited in biologically equivalent material. To achieve this, stopping power values using the *emCalculator.ComputedTotalDEDX* method from the idealized detector system were also included in the simulation results. These additional "ideal" stopping power values were necessary to determine the distribution and average value for the conversion ratio discussed in Section 5.2.2.

3.3.6 Particle identification system

The particle identification detector system was nearly identical to the physical detector system. In fact, the single detector data discussed in Section 6.4.2 is the same output data as the physical detector system. The physical detector system was modified for the dual detector classification simulation discussed in Section 6.4.3. For the dual detector system, a second $300\,\mu\mathrm{m}$ detector was placed $0.1\,\mathrm{cm}$ further downstream from the backside of the first $300\,\mu\mathrm{m}$ detector. Energy deposition in the second detector was recorded in the same manner as the first detector. Additionally, stopping power values in the second detector were determined by dividing the total energy deposited by the nominal thickness of $300\,\mu\mathrm{m}$.

Chapter 4

Detector spatial resolution

As discussed in Chapter 1, appropriate spatial resolution will be important for active radiation detectors. Fragments created in shielding will be grouped in space and time as they intercept detection systems. These coincident events are measured as a single event in detection systems without appropriate segmentation (pixel size) or spatial resolution. Inaccurate measurement of stopping power spectra will occur from coincident events. Additionally, accurate estimates of quality factor, discussed in Section 2.4.3, will not be possible if a detection system cannot measure individual particles. Section 4.1 describes the analysis methods used to investigate the effects of spatial resolution. Section 4.2 presents the results of the analysis.

4.1 Detector spatial resolution analysis methods

Galactic cosmic rays will intercept a spacecraft isotropically i.e., the fluence is considered to be constant from all directions in space. However, the GCR flux is sufficiently low that coincident events from separate incident primary ions can be assumed to be negligible for this work. Assessment of spatial resolution can then be reduced to the investigation of a single incident ion impacting a shield with the detector placed behind. As discussed in Section 3.3, all incident particles simulated originate from the same point and are directed in the positive Z direction towards the center of the shielding. The idealized detector system, as discussed in Section 3.3.4, is downstream (positive z direction).

In Geant4 it is possible to define a predetermined spatial resolution or segmentation of the detector. However, a simulation with fixed segmentation will provide results for only one spatial resolution and many additional simulations would have to be run with varied segmentation size. Additionally, fixed lateral location of the detection system and segment size would provide results that depend on the location defined in the simulation. This inaccuracy would be due to the fact that translation of the detector in the lateral (x) and/or vertical (y) direction would score different

amounts of coincident hits per segment or pixel. Additional simulations could be designed that translate the detector but this would increase the required computations and add complexity. Due to these challenges, a novel proximity analysis technique was created to assess the spatial resolution requirements of a detection system.

The proximity analysis is depicted in Figure 4.1. This method removes the requirement for fixed segmentation and the issue of detector translation. The process is based on taking the location of each particle incident on the detection system and computing the distance to all possible neighbors. The particles incident on the detector can be the primary ion, secondary fragments of the primary ion and secondary fragments produced from components of the shield. These distances create a N by N proximity matrix that contains all possible distances, where N is the total number of particles incident on the detector. Duplicate pairs are removed by using only the lower triangle of the matrix. Columns of the matrix then represent the distance of other particles from the particle represented by that column, e.g. column 1 has the distances of other particles from particle 1. Non-zero values of the matrix at this stage form the proximity distribution. The proximity distribution shows the frequency of particles with separation X. Section 4.2.1 presents the results of these proximity distributions. The proximity distributions are used to create inverse cumulative distributions that represent the probability that a particle will have spacing greater than X. These proximity data form the basis for identifying coincident events in segmented detectors.

The effects of coincident events on a segmented detector are analyzed using the analysis sequence shown in Figure 4.2. The sequence works by choosing a pixel size, p, and creating a mask or spatial logic matrix. A mask or spatial logic matrix contains logical elements (true or false) and can be applied to other matrices. A value of true in the i, j position of the spatial logic matrix means that the distance between particle i and particle j is less than the pixel size p. By this convention, the diagonal entries of the spatial logic matrix correspond to the distance of a particle from itself and will always be true. Additionally, the rows of the spatial logic matrix represent particles that are coincident with the i particle, e.g., true values in row 1 represent particles coincident with

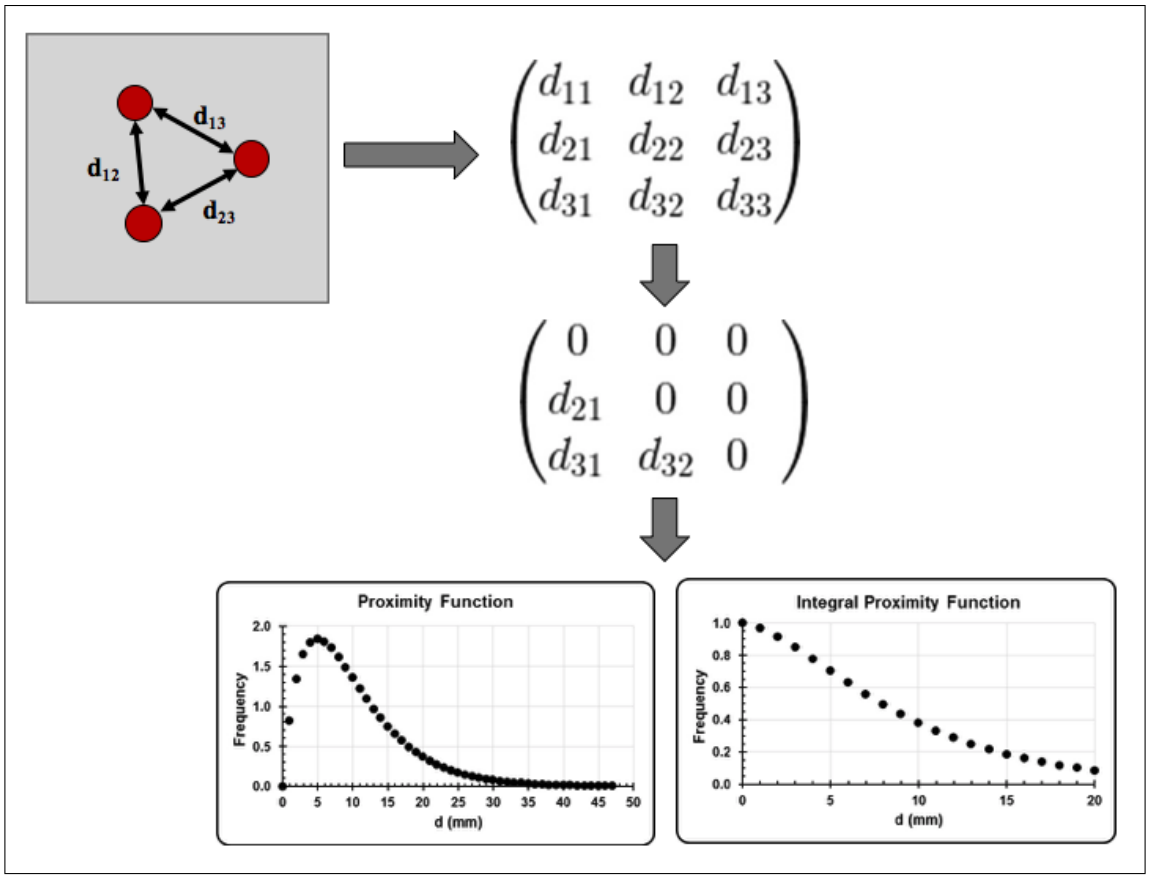

Figure 4.1: Proximity matrix flow chart: A matrix of distances between particles is created. The diagonal vector of the matrix is always zero and the lower triangle is taken to remove duplicate events. The resultant matrix is then used to create the proximity and inverse cumulative distributions.

particle 1. The spatial logic matrix is then used to determine the stopping power a detection system would measure from coincident events.

Stopping power matrices are created from Geant4 stopping power tables, i.e., the *emCalculator.ComputedTotalDEDX* method discussed in Section 3.3.4, for each particle intercepting the virtual detector. These tables are based on the selected physics packages and material and use unrestricted stopping power. The stopping power matrices are structured with the stopping power of particle i repeated along all j rows of column i, e.g., column 1 contains repeated values of the stopping power for particle 1. At this stage, all rows of the stopping power matrices are identical and provide no new information. However, when the spatial logic matrix is used to "mask" the stopping power matrix, coincident events can be identified. The stopping power of coincident

events measured by the idealized detector system is then found by summing along the rows. These sums include the stopping power for both single and coincident effects for a particular pixel size p. This process is repeated for every incident particle in the simulation.

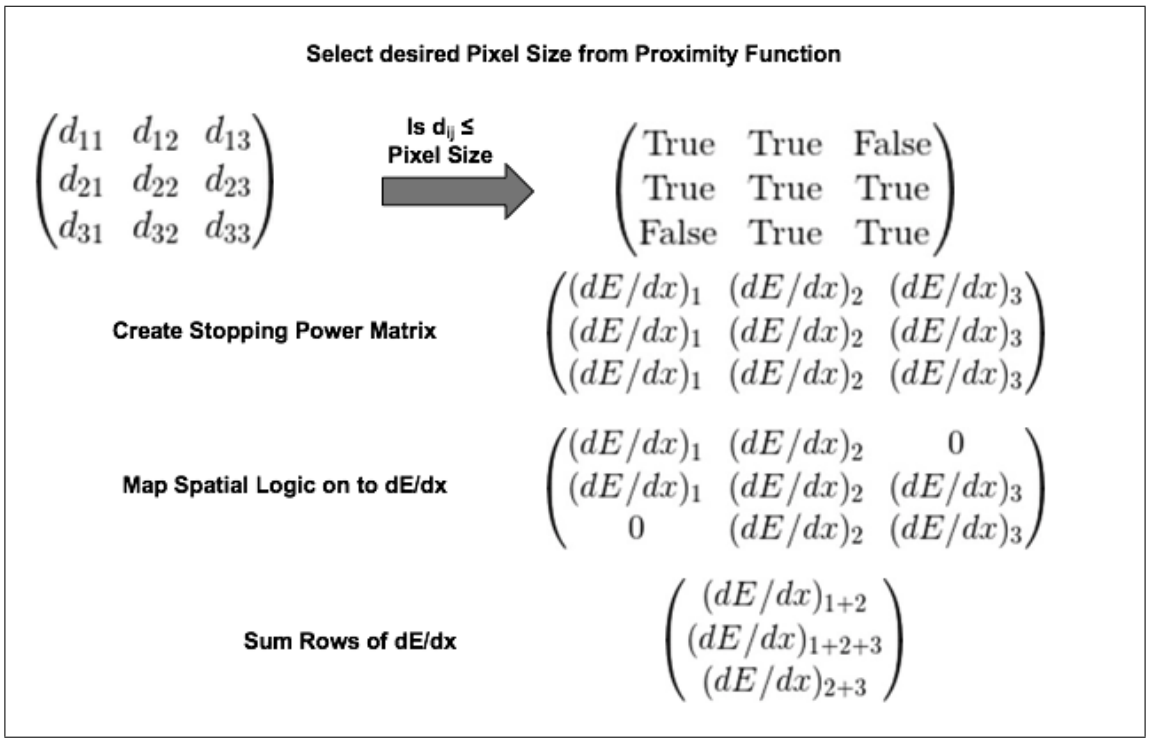

Figure 4.2: Coincident matrix flow chart: A matrix of each particle from its neighboring particles is created. A truth matrix is then created based on the selected pixel size. The truth matrix mask is applied to stopping power matrix. The result is then summed across the rows to get the coincident stopping power values.

The SciPy Python library (Jones et al., 2001–) was used for matrix manipulation. SciPy is highly optimized for matrix operations and provides significant speed increases over traditional programming loops. The speed increase gained by using matrices for the analysis sequence was essential for analyzing the large amount of output data generated.

4.2 Detector spatial resolution results

Results of the proximity distribution analysis, described in Section 4.1, are presented in Section 4.2.1. The proximity distribution results provide a method for determining the pixel size necessary

for mitigating coincident events. Proximity distributions are presented for the different ion, energy, shielding thickness and distance downstream.

Stopping power distributions are presented in Section 4.2.2 for the idealized detector system. Section 4.2.2.1 presents the ideal stopping power distributions considering perfect spatial resolution. Section 4.2.2.2 presents the results of coincident stopping power distributions for various segmentation sizes.

4.2.1 Proximity distributions

The proximity analysis methods, described in Section 4.1, were applied to the output of the Geant4 virtual detector simulations. The proximity distribution, i.e., the distances each fragment particle is from every other particle, was created. Figure 4.3 shows the results for each incident ion and energy after traversing 5.4 g/cm^2 (2 cm) Al shielding at a distance of 10 cm downstream from the back of the shielding. The proximity distributions have similar shapes for each ion and energy selected for the experiments. As expected, heavy ion fragments have an increased probability of being closely spaced. In general, the distributions are skewed towards lower distances. Moreover, the distributions have long tails that extend to large distances.

In general, with increasing energy the distance between fragments usually decreases, i.e., the distribution shifts to smaller proximity values (closer particle spacing). Particles are more closely spaced in the 1200 MeV/n case than the 900 MeV/n case. Based on the proximity results as a function of energy, the highest energy particles of the galactic cosmic radiation (GCR) will likely be the limiting factor in pixel size.

As discussed in section 3.3.4, the change in proximity distributions as a function of distance downstream from the detector was investigated. Figure 4.4 shows the proximity function 20 cm downstream from the back of the shielding and can be compared to the 10 cm downstream case in Figure 4.3. In general, the separation of fragments becomes larger with increasing distance from the detector. This result is expected, as any ion that emerges from the shielding will continue to

diverge due to the negligible probability of scattering in the lower density medium that fills the space between the shield and detector.

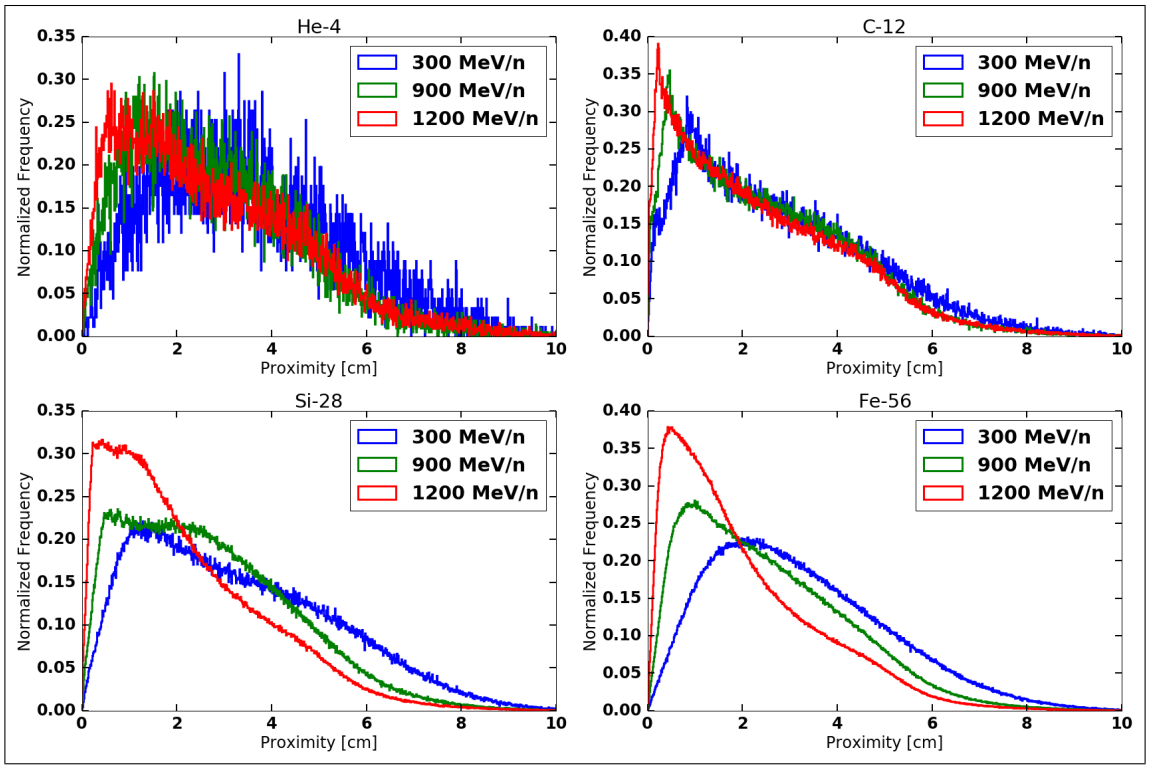

Figure 4.3: Proximity distributions: 5.4 g/cm^2 of aluminum shielding at 10 cm downstream from the back of the shield for incident He-4, C-12, Si-28 and Fe-56.

To determine the pixel size necessary to mitigate the effects of coincident events it is useful to look at what percentage of the proximity data lies above a certain pixel size. Inverse cumulative distributions of the proximity data show the pixel or segment size that would be needed to ensure a specific percentage of the data will not have coincident events. The benefit of these plots is that a mission specific confidence level can be selected and then the appropriate pixel size for that mission selected. Inverse cumulative distributions were generated by combining all of the normalized proximity distributions for the different ion, downstream distance, and shielding thickness combinations. In general, across all different experimental conditions a detector size of 1 cm gives 90% confidence that the detection system will not register coincident events.

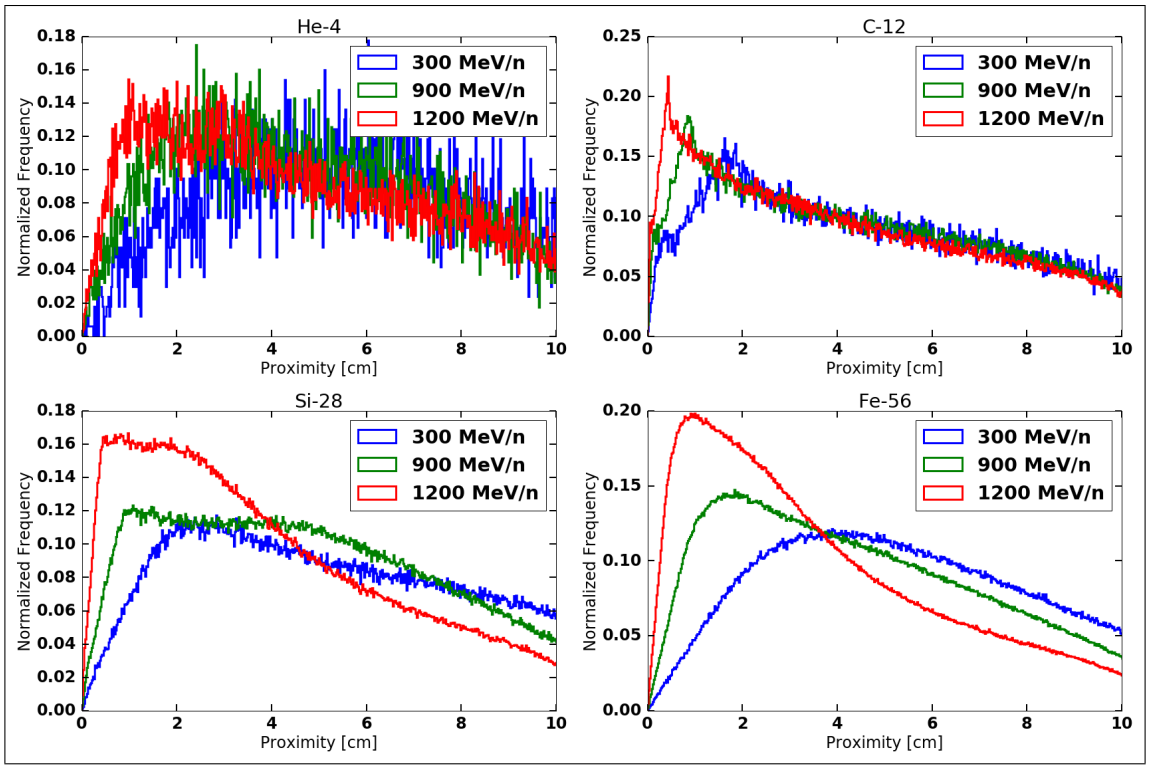

Figure 4.4: Proximity distributions: 5.4 g/cm^2 of aluminum shielding at 20 cm downstream from the back of the shield for incident He-4, C-12, Si-28 and Fe-56.

The inverse cumulative proximity distribution for all incident ions after traversing 5.4 g/cm^2 (2 cm) Al shielding at varying distances downstream are shown in Figures 4.5 and 4.6. As discussed above, these plots generally show that the distance between fragments increases with increasing distance downstream. In practice, this means that the closer a detector system is placed near shielding the smaller the pixel size will need to be to reduce coincident events. The inverse cumulative plots, for the 5.4 g/cm^2 (2 cm) Al shielding case, indicate that a pixel size of 0.1 cm will also be sufficient to ensure 99% of the events in a detector are non-coincident.

The inverse cumulative distributions with combined energies for each of the incident ions, for the 5.4 g/cm^2 (2 cm) Al shielding case, are shown in Figures 4.7 and 4.8. The plots show that when the incident energies are combined, there is little difference in the general shapes of the curves. Figure 4.8 focuses on the small pixel size region and shows that irrespective of ion a pixel size of 0.1 cm will ensure that 99% of the time events in the detector will be unique non-coincident events.

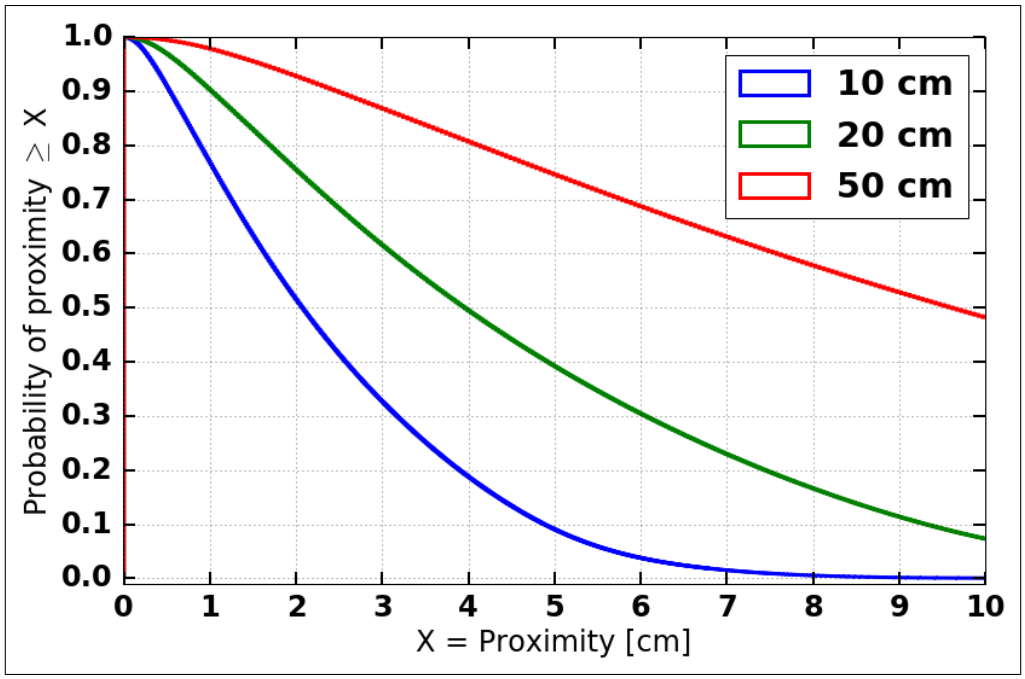

Figure 4.5: Inverse cumulative proximity distribution for all incident ions at 10, 20 and 50 cm downstream after 5.4 g/cm^2 (2 cm) of Al shielding

The thickness of shielding will also change the proximity distributions and the associated inverse cumulative distributions. The proximity distribution for all ions and energies at the thickest shield tested, 20 cm Al (54 g/cm^2), is shown in Figure 4.9. When compared to the 2 cm Al case above, the distributions have much greater proximity distances. The inverse cumulative proximity distribution for all incident ions in the simulation at varying thickness of Al are shown in Figure 4.10. A zoomed in version is shown in Figure 4.11. This plot shows a general trend that fragment proximity increases with increasing shielding thickness. The zoomed in plot indicates that a pixel size of 0.3 cm will reduce 95% of the coincident events for all shielding thicknesses. For thick shielding a detector of spatial resolution on the order of 0.7 cm would be sufficient.

The above plots and discussion show that a detection system with spatial resolution or detector pixel size less than 1 mm will be able to mitigate 99% of the possible coincident events in the detector system under various experimental conditions. The confidence level can also be varied based on the demands of the mission. The results and discussion on the change in stopping power distributions based on pixel size is discussed in Section 4.2.2.

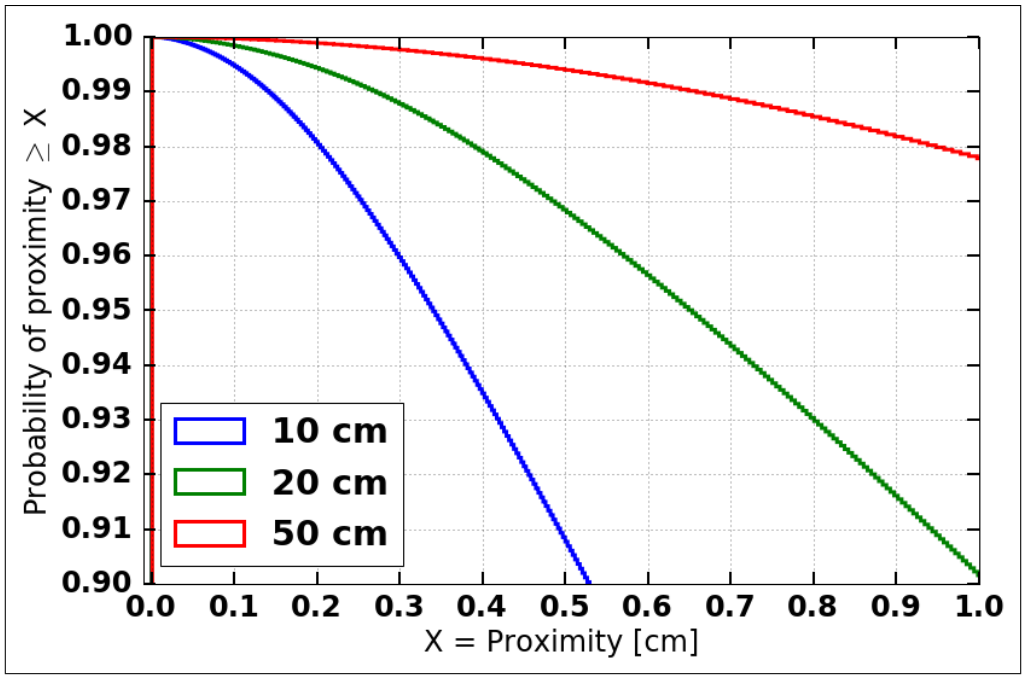

Figure 4.6: Inverse cumulative proximity distribution for all incident ions at 10, 20 and 50 cm downstream after 5.4 g/cm^2 (2 cm) of Al shielding. This plot focuses on the small pixel size and high probability region.

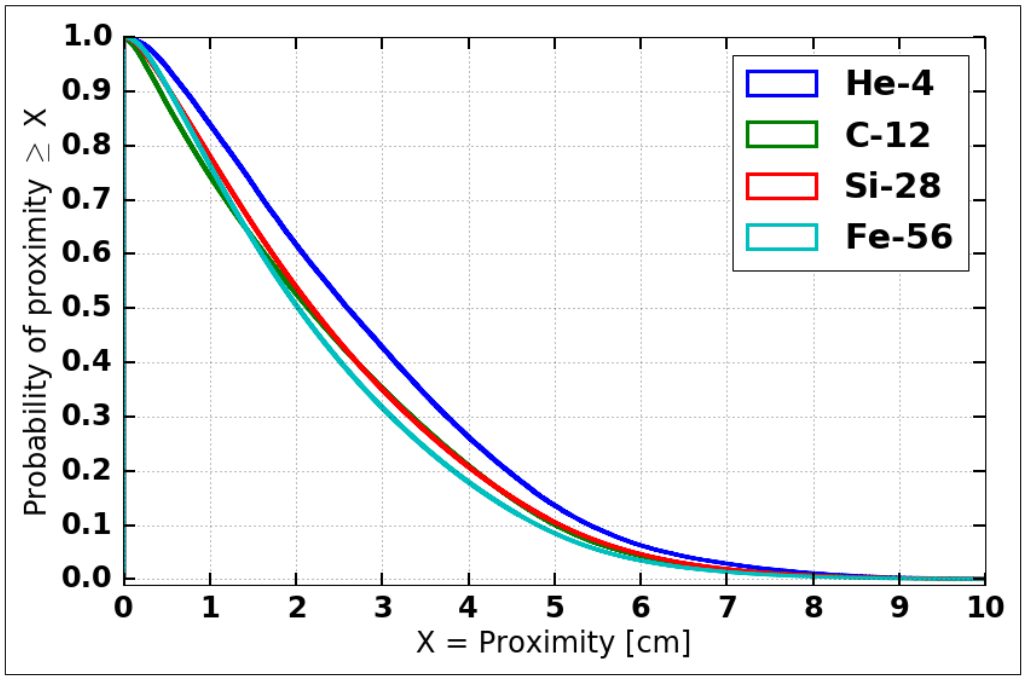

Figure 4.7: Inverse cumulative proximity distribution 10 cm downstream for each ion after 5.4 g/cm^2 (2 cm) of Al shielding.

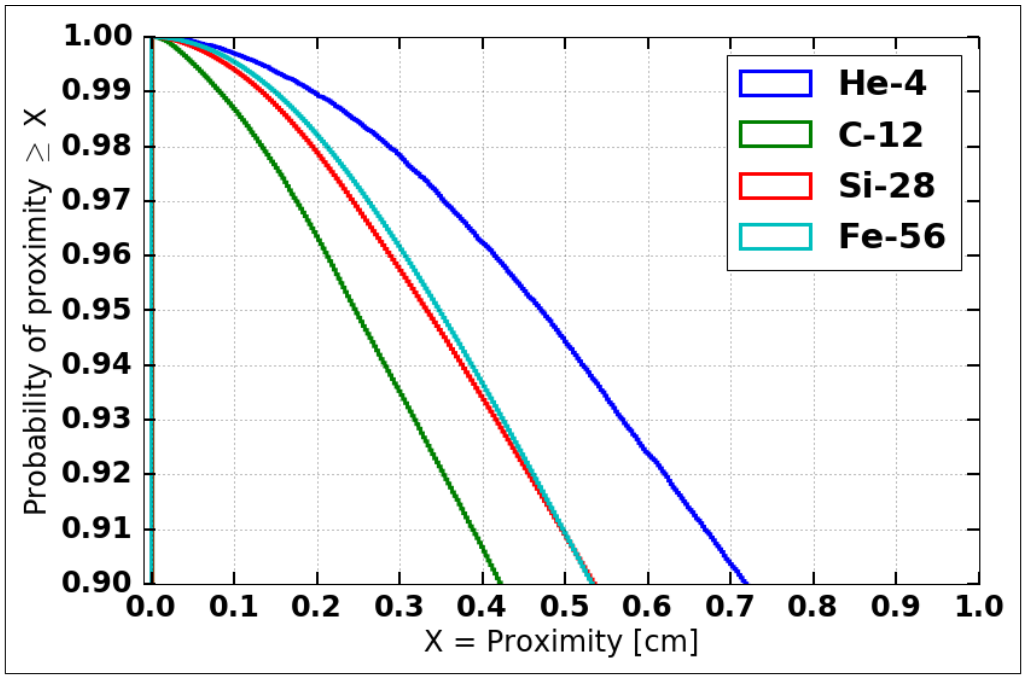

Figure 4.8: Inverse cumulative proximity distribution 10 cm downstream for each ion after 5.4 g/cm^2 (2 cm) of Al shielding. This plot focuses on the small pixel high probability region.

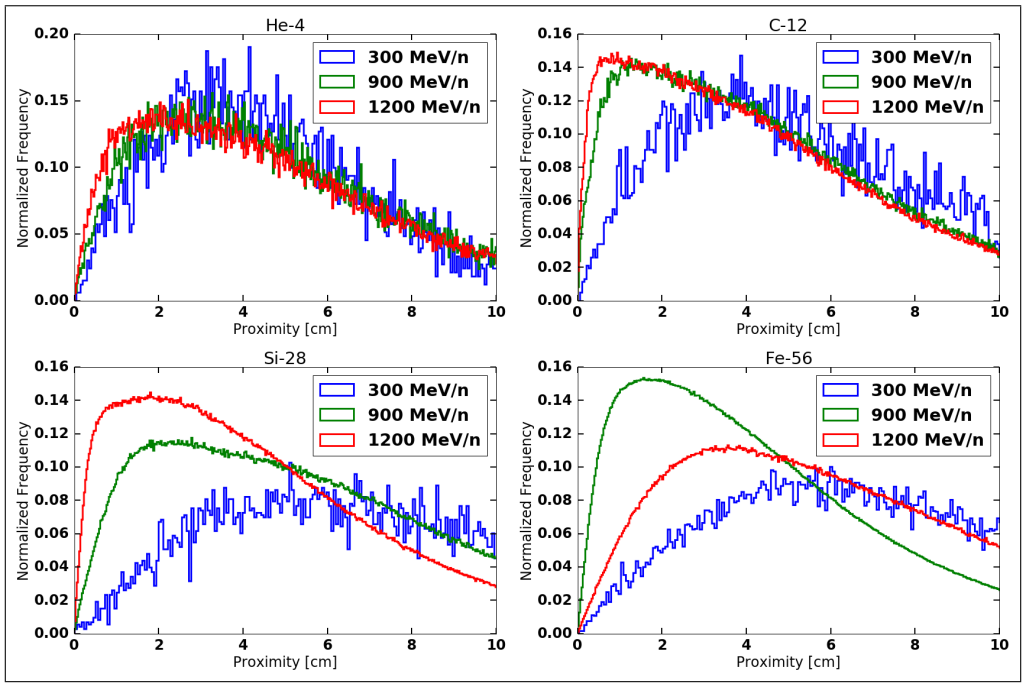

Figure 4.9: Proximity distribution 10 cm downstream after 54 g/cm^2 (20 cm) of Al shielding.

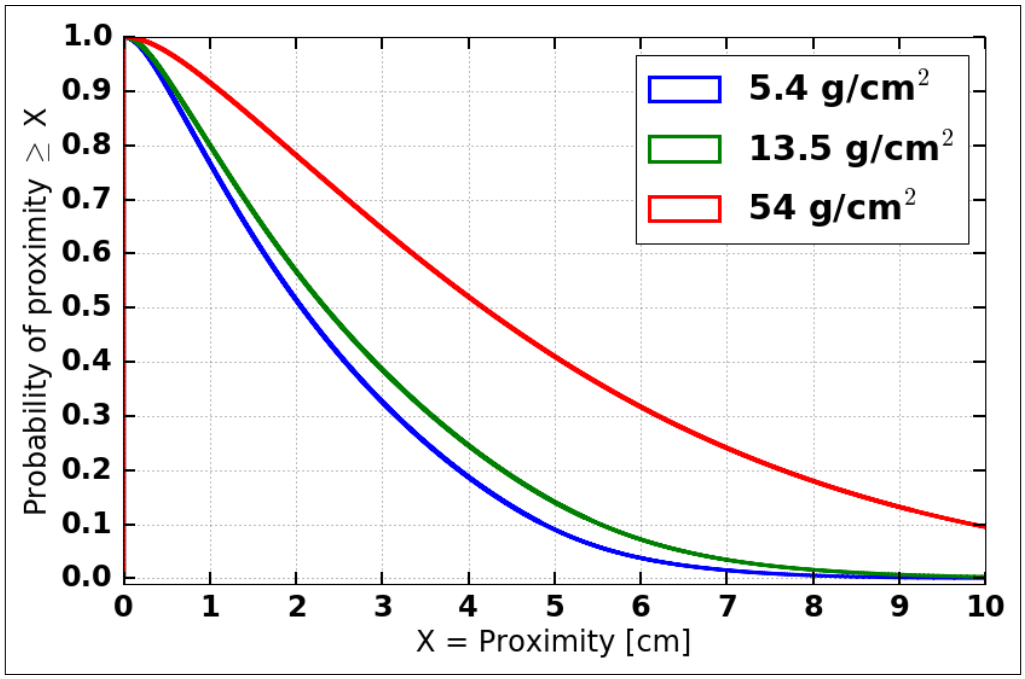

Figure 4.10: Inverse cumulative proximity distribution for all incident ions 10 cm downstream 5.4 g/cm^2, 13.5 g/cm^2, 54 g/cm^2 of Al shielding

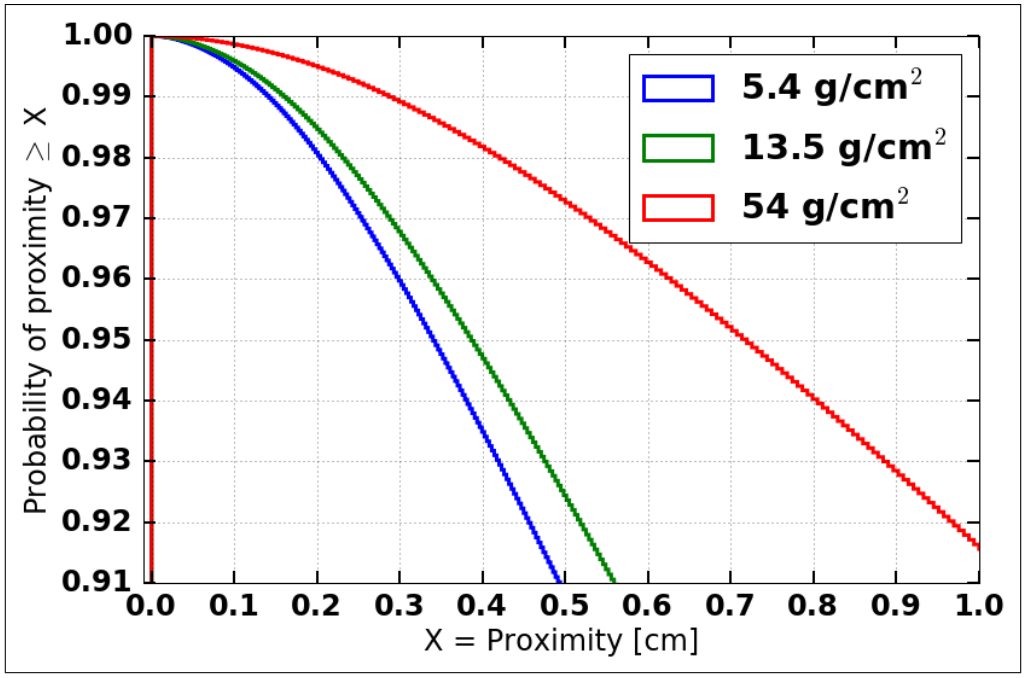

Figure 4.11: Zoomed in inverse cumulative proximity distribution for all incident ions 10 cm downstream 5.4 g/cm^2, 13.5 g/cm^2, 54 g/cm^2 of Al shielding

4.2.2 Stopping power distributions

The proximity analysis of Section 4.2.1 showed that a segmentation or pixel size can be selected to reduce the effects of coincident events. The next question to answer is: How much does the choice of pixel size, i.e., number of coincident events allowed, change the resultant stopping power distributions? Based on the methods described in Section 4.1, distributions of stopping power in silicon were created for various pixel sizes. The pixel sizes selected were ideal, i.e., perfect segmentation or no coincident events, 0.1 cm and 5 cm. The 5 cm pixel size represents an unsegmented detector and the 0.1 cm pixel size represents the recommended size based on the proximity analysis results. The distributions of the stopping power in silicon were plotted for all particles (primary and secondary) from incident ions of He, C, Si and Fe at energies of 300, 900 and 2400 MeV/n. First, plots are shown for the ideal pixel size case along with tables of the dose mean stopping power. Next, stopping power distribution plots are created for both the ideal and 5 cm pixel size. Furthermore, tables summarize the results of the coincident cases in terms of the dose mean stopping power. These plots highlight how the distribution can change due to the inaccurate scoring of coincident events.

4.2.2.1 Ideal stopping power distributions

Histograms showing the normalized frequency of stopping powers for the various incident ions, energies and shielding thicknesses are shown in Figures 4.12, 4.13, 4.14 and 4.15. The dose mean stopping power for each ion, energy and shielding combination was also computed.

The distributions of ideal stopping power generated by incident helium ions are shown in Figure 4.12. These distributions are very similar and nearly identical with the exception of the 300 MeV/n and 54 g/cm^2 case shown in the bottom left corner. This result is consistent with the fact that helium nuclei are tightly bound and less likely to fragment. The lower probability of helium ions to fragment is responsible for their potential dosimetric benefits in particle therapy for cancer (Zeitlin and La Tessa, 2016).

An increased stopping power near the end of the incident ions range explains the shifted primary peak in this lowest energy (300 MeV/n) and thickest shielding (54 g/cm^2) case. Moreover,

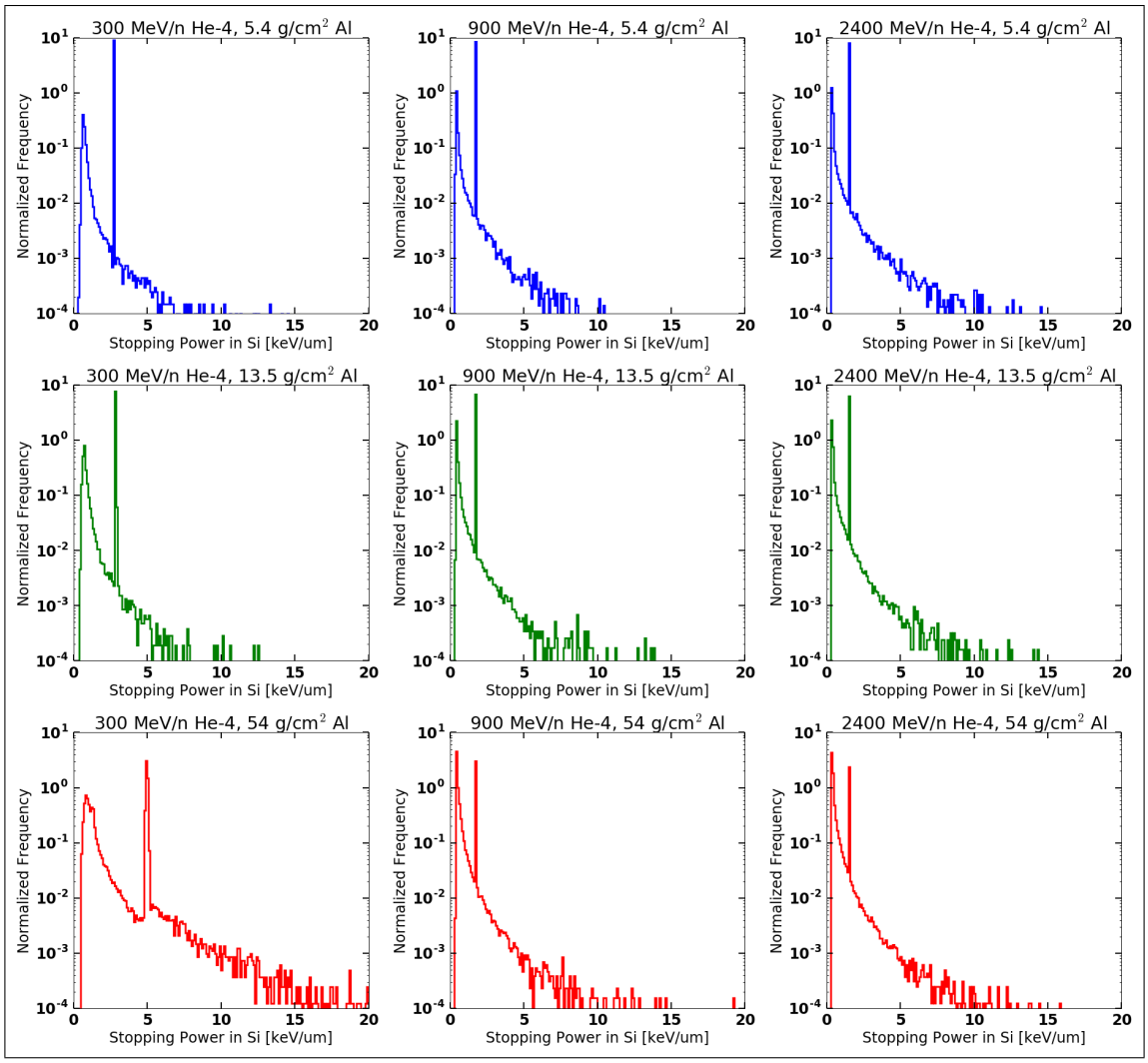

Figure 4.12: Stopping power in Si distribution for incident He ions of 300, 900 and 2400 MeV/n after 5.4 g/cm^2, 13.5 g/cm^2, 54 g/cm^2 of Al shielding

the lowest stopping power peak is the widest in this case. As the stopping power of the incident helium ions increases there is a corresponding increase in the energy of the secondary protons. Table 4.1 also shows this phenomenon with the highest dose mean stopping power coming from this case.

Table 4.1 summarizes the dose mean stopping power in silicon and water for each incident helium ion energy and shielding thickness. In general the dose mean stopping power for incident helium ions and their secondaries are low, under 5 keV/μm in silicon and under 2.5 keV/μm in

water. As expected the table shows that the stopping power commonly increases with decreasing incident energy.

Table 4.1: Dose mean stopping power [keV/μm] in silicon and water for incident He ions of varying energies. 5.4 g/cm^2, 13.5g/cm^2, 54 g/cm^2 Al shielding and 10 cm downstream

	300 MeV/n		900 MeV/n		2400 MeV/n	
	Si	Water	Si	Water	Si	Water
5.4 g/cm^2	2.71	1.44	1.75	0.93	1.77	0.95
13.5 g/cm^2	2.74	1.46	1.88	1.02	1.72	0.92
54 g/cm^2	4.62	2.50	1.59	0.86	1.44	0.79

The distributions of ideal stopping power generated by incident carbon ions are shown in Figure 4.13. Similar to the distributions of incident helium ions, the distributions for incident carbon ions have higher probability events at lower stopping powers. The increased frequency of low stopping power is typical of light fragment products such as protons. The plots also show a high frequency peak representative of a non-fragmented primary ion.

Distinct from the helium ion plots, the carbon plots show multiple peaks throughout the spectrum. These peaks represent the stopping power of secondary fragments created in the shield. Conservation of momentum requires these projectile fragments to have less total energy than the primary but similar velocity. Stopping power is proportional to the ion charge Z squared, i.e., $dE/dx \propto Z^2$. Projectile fragments will have lower ion charge and thus lower stopping power than the incident carbon ion. Five of these peaks, corresponding to ion charges of 1 - 5, can be seen below the primary carbon (Z=6) peak.

The left column of plots, corresponding to the 300 MeV/n incident carbon, show peaks having increased widths. This is likely due to ions nearing the end of their range in the shielding and producing a large number of secondary fragments with more varied velocity and stopping power. The bottom left plot, low energy and thick shielding, has similar characteristics to the comparable plot of incident helium ions and is characteristic of the incident ion not penetrating the shielding.

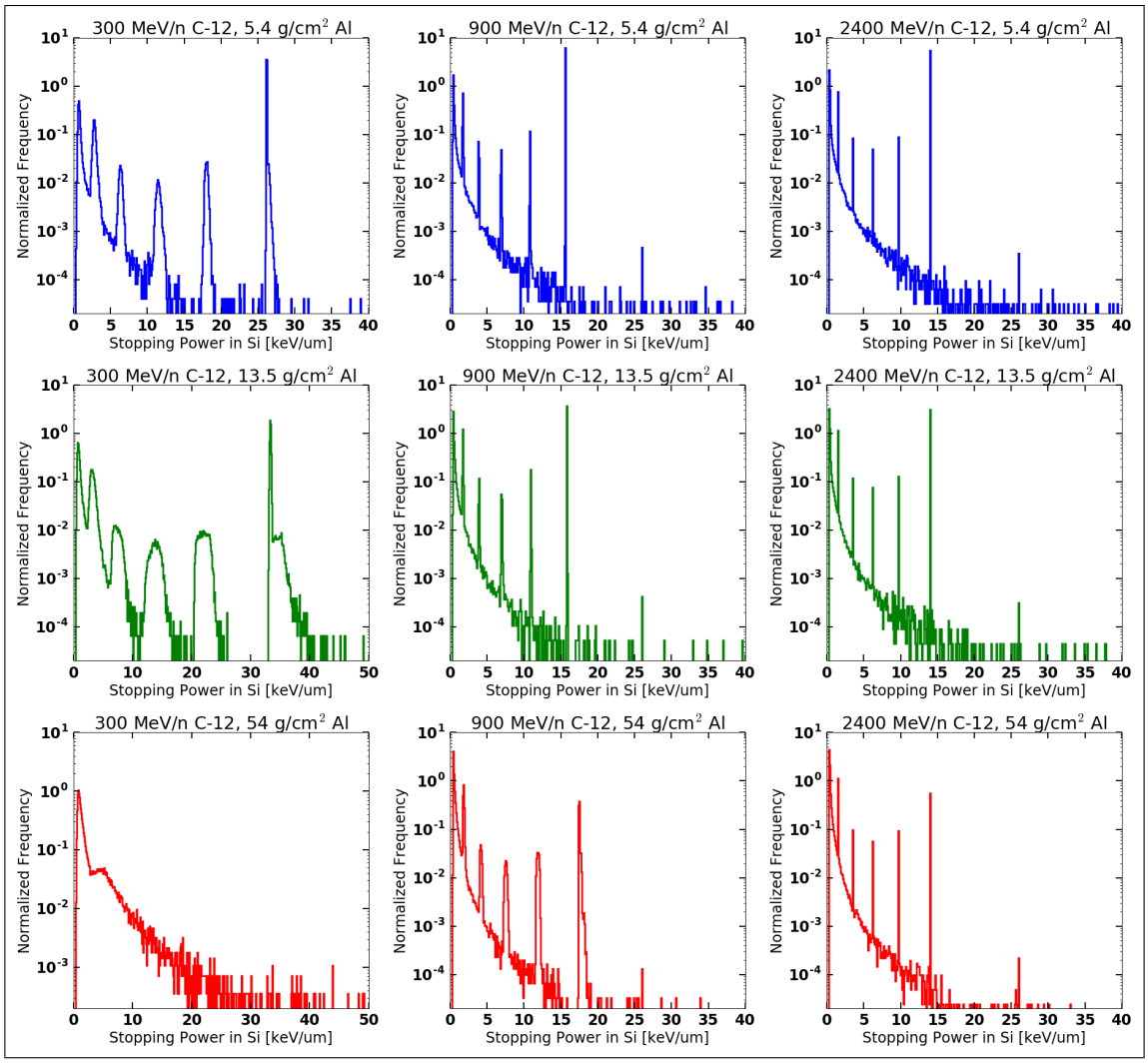

Figure 4.13: Stopping power in Si distribution for incident C ions of 300, 900 and 2400 MeV/n after 5.4 g/cm^2, 13.5 g/cm^2, 54 g/cm^2 of Al shielding

The middle left plot, 300 MeV/n and 13.5 g/cm^2 of shielding, shows the stopping power increasing as the incident particles are nearing the end of their range.

The distribution characteristics highlight the complexity of using ions such as C for radiation therapy purposes. Accurate carbon ion treatment planning will require extensive knowledge of the fragmentation spectrum produced inside the patient. With respect to space applications, the astronauts bodies will be exposed to the full range of the fragmentation spectra. Each unique incident GCR ion will produce complex effects within the body.

Table 4.2 summarizes the dose mean stopping power in silicon and water for these cases. In general, the dose mean stopping power for incident carbon ions and their fragments is five times higher than incident He ions. The dose mean stopping power ranges from 7 - 31 keV/μm in silicon and between 4 - 17 keV/μm in water.

Table 4.2: Dose mean stopping power [keV/μm] in silicon and water for incident C ions of varying energies. 5.4 g/cm^2, 13.5g/cm^2, 54 g/cm^2 Al shielding and 10 cm downstream

	300 MeV/n		900 MeV/n		2400 MeV/n	
	Si	Water	Si	Water	Si	Water
5.4 g/cm^2	25.44	13.58	15.08	7.93	13.51	6.94
13.5 g/cm^2	31.21	16.77	14.36	7.55	12.65	6.50
54 g/cm^2	7.36	4.20	11.51	6.08	8.43	4.34

The distributions of ideal stopping power generated by incident silicon ions are shown in Figure 4.14. The distributions show very similar characteristics to the helium and carbon plots already discussed. The main difference being that incident silicon ions have more projectile fragments, giving more peaks in the spectrum. Additionally, the stopping power distribution is shifted to higher values when compared to lower Z incident ions. The higher stopping power results from a higher Z incident ion and higher Z fragments. The higher stopping power is also apparent in the the fact that now 3 of 9 plots, show characteristic shapes of the incident ion not penetrating the shielding. The top left panel, 300 MeV/n and 5.4 g/cm^2 Al shielding, shows the wide fragment peaks associated with the incident ions reaching the end of their range. For silicon ions this phenomenon is occurring after less shielding than was shown in the carbon plots.

The dose mean values, summarized in Table 4.3, validate the observations from the plots. As the incident ions are nearing the end of their range, the associated increase in stopping power can be observed in the dose mean average values. With the exception of the 300 MeV/n ions incident on 54 g/cm^2 shielding, all dose mean values are higher than those in the carbon table. The lowest energy ion and thickest shield case shows that even secondary ions produced in the shielding are

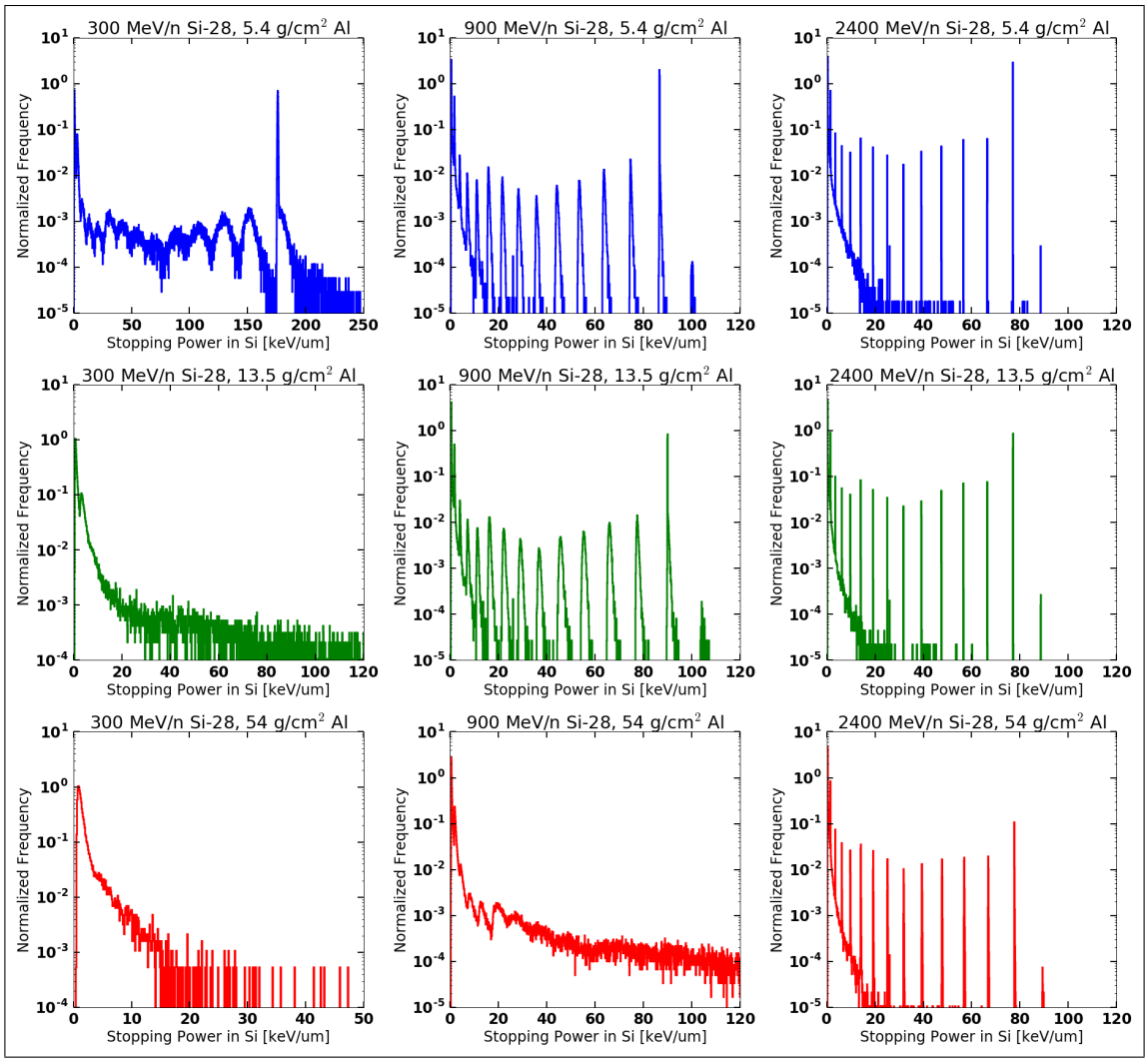

Figure 4.14: Stopping power in Si distribution for incident Si ions of 300, 900 and 2400 MeV/n after 5.4 g/cm^2, 13.5 g/cm^2, 54 g/cm^2 of Al shielding

not making it to the end of the shielding. Only protons with low stopping power and sufficient energy are making it to the detector under these conditions.

The distributions of ideal stopping power generated by incident iron ions are shown in Figure 4.15. These plots demonstrate many of the same characteristics discussed in the He, C and Si cases. One notable difference is the case for 5.4 g/cm^2 of shielding and incident ion energy of 300 MeV/n. This plots abscissa has been extended to highlight that this particular choice of energy and ion combination allows the incident iron ions to emerge slowed down with very high LET. The range of these particles is about 1 mm and fell just outside of the range cut of 300 μm implemented

Table 4.3: Dose mean stopping power [keV/μm] in silicon and water for incident silicon ions of varying energies, 5.4 g/cm^2, 13.5g/cm^2 and 54 g/cm^2 Al shielding and 10 cm downstream

	300 MeV/n		900 MeV/n		2400 MeV/n	
	Si	Water	Si	Water	Si	Water
5.4 g/cm^2	170.1	91.1	83.2	43.5	74.0	37.7
13.5 g/cm^2	67.0	38.5	81.2	42.5	69.3	25.3
54 g/cm^2	4.9	2.8	139.3	80.1	25.8	23.4

in the analysis. The dose mean stopping power for this case is over 5 times higher than the other cases at 1856 keV/μm.

The dose mean stopping powers in silicon and water are summarized in Table 4.4. Table 4.4 shows a decrease in the dose mean stopping power for the 300 MeV/n case with 13.5 g/cm^2 shielding and the 300 MeV/n and 900 MeV/n with 54 g/cm^2 case when compared to the silicon table. The other entries in the table show the highest dose mean stopping powers for the study. This result is consistent with expectation based on the Z^2 dependence in the Bethe-Bloch equation.

Table 4.4: Dose mean stopping power [keV/μm] in silicon and water for incident Fe ions of varying energies. 5.4 g/cm^2, 13.5g/cm^2, 54 g/cm^2 Al shielding and 10 cm downstream

	300 MeV/n		900 MeV/n		2400 MeV/n	
	Si	Water	Si	Water	Si	Water
5.4 g/cm^2	1857	1160	294	155	258	132
13.5 g/cm^2	15.4	9.0	302	160	242	125
54 g/cm^2	4.0	2.3	35.6	20.3	170	90.0

Overall, the distributions of stopping power for the incident ions of this study have some common features. In general, the stopping power distributions have the highest frequency of events at smaller stopping powers, e.g. 0 - 5 keV/μm. These events correspond to protons that have low stopping power and are created in large numbers from fragmentation events.

Additionally, the distributions show a prominent high frequency peak that corresponds to the primary incident ion stopping power after it has emerged from the detector. These peaks are present for all incident ions but are most easily identified in the helium case shown in Figure 4.12.

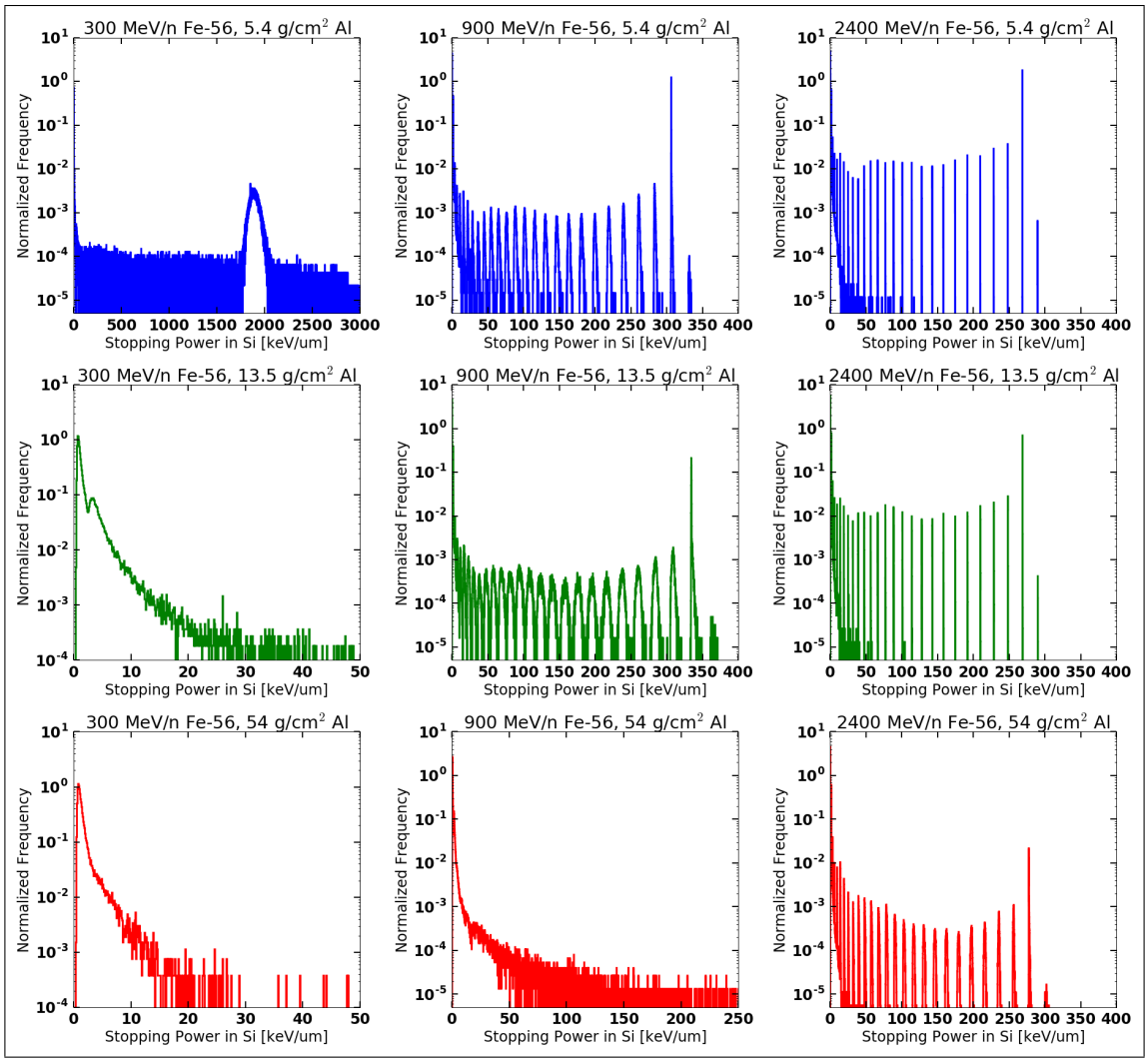

Figure 4.15: Dose mean stopping power [keV/μm] in silicon and water for incident iron ions of varying energies, 5.4 g/cm^2, 13.5g/cm^2 and 54 g/cm^2 Al shielding and 10 cm downstream

These events correspond to non-fragmentation events and thus should not change in subsequent coincident analyses.

Another common feature of the stopping power distributions for incident C, Si and Fe are the appearance of peaks corresponding to secondary projectile fragments. These can be identified as lower frequency peaks to the sides of the primary incident particle peaks. Carbon ions incident on 5.4 g/cm^2 of aluminum, shown in the top row of Figure 4.13, clearly show these features. The 300 MeV/n case clearly shows 6 distinct peaks corresponding to fragments with ion charge of $Z = 1$ to $Z = 6$. The remaining energies in the top row, 900 and 2400 MeV/n, exhibit the same

behavior but have an additional peak above the highest frequency carbon $Z = 6$ peak. These low probability peaks correspond to target fragments generated from the aluminum shielding that have a Z of greater than 6. More often than not, the other stopping power distributions show similar fragmentation peaks.

In some cases, no peak in the stopping power distribution corresponding to the incident ion can be seen. This is due to the primary incident particle not having sufficient energy to emerge from the shield. This results in a distribution that has minimal fragmentation peaks and is dominated by protons with low stopping power that have sufficient range to exit the shield.

4.2.2.2 Coincident stopping power distributions

The effects of coincident events on the distributions of stopping power and associated dose mean values were analyzed. Similar to the previous section on ideal stopping power, plots and tables were made for all combinations of incident ion and shielding thickness. In the plots of this section, the distributions of ideal stopping power were plotted along with the distributions of coincident stopping power for a pixel size of 5 cm. Based on the results of the proximity analysis, dose mean values were tabulated for the ideal, i.e., no segmentation, 0.1 cm and 5 cm pixel size.

Distributions of stopping power for the ideal and 5 cm pixel size for incident He-4 ions are shown in Figure 4.16. For all incident energies and shielding thicknesses these plots show small but distinct shifts towards higher stopping power. Furthermore, a corresponding decrease in the frequency of low stopping power events is seen. This is consistent with the expectation of the experiment. Low stopping power secondary ions, primarily protons, are the most common fragmentation product. Coincidence of multiple closely spaced secondaries would decrease the frequency of these single events and replace them with combined events a factor of 2 or more times higher than the single events in the distributions.

Dose mean stopping power values for the ideal, 5 cm and 0.1 cm pixel size are tabulated in Table 4.5. These results show that for the 5 cm pixel size bias in stopping power of up to 30%, for the 2400 MeV/n and 54 g/cm^2 shielding case, are possible. These large percent changes are due to the fact that the dose mean stopping powers are numerically small. The low energy incident

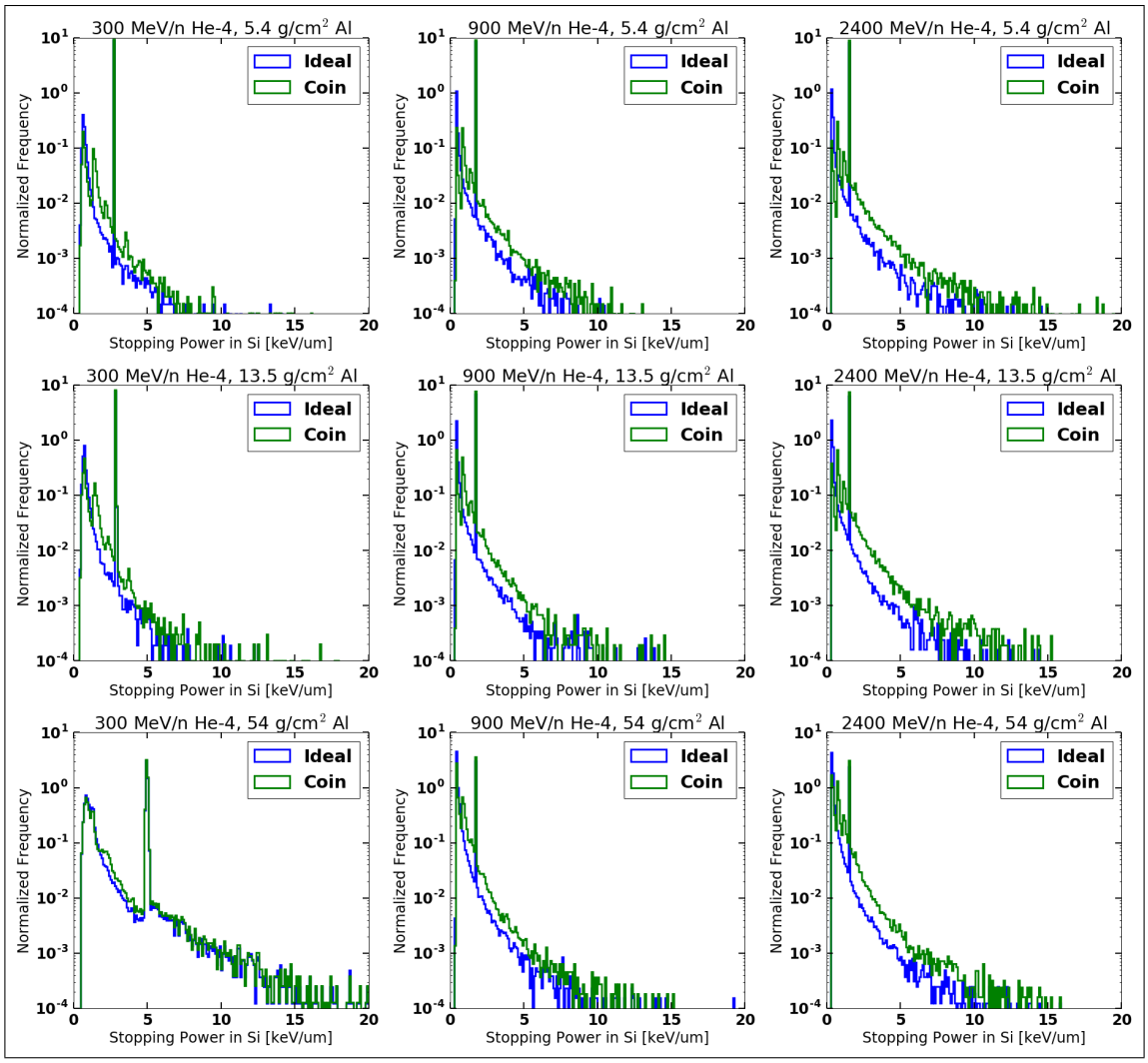

Figure 4.16: Stopping power distributions is Si for 5 cm pixel vs ideal for incident He ions of 300, 900 and 2400 MeV/n after 5.4 g/cm^2, 13.5 g/cm^2, 54 g/cm^2 of Al shielding

helium ions, 300 MeV/n, showed the least change for the 5 cm pixel size. While the high energy incident helium ions, 2400 MeV/n, showed the largest discrepancy. Table 4.5 also shows that for incident helium ions, with a detector pixel size of 0.1 cm, the effects of coincidence are negligible. The resulting dose mean stopping power for all cases was not different from the ideal pixel size case.

Figure 4.17 shows the distributions of stopping power for incident carbon ions for all the different energy and shielding thickness combinations. In contrast to the helium plots, the 5 cm pixel size distributions of coincident stopping power display more changes in structure. These plots

Table 4.5: Dose mean stopping power [keV/μm] in Si for the ideal, 5 cm pixel and 0.1 cm pixel cases for incident He ions of varying energies. 5.4 g/cm^2, 13.5g/cm^2, 54 g/cm^2 Al shielding and 10 cm downstream

	300 MeV/n			900 MeV/n			2400 MeV/n		
	Ideal	5 cm	0.1 cm	Ideal	5 cm	0.1 cm	Ideal	5 cm	0.1 cm
5.4 g/cm^2	2.71	2.76	2.71	1.75	1.87	1.75	1.77	2.12	1.77
13.5 g/cm^2	2.74	2.79	2.74	1.88	2.20	1.88	1.72	2.08	1.72
54 g/cm^2	4.62	4.68	4.62	1.59	1.85	1.59	1.44	1.86	1.44

show a more distinct decrease in the frequency of low stopping power events and a corresponding increase in higher stopping power events. While the peaks of the $Z \geq 5$ ions are still mostly preserved, these peaks show additional structure to the right of the peaks. The increase in event frequency to the right of the ideal incident ion peak corresponds to the stopping power added from other low stopping power ions, mostly protons.

Table 4.6 summarizes the dose mean stopping power for the different pixel sizes. Although the plots show visible structural differences when compared to the incident He ion plots, the relative difference in the dose mean stopping power is lower. For incident carbon ions the highest percent difference, when compared to the ideal case, is 19%. For all but two, the 300 MeV/n and 2400 MeV/n at the thickest shielding (54 g/cm^2), the percent difference between the 5 cm and ideal pixel size is less than 1%. Dose mean stopping power for the 0.1 cm pixel size showed the same results as for the He case. Mainly that a pixel size of 0.1 cm allows the detector system to faithfully recreate the stopping power distributions and associated dose mean stopping powers.

Table 4.6: Dose mean stopping power [keV/μm] in silicon for the ideal, 5 cm pixel and 0.1 cm pixel cases for incident C ions of varying energies. 5.4 g/cm^2, 13.5g/cm^2, 54 g/cm^2 Al shielding and 10 cm downstream

	300 MeV/n			900 MeV/n			2400 MeV/n		
	Ideal	5 cm	0.1 cm	Ideal	5 cm	0.1 cm	Ideal	5 cm	0.1 cm
5.4 g/cm^2	25.4	25.4	25.4	15.1	15.1	15.1	13.5	13.5	13.5
13.5 g/cm^2	31.2	31.0	31.2	14.4	14.2	14.4	12.6	12.5	12.7
54 g/cm^2	7.4	8.8	7.4	11.5	11.0	11.5	8.4	8.0	8.4

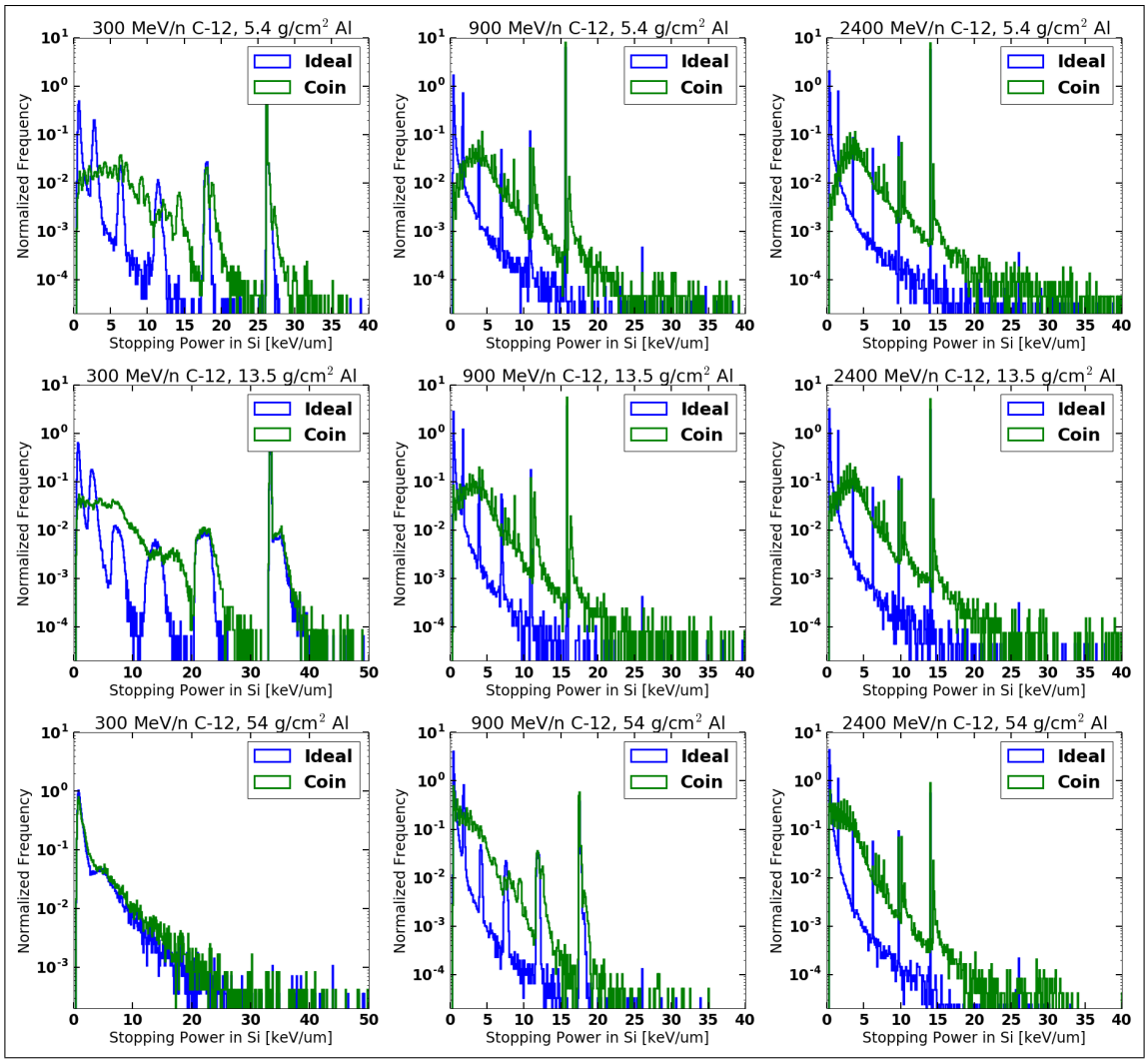

Figure 4.17: Stopping power distributions is Si for 5 cm pixel vs ideal for incident C ions of 300, 900 and 2400 MeV/n after 5.4 g/cm^2, 13.5 g/cm^2, 54 g/cm^2 of Al shielding

Figure 4.18 shows the distributions of stopping power for incident silicon ions for the different energy and shielding thickness combinations. These plots have many of the same features as the carbon plots. Lower Z ions combine to smooth out the lower stopping power peaks. Additionally, these lower Z ions combine with the higher Z fragments to add "tails" to the ideal stopping power peaks. Tails in this context refers to the additional structure that extends to the right or higher stopping power side of each ideal peak. The 300 MeV/n and 13.5 g/cm^2 shielding case, in which the incident ion and its higher Z fragments did not make it through the shield, shows a large increase in the frequency of stopping power above 15 keV/μm. This increase leads to an increased

dose mean stopping power for the 5 cm pixel size while the similar style plot at 900 MeV/n and 54 g/cm^2 shielding shows a decrease in dose mean stopping power.

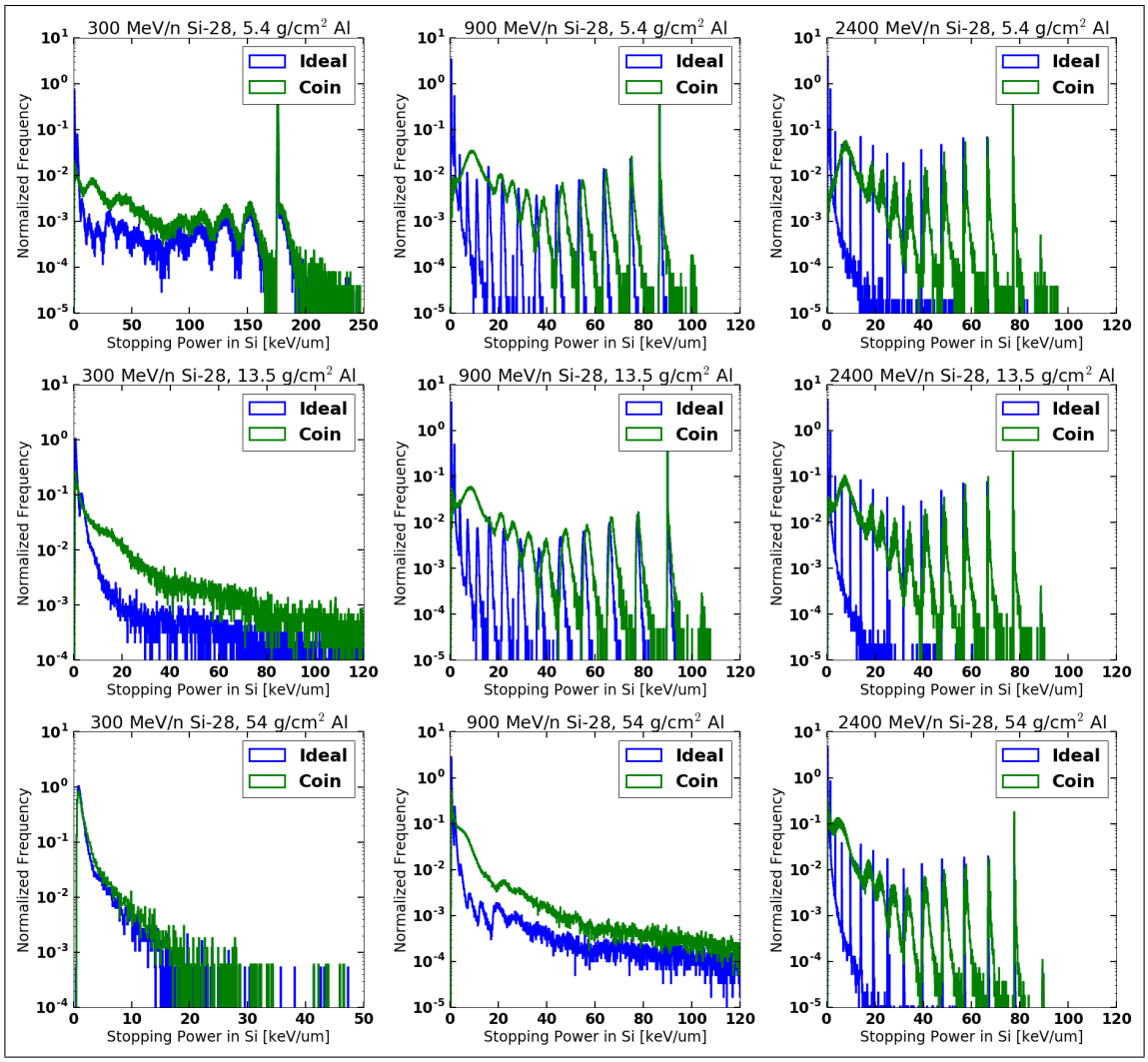

Figure 4.18: Stopping power distributions is Si for 5 cm pixel vs ideal for incident Si ions of 300, 900 and 2400 MeV/n after 5.4 g/cm^2, 13.5 g/cm^2, 54 g/cm^2 of Al shielding

Table 4.7 summarizes the dose mean stopping power for the different pixel sizes. Comparing the ideal case to the 5 cm pixel case shows that the dose mean stopping power sometimes increased while other times it decreased. There is no clear reason why this happened at some energy and shield combinations while it didn't at others. However, there is a tendency for the dose mean stopping power of coincident events to increase when the incident ion did not have sufficient

energy to exit the shield. Examples of the increase in coincident dose mean stopping power when compared to the ideal can be seen in the 300 MeV/n energy and 13.5 and 54 g/cm^2 cases. In contrast, the dose mean stopping power of coincident events tended to decrease for ions with higher incident energies. Percent error in the dose mean stopping power was as large as 33% for these cases with most percent errors between 5 and 10%. Overall these errors are larger than the incident helium and carbon cases. Similar to the helium and carbon cases, the errors in dose mean stopping power introduced by a large pixel size can be eliminated by selecting a pixel size of 0.1 cm. At a pixel size 0.1 cm, the difference between the stopping power of the ideal and coincident case are negligible.

Table 4.7: Dose mean stopping power [keV/μm] for incident Si ions for the ideal, 5 cm pixel and 0.1 cm pixel cases in silicon of varying energies. 5.4 g/cm^2, 13.5g/cm^2, 54 g/cm^2 Al shielding and 10 cm downstream

	300 MeV/n			900 MeV/n			2400 MeV/n		
	Ideal	5 cm	0.1 cm	Ideal	5 cm	0.1 cm	Ideal	5 cm	0.1 cm
5.4 g/cm^2	170.1	165.5	170.1	83.2	79.9	83.2	74.0	71.8	74.0
13.5 g/cm^2	67.0	73.8	67.0	81.2	72.7	81.2	69.3	62.9	69.3
54 g/cm^2	4.9	6.5	4.9	139.3	101.4	139.3	45.8	31.1	45.8

The distributions of stopping power for incident Fe ions are shown in Figure 4.19. Firstly, these plots highlight how complex the fragmentation spectra and associated distributions of stopping power are for high Z and high E ions. Iron, with a Z of 26 and mass number of 56, can fragment into many different ion combinations. The large numbers of fragments produced leads to many coincident events. Although the plots are more complex, many of the same features already discussed for the other incident ions are visible in the plots. When compared to the previous lighter ions the changes in the distributions are magnified, especially at the lower energy stopping powers of the distribution. The peaks of ions below a Z of approximately 8 or 9 can no longer be resolved in most cases.

Table 4.8 summarizes the dose mean stopping power for the different pixel sizes. Similar to the previous discussion for incident silicon ions, the dose mean averages tend to increase for

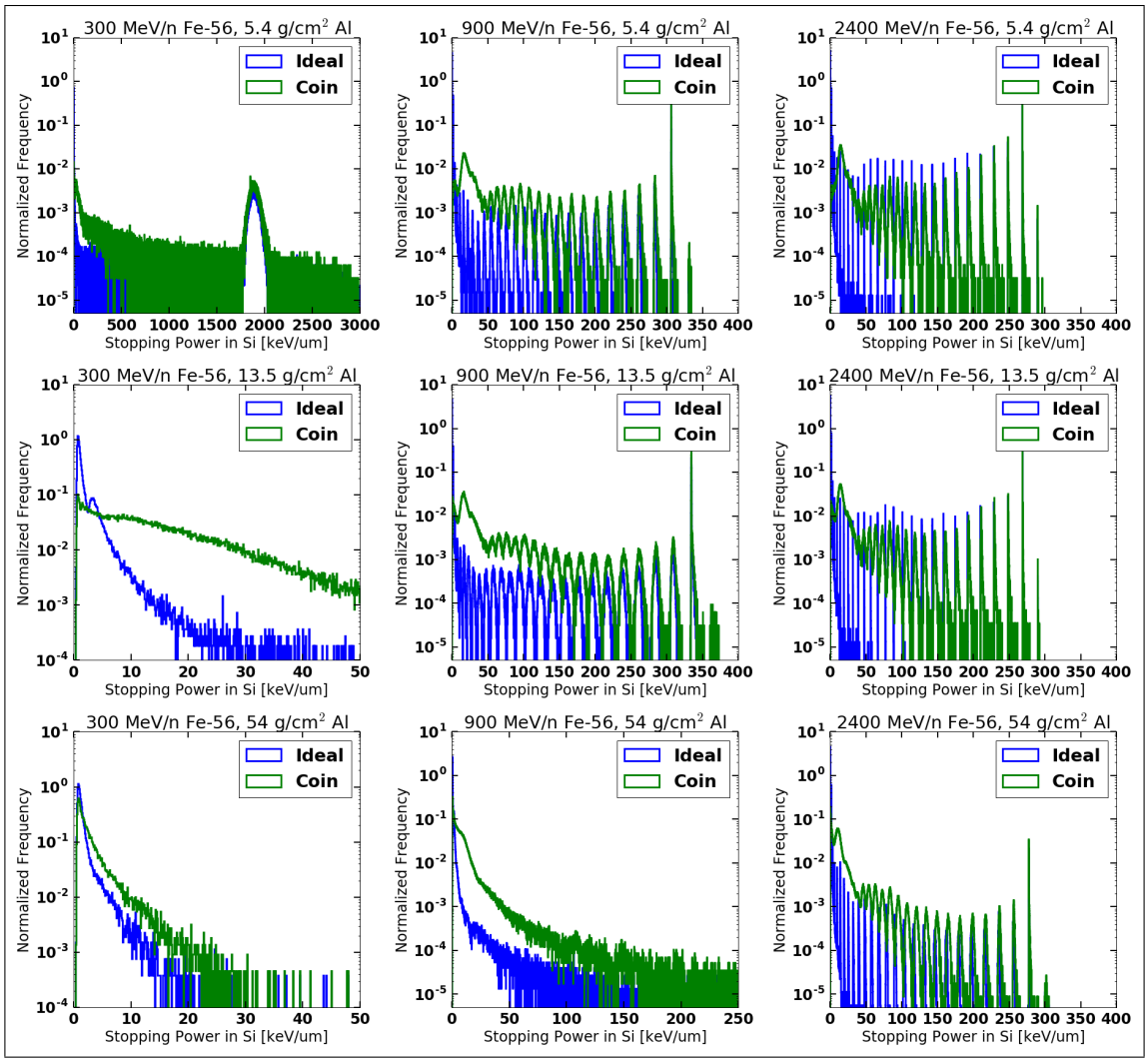

Figure 4.19: Stopping power in Si distribution for incident Fe ions of 300, 900 and 2400 MeV/n after 5.4 g/cm^2, 13.5 g/cm^2, 54 g/cm^2 of Al shielding

the situations where the incident ions are less likely to transmit through the shielding. When the incident ions easily transmits through the shielding, the dose mean average tends to decrease. The percent difference error for the cases where the incident ion transmits through the shielding is the highest of all the ions tested with a maximum of 161% and many over 30%. The smallest percent difference was 4% for the unique case of the 300 MeV/n ion incident on 5.4 g/cm^2 shielding. However, reduction of the pixel size to 0.1 cm eliminated almost all of the errors from coincident events.

Table 4.8: Dose mean stopping power [keV/μm] for incident Fe ions for the ideal, 5 cm pixel and 0.1 cm pixel cases in silicon of varying energies. 5.4 g/cm^2, 13.5g/cm^2, 54 g/cm^2 Al shielding and 10 cm downstream

	300 MeV/n			900 MeV/n			2400 MeV/n		
	Ideal	5 cm	0.1 cm	Ideal	5 cm	0.1 cm	Ideal	5 cm	0.1 cm
5.4 g/cm^2	1857	1776	1857	294	273	294	258	245	258
13.5 g/cm^2	15.7	41.2	15.8	302	248	302	243	206	242
54 g/cm^2	4.1	6.9	4.1	35.6	43.6	35.6	170	89.9	169.8

4.3 Spatial resolution conclusions

The analysis of particle proximity and coincident events showed that large errors in stopping power can be introduced if an active radiation detection system is not properly segmented. Segmentation of a detector system to a size of 0.1 cm was proposed and confirmed to mitigate the errors of coincident events. While this analysis was only done on a subset of the GCR spectrum, it is reasonable to assume that these results can eliminate the coincidence issue in the full GCR environment. With a pixel size of 0.1 cm, it is highly likely that a detection system is measuring single particles as opposed to coincident events.

A general method has been developed to determine the appropriate pixel size needed to remove coincident events. This method can be applied to different incident spectrum and shielding configurations. The results of this chapter also highlight the potential measurement errors of previous detection systems that lacked segmentation.

Chapter 5

Detector energy resolution

5.1 Detector energy resolution methods

The general and specific experimental setup for investigation of energy resolution was discussed in Section 3.3.1 and 3.3.6. For investigation of energy resolution, the idealized detector system with a virtual detector was changed to the physical detector system with a real detector. As opposed to the virtual detector, the real detector records the energy deposition as particles pass through the detector.

The path length each particle takes through the detector can vary due to the angle of incidence. In order to compare the simulation output of the physical detector system to the idealized detector system, the method for converting energy deposition to stopping power must be specified. For this work, the stopping power was determined as the total energy deposited in the detector divided by the standard thickness of the detector, 300 μm.

An important distinction for this chapter is that the total energy deposited in the real detector is not pulled from tabulated results, as it was for the virtual detector. Energy deposition in the detector took into account the specific physics packages and range cuts discussed in Section 3.2.1. This subtle but important distinction introduces energy straggling in the detector as described in Section 2.1.5.

Figure 5.1 shows results from an initial experiment to verify energy straggling based on the physics package selection for the physical detector system. The plots clearly show characteristic "long-tailed" distributions common of energy straggling. The shape of the distributions of stopping power, shown in Figure 5.1, changes based on the incident ion and incident energy. The results of these experiments confirmed the work described by Bohr, Bethe, Bloch, Vavilov and Landau discussed in Section 2.1.5. If the spatial resolution of a detector is chosen to mitigate coincident events, energy straggling effects will limit the accuracy of the stopping power measured by a

real detector. Identification of particles, as described in Chapter 6, will be difficult without an understanding of the errors introduced by energy straggling.

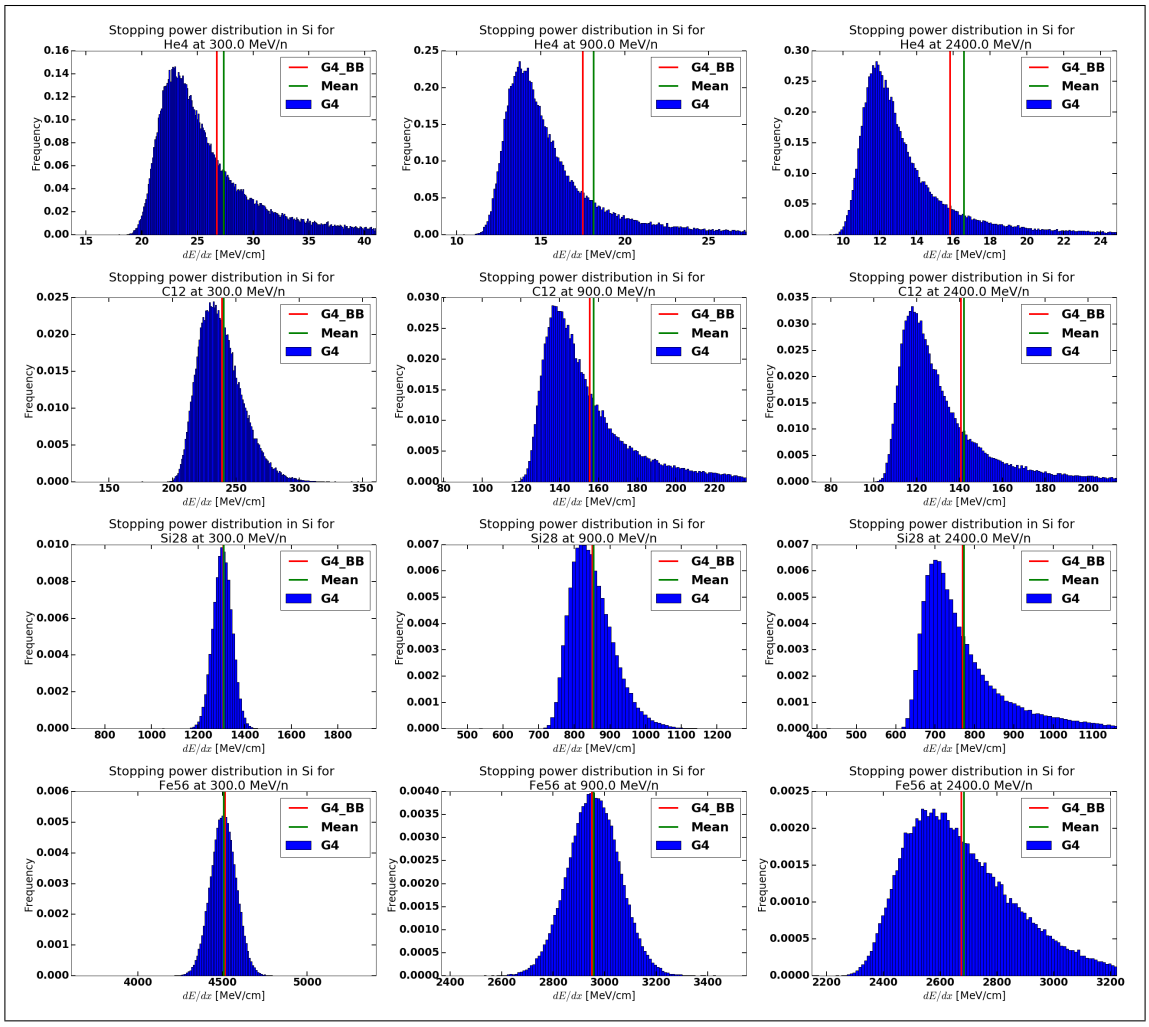

Figure 5.1: Results from initial simulation to verify energy straggling effects and physics package selection. These plots show the 4 ions and 3 energies used in the simulations incident on a 300 μm detector. No shielding was used before the detector in these cases. Bethe-Bloch and the mean of the distribution are also plotted for reference.

In addition to energy straggling, the conversion of stopping power in silicon to stopping power in tissue equivalent material (water) was investigated. The background of this conversion was discussed in Section 2.6. The methodology to investigate this conversion factor was simple. The ideal stopping power in silicon and water was recorded for every ion incident on the detector. These stopping power values, also stored in the idealized detector system, were kept in the physical

detector system simulations to perform this analysis. The ratio of stopping powers was simply taken and plotted. The results of this analysis are presented in Section 5.2.2.

5.2 Detector energy resolution results

5.2.1 Distributions of stopping power in real detectors

The distribution of stopping power for the physical detector system with real detectors are presented in this section, as well as the dose mean stopping power for all combinations of incident ion, energy and shielding thickness. The dose mean stopping power for both the physical detector system and the idealized detector system are presented for comparison.

The distributions of stopping power for incident He ions, including the effects of energy straggling, are shown in Figure 5.2. In comparison to the results discussed in Chapter 4, on the effects of coincident events, these plots show distinct differences. First, the low energy stopping power peak from protons is not reduced or shifted over as it was for coincident events. Second, when compared to the ideal spectra, the primary peaks now show visible energy straggling. The effects of energy straggling on the spectra of these plots can be identified by first noticing the ideal peak location. In all cases the peak of stopping power measured by the real detector is shifted to the left of the ideal peak. Additionally, the distribution extends far to the right of the ideal peak and has a characteristic long tail as described in Chapter 2 and shown in Figure 5.1 of this chapter.

The dose mean stopping powers for incident helium ions are summarized for the ideal and real cases in Table 5.1. For the 300 MeV/n incident helium ions, the dose mean stopping power shows minimal difference between the two cases. As the energy of the incident helium increases the percent error from the ideal case increases. Looking again at the non-shielded energy straggling distribution in Figure 5.1, this result makes sense. The larger the energy of incident He ion the more pronounced the energy straggling effects are. The percent difference for the 900 MeV/n and 2400 MeV/n cases range from 13% to 71%. These results further confirm that once pixel size is appropriately selected landau effects can introduce large errors the distributions of stopping power.

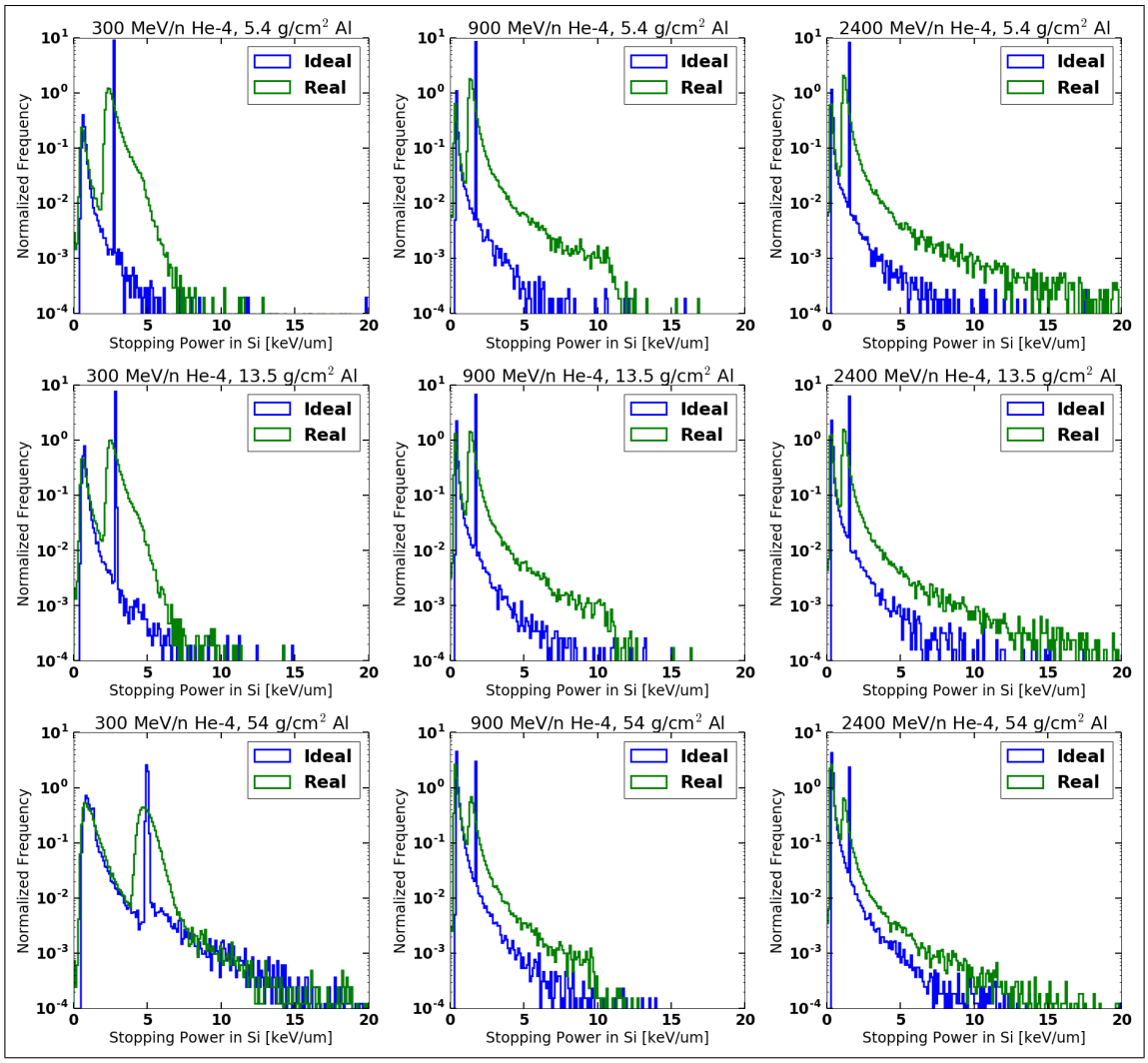

Figure 5.2: Distributions of stopping power in silicon for incident helium ions of 300, 900 and 2400 MeV/n after 5.4 g/cm^2, 13.5 g/cm^2, 54 g/cm^2 of Al shielding. The ideal stopping power as measured by a virtual detector are plotted along with the stopping power measured in a real detector.

Distributions of stopping power for incident carbon ions are shown in Figure 5.3. The characteristic effects of energy straggling are clearly seen in the 900 and 2400 MeV/n cases. As expected, the peaks of the real distribution are shifted to the left of the ideal peaks and display a long tail. The lowest energy, 300 MeV/n, and thickest shield, 54 g/cm^2, plot shows little structural change in the spectrum. The other 300 MeV/n plots have more normally shaped peaks consistent with the energy straggling distribution plot in Figure 5.1.

Table 5.2 summarizes the dose mean stopping powers for the various energy and shielding combinations. In general, the percent difference change in the dose mean stopping power is less

Table 5.1: Dose mean stopping power [keV/μm] in silicon for the ideal and real case for incident helium ions of varying energies after 5.4 g/cm^2, 13.5g/cm^2, 54 g/cm^2 Al shielding. The physical detector system is 10 cm downstream from the back of the shielding

	300 MeV/n		900 MeV/n		2400 MeV/n	
	Ideal	Real	Ideal	Real	Ideal	Real
5.4 g/cm^2	2.80	2.82	1.93	2.26	2.24	3.50
13.5 g/cm^2	2.80	2.85	1.96	2.22	1.93	3.30
54 g/cm^2	4.63	4.62	1.47	1.75	1.42	2.27

than that found for incident helium ions. This is primarily due to the fact that the stopping power values are larger. The percent difference change between the ideal and real cases are below 14% in all situations. Lower energy incident ions vary by less than 3% between the real and ideal cases. Similar to the results for incident helium ions, the real detector measurements provide an overestimation of dose mean stopping power. This overestimation is greatest at the highest incident energy of 2400 MeV/n.

Table 5.2: Dose mean stopping power [keV/μm] in silicon for the ideal and real case for incident carbon ions of varying energies after 5.4 g/cm^2, 13.5g/cm^2, 54 g/cm^2 Al shielding. The physical detector system is 10 cm downstream from the back of the shielding

	300 MeV/n		900 MeV/n		2400 MeV/n	
	Ideal	Real	Ideal	Real	Ideal	Real
5.4 g/cm^2	25.50	25.56	15.08	15.55	13.52	15.06
13.5 g/cm^2	31.38	31.30	14.49	14.76	12.75	14.14
54 g/cm^2	7.36	6.97	11.66	11.72	8.36	9.48

Distributions of stopping power for incident silicon ions are shown in Figure 5.4. These plots show that as the charge Z of the incident ion increases the resultant spectra start to lose the distinct peak structure found in the ideal plots. Peaks of lower Z fragments are closely spaced and combine to form a "smoothed out" distribution. This smoothing effect is more distinct as energy increases. Similarly to the helium and carbon plots, the stopping power distributions show little difference when the incident ions are stopped in the shield.

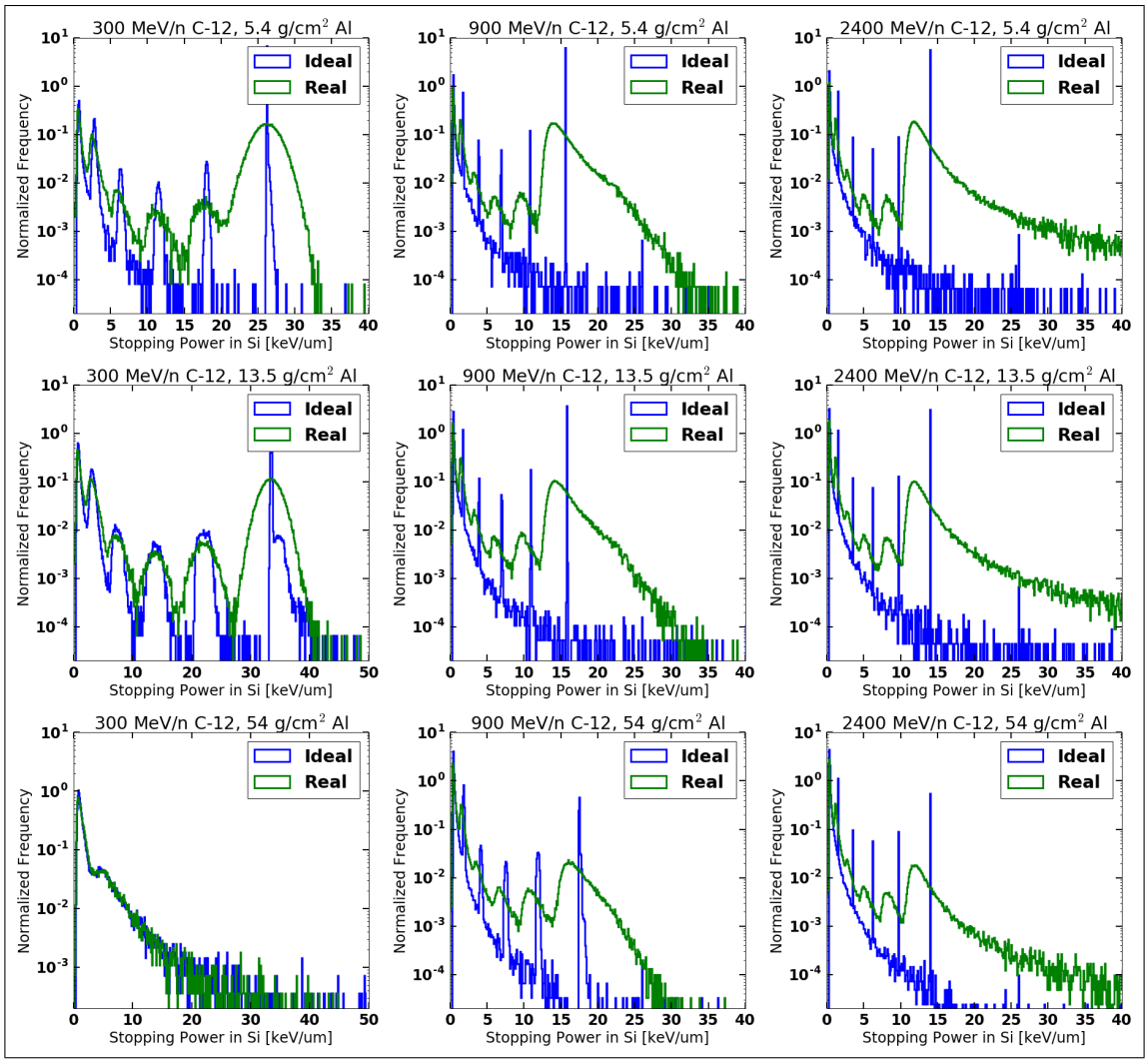

Figure 5.3: Distributions of stopping power in silicon for incident carbon ions of 300, 900 and 2400 MeV/n after 5.4 g/cm^2, 13.5 g/cm^2, 54 g/cm^2 of Al shielding. The ideal stopping power as measured by a virtual detector are plotted along with the stopping power measured in a real detector.

The dose mean stopping powers are summarized in Table 5.3 for the different energy and shielding combinations. The results for incident silicon ions show the dose mean stopping power can vary by as much as 16% for these cases. The values for the 300 MeV/n energy and 13.5 g/cm^2 shielding case show a unique result where the spectrum looks relatively unchanged but the dose mean values are 16% different. The table also shows that there is no clear trend for when the real detection system will over or under estimate the dose mean average. The complex nature of the secondary fragment ions, their energy and associated energy straggling make it difficult to make

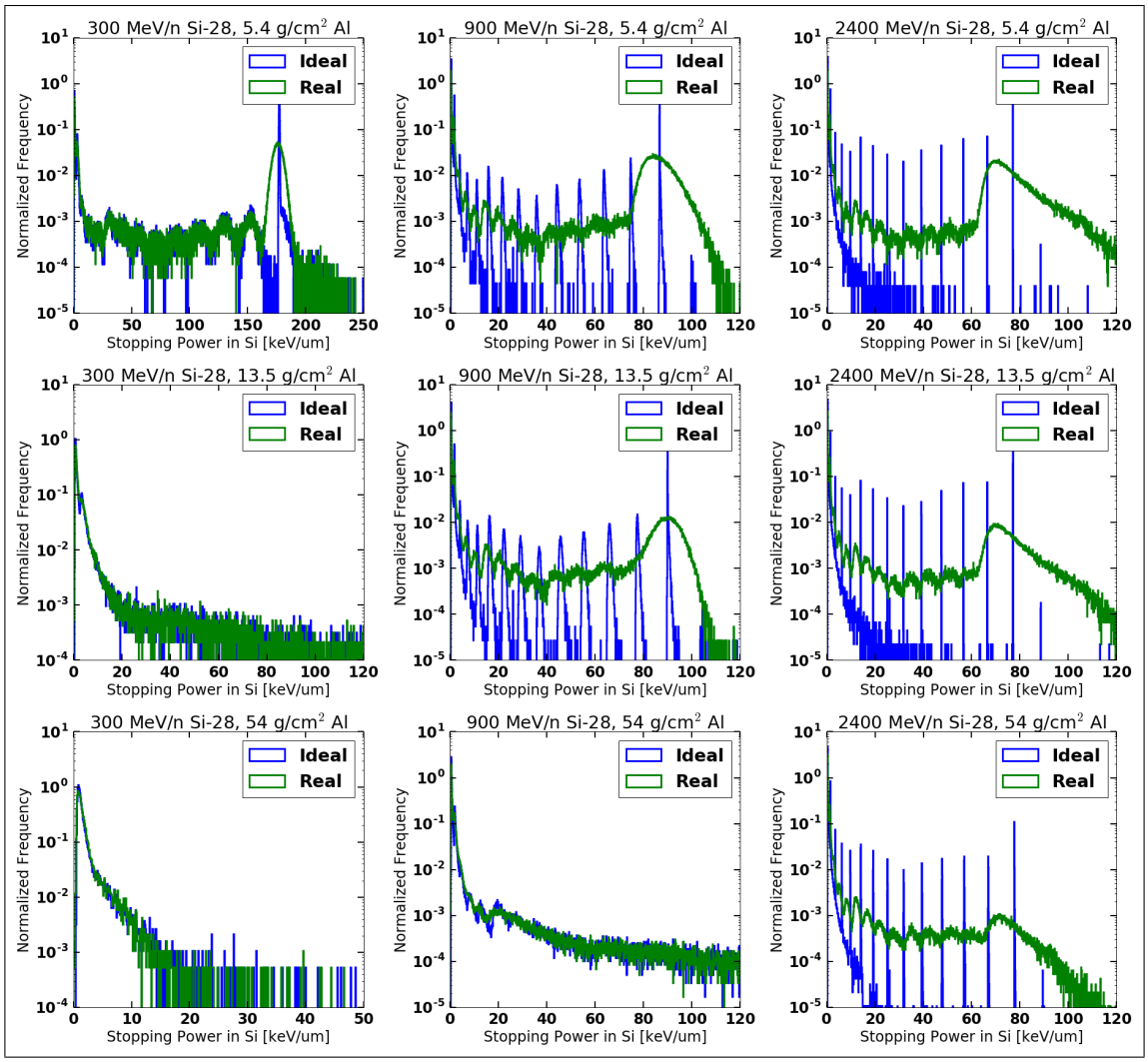

Figure 5.4: Distributions of stopping power in silicon for incident silicon ions of 300, 900 and 2400 MeV/n after 5.4 g/cm^2, 13.5 g/cm^2, 54 g/cm^2 of Al shielding. The ideal stopping power as measured by a virtual detector are plotted along with the stopping power measured in a real detector.

statements about general trends. Based on these results, it is not possible to assume whether a real detector will under or over estimate the dose mean stopping power.

The plots for the final incident ion of this section, iron, are shown in Figure 5.5. These plots show all of the same features discussed earlier. Iron with its large Z of 26 and its secondaries and greater order fragments make these spectra very flat due to the numerous overlapping long tailed distributions of lighter ions. While looking at the ideal spectrum, it is possible to easily identify the different Z fragments. However, a real detector system renders this much more challenging.

Table 5.3: Dose mean stopping power [keV/μm] in silicon for the ideal and real case for incident silicon ions of varying energies after 5.4 g/cm^2, 13.5g/cm^2, 54 g/cm^2 Al shielding. The physical detector system is 10 cm downstream from the back of the shielding

	300 MeV/n		900 MeV/n		2400 MeV/n	
	Ideal	Real	Ideal	Real	Ideal	Real
5.4 g/cm^2	171.39	170.14	83.20	83.52	74.08	75.57
13.5 g/cm^2	99.32	82.62	81.10	81.27	69.38	70.67
54 g/cm^2	5.38	4.91	146.33	133.97	46.09	46.75

Dose mean stopping power values are summarized in Table 5.4. These results are similar to those of the other incident ions in this study. While some energy and shielding combinations show little change in the dose mean stopping power, others show differences of up to 22%. For some combinations of energy and shielding thickness, the real detector overestimates the dose mean while in others it is underestimated.

Table 5.4: Dose mean stopping power [keV/μm] in silicon for the ideal and real case for incident iron ions of varying energies after 5.4 g/cm^2, 13.5g/cm^2, 54 g/cm^2 Al shielding. The physical detector system is 10 cm downstream from the back of the shielding

	300 MeV/n		900 MeV/n		2400 MeV/n	
	Ideal	Real	Ideal	Real	Ideal	Real
5.4 g/cm^2	2021	2108	294	294	258	259
13.5 g/cm^2	23.3	18.1	302	302	242	243
54 g/cm^2	4.3	3.9	39.0	35.8	169	169

5.2.2 Stopping power conversion results

The effects of coincident events and energy straggling on the stopping power spectra have been investigated in this paper but only apply to stopping power in silicon detection systems. Determination of the radiation risk to astronauts requires the conversion of stopping power in silicon to stopping power in biologically equivalent materials. This conversion has traditionally been done by the use of a single conversion factor. Given the uncertainties studied in the previous

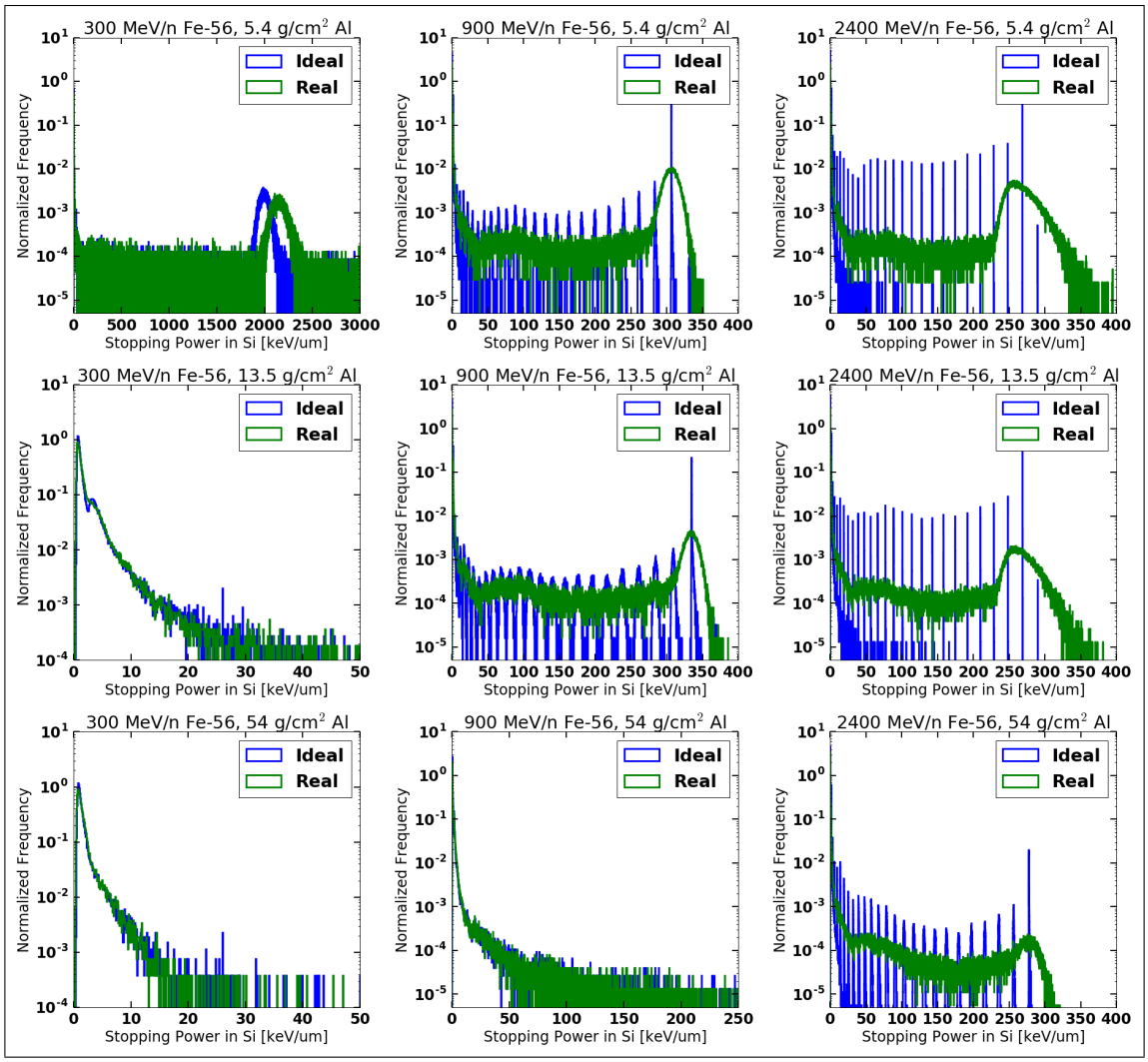

Figure 5.5: Distributions of stopping power in silicon for incident iron ions of 300, 900 and 2400 MeV/n after 5.4 g/cm^2, 13.5 g/cm^2, 54 g/cm^2 of Al shielding. The ideal stopping power as measured by a virtual detector are plotted along with the stopping power measured in a real detector.

section, it is important to know how large of an effect this conversion factor would introduce, and if it is appropriate to use a single value for this conversion.

Data from the real detector case, using all different shielding thicknesses, were used to investigate the ratio of stopping power in water to stopping power in silicon. Figure 5.6 shows a histogram of the stopping power ratios for all incident ion, energy and shielding combinations studied. As opposed to other plots above, this plot shows the absolute frequency of the values, with a total of over 26×10^6 individual ratios studied. The plot shows that the 5.4 g/cm^2 case has a distinct bi-modal distribution. Further investigation showed that the high ratio, greater than 0.6, cases could

be identified as belonging to the very high LET, low energy Fe particles with incident energy of 300 MeV/n that emerged from the 5.4 g/cm^2 thickness aluminum shielding. These low energy Fe ions were not able to transmit through the thicker shields. This unique case can be considered to be an artifact of the particular ion, energy and shielding thickness. At the shielding thicknesses of 13.5 g/cm^2 and 54 g/cm^2, little difference is seen between the distributions and dose mean values.

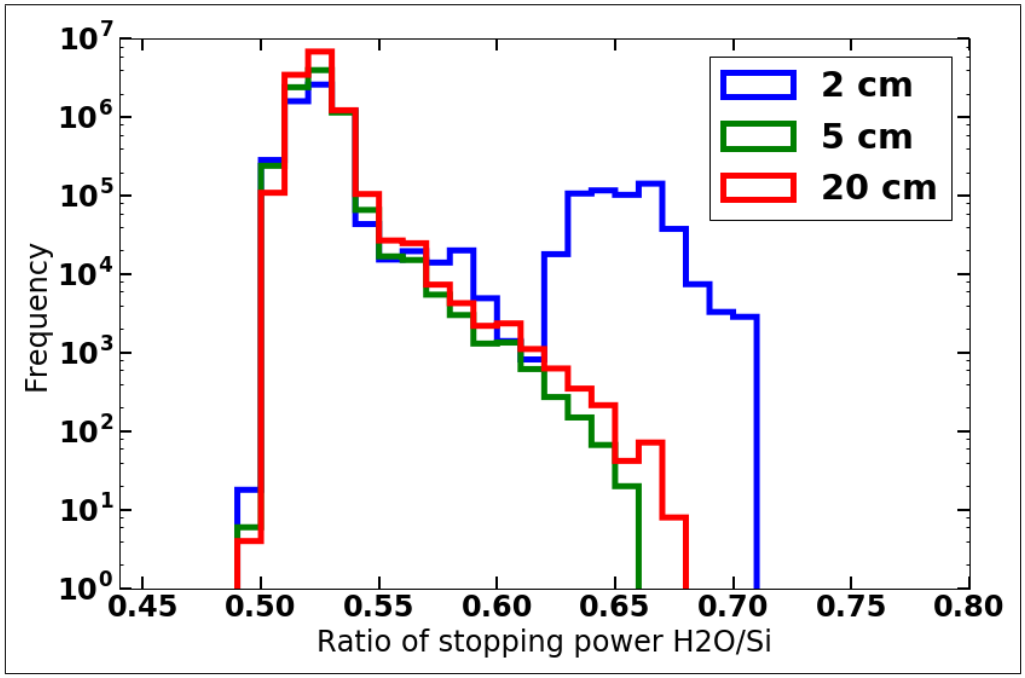

Figure 5.6: Histogram showing the frequency of the ratios of stopping power in water vs silicon

The mean ratios for the distributions are provided in Table 5.5 and show that a reasonable single factor to convert stopping power in silicon to that in water for these applications would be 0.53. This value is lower than the those quoted by Zeitlin et al. In 2010, Zeitlin et al. quoted a value of 0.56 (Zeitlin et al., 2010). While in 2013, Zeitlin et al. used a value of 0.625 (Zeitlin et al., 2013).

This conversion factor can be used if there is a desire to compute radiation quality factors, but it is important to note that errors on the order of the other errors discussed will be introduced by assuming one value. It would be more appropriate to assign conversion factors based on particle charge and energy. This could be accomplished by extending some of the machine learning work presented in Chapter 6.

Table 5.5: Table of mean stopping power ratio, stopping power in water over stopping power in silicon for the various shielding thicknesses simulated

Shielding thickness	Mean stopping power ratio
5.4 g/cm^2	0.535
13.5 g/cm^2	0.524
54 g/cm^2	0.524

5.3 Energy resolution conclusions

This chapter investigated errors in the estimation of stopping power when a real detector is used. These errors are due to the random probabilistic nature of energy deposition in thin detectors. The results show that energy straggling will present significant challenges to the accurate measurement of stopping power. In contrast to coincident events, the effects of energy straggling cannot be mitigated easily. Energy straggling resulted in larger errors in the measurement of stopping power than coincident events. The effects of energy straggling on the dose mean values are also less intuitive and more challenging to explain. Moreover, Section 5.2.2 showed that the stopping power measured in a silicon detector must be carefully converted to stopping power in biologically relevant materials.

Chapter 6

Ion classification with machine learning

6.1 Introduction

As discussed in Chapter 1, one goal of this work was to determine if it is possible to identify the charge Z of individual particles incident on a radiation detection system. The ability to identify individual particles will be important for the use of the updated NASA quality factors discussed in Section 2.4.3. The methods of machine learning were chosen for the task of particle identification. These methods were applied to the output data generated from the simulations described in Section 3.3.6.

The chapter is structured differently from the others. First, the basic background of machine learning techniques is presented in Section 6.2. Radiation specific machine learning applications are reviewed in 6.2.1. Similar to the other chapters, the methods used for the analysis are discussed in Section 6.3, with specifics on the algorithm presented in Section 6.3.1. Results are then presented in Section 6.4, with conclusions from this study discussed in 6.5.

6.2 Background

A machine learning algorithm is a computational process that attempts to learn how to achieve a desired goal without being explicitly programmed to do so. These algorithms have the possibility to learn over many repetitions similar to human beings. The foundations of machine learning have a rich history in computer science, artificial intelligence, statistics and mathematics. The ideas of artificial intelligence, the foundation of machine learning, were most famously discussed by Alan Turing in his 1950 paper titled "Computing Machinery and Intelligence" (Turing, 1950).

Early applications of machine learning focused on tasks such as learning to play checkers (Samuel, 1959). Eventually these methods became powerful enough to defeat the then-reigning world champion in chess in 1997 (Campbell et al., 2002). Machine learning has continued to

progress and is now used extensively in a large variety of research and industry areas, such as self driving cars and computer aided diagnosis in medicine.

The goal of this work was to investigate if techniques of machine learning could be applied to identification of particle charge Z. The spatial resolution results of this work showed that it is possible to segment a detection system to ensure individual particles are being measured. The energy resolution results showed that energy straggling will pose significant challenges for any detection system. The problem then becomes, can a machine learning model correctly identify the charge of a particle Z based only on the energy deposition in a detector, including energy straggling effects.

The challenges an algorithm will face can be summarized by looking at Figure 6.1. The plot on the left shows the stopping power for six representative ions computed by the Bethe-Bloch method discussed in Chapter 2. The dotted line represents a perfect measurement of stopping power and shows that a single measurement could lead to multiple different ion classifications. However, for higher energy particles, the stopping power of different ions are sufficiently differentiated to allow for identification. However, the left plot assumes the stopping power could be perfectly measured. In the terminology of the previous sections, this would be representative of an idealized detector system. The plot on the right is representative of what the plot on the left would look like with energy straggling effects. Energy straggling will render identification even at high energies challenging.

6.2.1 Machine learning in radiation detection

Machine learning has been used in several applications related to radiation detection and radiation therapy. Kangas et al. used machine learning methods to reduce the number of false alarms reported by a portal monitor designed to identify illicit radioactive materials (Kangas et al., 2008). Machine learning has also been used in medical applications to quantify the prompt radiation produced after proton radiotherapy treatment (Gueth et al., 2013). Another medical application studied by Su et al., used machine learning methods to predict radiation-induced pneumonitis (Su

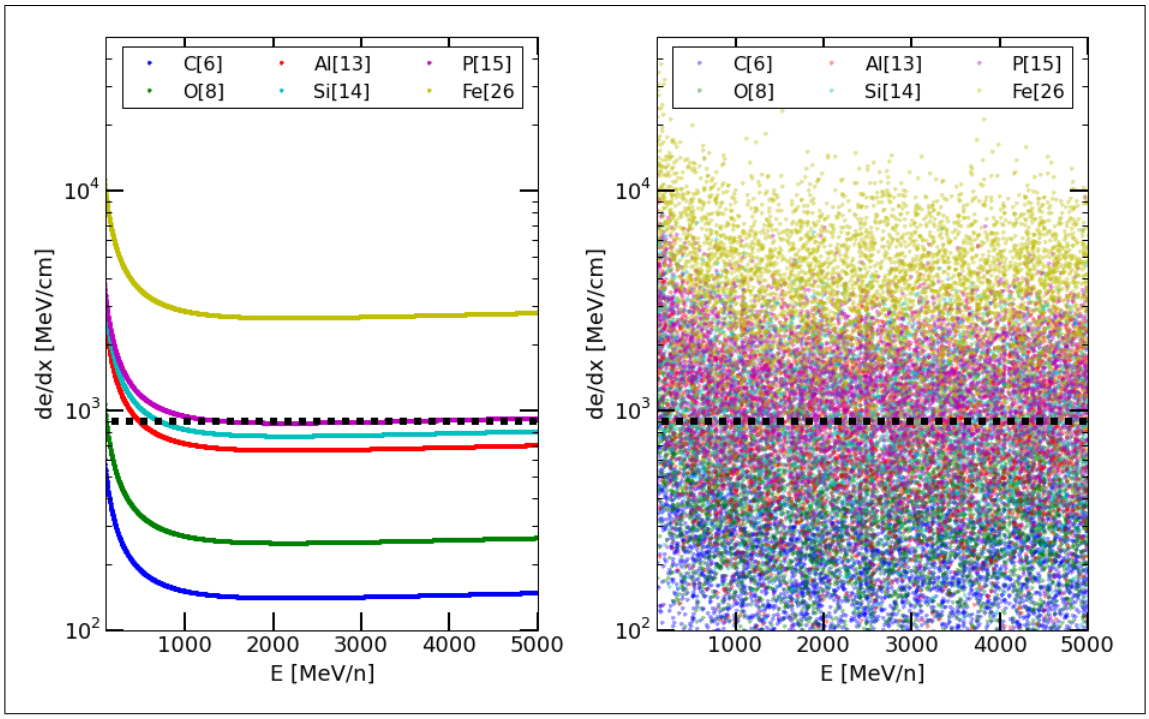

Figure 6.1: These two plots highlight the challenges a machine learning algorithm will face when trying to identify ions based on stopping power. The stopping power of six ions, based on the Bethe-Bloch formalism, are plotted as a function of energy in MeV/n. The dashed line is representative of a single measurement of stopping power. The plot on the left shows how an ideal detection system may identify the particle species based on stopping power. The plot on the right shows the challenges in identification when energy straggling is present.

et al., 2005). Additionally, machine learning has been used to look at secondary effects of radiation during prostate radiotherapy (Gulliford et al., 2004).

The use of machine learning in space radiation detection systems is more limited. The group working with the Timepix detector, discussed in Section 2.5, has published several papers on using machine learning to improve detection capabilities. However, to the author's knowledge, there have been no published results on specific classification performance, using machine learning, for individual ions present in the space radiation spectrum.

6.3 Machine learning methods

Machine learning methods can be categorized into three main groups; reinforcement learning, unsupervised learning and supervised learning. In reinforcement learning, the algorithm will in-

teract with a dynamic system in which it must reach a goal. The algorithm is provided feedback after interaction and learns based on this positive or negative feedback. Unsupervised learning attempts to learn features of the input data set with no guidance. In supervised learning, a data set that includes both input and the desired output are provided to the algorithm. The goal of the supervised learning algorithm is then to learn a general rule that can map the input to the output. This rule can then be applied to data sets where the output is unknown. Supervised learning was the method used for this work.

The larger category of supervised machine learning can be further broken down based on the type of output desired. In regression, the goal of the machine learning model is to predict a continuous variable. In classification, the goal of the model is to assign a class based on the input information. Multi-label classification predicts multiple possible classes based on the input data and is the focus of this work.

Outputs from the simulations described in Section 3.3.6 were used as input to the machine learning algorithm. This input data set consisted of the stopping power estimated by a real detector and the known particle charge Z. In the common language of machine learning, the data set contains two column vectors. The first column vector, the stopping power values, is considered the feature vector. While the second column vector, the particle charge Z, is considered the the target vector.

The use of a multi label classification algorithm can be split into two main stages: training and prediction. When developing models it is common practice to divide the data set available into a training and testing dataset. For this work, training was performed in a supervised manner using the training data set. Specifically, the information from the feature vector, stopping power, is used to train the machine learning algorithm to correctly classify the values in the target vector, particle charge Z. Once the algorithm is trained, additional measurements from the feature vector are used to predict the class. These predicted class values can then be compared to the actual class to determine the performance of the algorithm.

The Scikit-learn Python package, version 18.0 Sep 2016 release, was used for its ability to implement and study different machine learning algorithms quickly (Pedregosa et al., 2011). It also has the benefits of being open source and based on many of the Python tools already used previously in this work. Scikit-learn has implemented models for supervised learning, including classification and regression, unsupervised learning, and many pre-processing and model comparison tools. This work focused on the use of the supervised classification techniques and model evaluation metrics. In particular, the method of nearest neighbor based classification was tested.

6.3.1 Machine learning algorithm

Training and testing data sets were created from the full data set. Two thirds of the data were used for training while the other one third was used for testing. The data split was chosen so both the training and testing data set would have a sufficient number of lower probability events.

The *KNeighborsClassifier* algorithm, of the Scikit learn Python package, was used for classification of the data. This algorithm uses instance-based learning and does not attempt to create an analytical model. Classification is performed by computing a majority vote based on the nearest neighbor to each sample of the input data set.

The *KNeighborsClassifier* has several parameters that can be tuned. The most commonly adjusted parameter is the number of nearest neighbors the algorithm queries to perform the vote. The default value is 5 but for this work the value of 20 was used. The next tunable parameter is the weights of each value in the vote. The weights can be uniform, a function of the distance away or user defined. For simplicity, the classifier was run with uniform weights.

6.4 Results

Sections 3.3.1 and 3.3.6 described the two geometric setups for simulations: single and double detector. Results are broken into three sections. Some basic analysis on the simulation outputs, relevant to machine learning, are discussed in Section 6.4.1. Section 6.4.2 discusses the results of

the single detector machine learning study, while, Section 6.4.3 discusses the results from the two detector study.

6.4.1 Data set basics

Although the ions incident on shielding in these simulations were a subset of the GCR spectrum, the fragmentation products represent all ions from $Z = 1$ to $Z = 26$. The distribution of ions after passing though 2 cm of Al shielding is shown in Figures 6.2 and 6.3. Figure 6.2 is plotted on a linear scale and shows that the data set is dominated by a small number of ions.

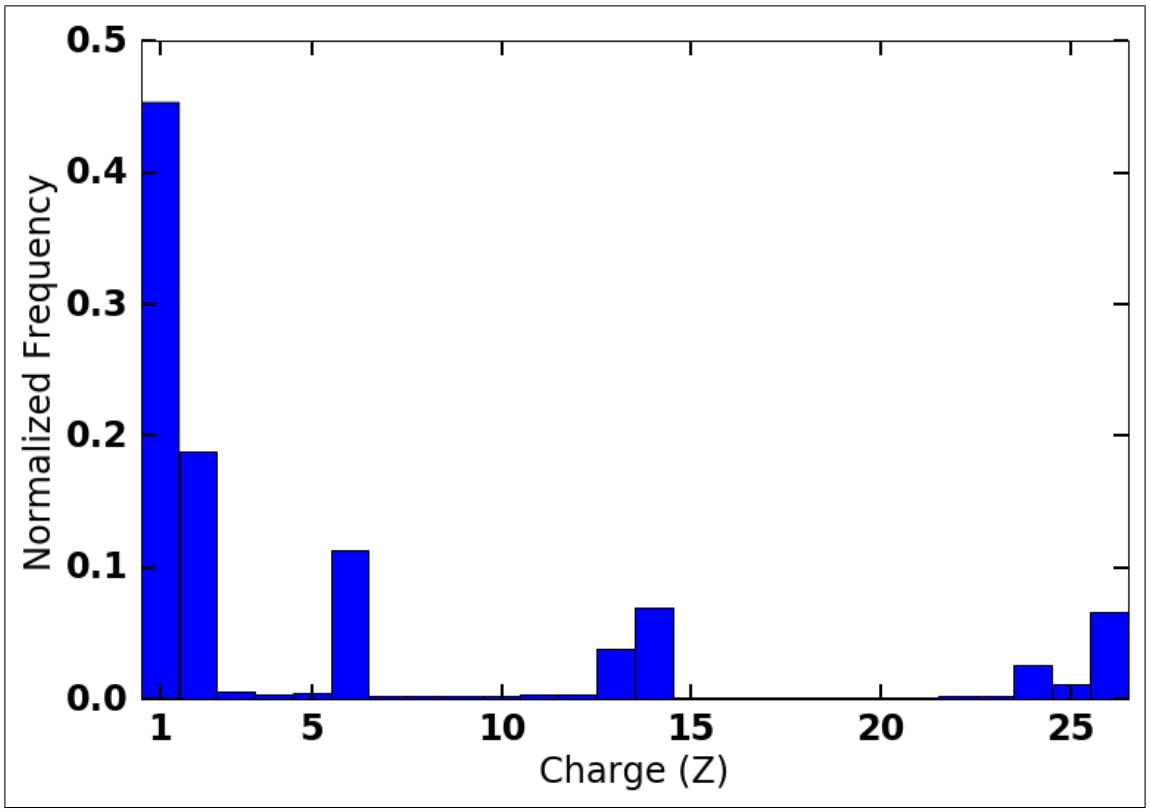

Figure 6.2: Histogram showing the normalized frequency of ion charge distribution used in these studies. In this plot the normalized frequency is plotted on a linear scale.

A large part of the data set, 45%, is composed of protons $Z = 1$. This is expected, as protons are created in abundance when higher Z ions fragment. Helium is the next largest fraction of the data set at just under 20%. The four incident ions selected for these simulations are also shown

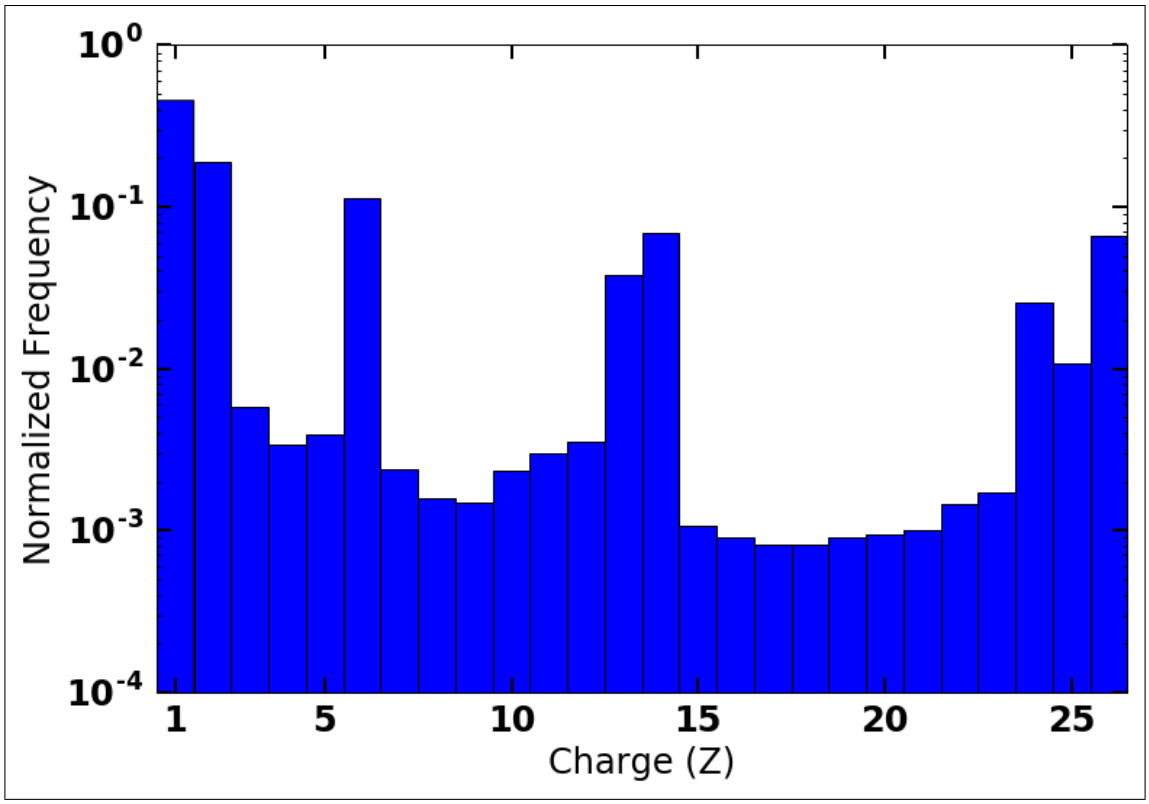

Figure 6.3: Histogram showing the normalized frequency of ion charge distribution used in these studies. In this plot the normalized frequency is plotted on a logarithmic scale.

with ion charges of $Z = 2, 6, 14, 26$. When plotted on a logarithmic scale all ions for $Z = 1$ to $Z = 26$ are visible. Although the distribution is not equivalent to that of the GCR, it is an appropriate testing set for the initial studies in this work.

6.4.2 Single detector machine learning

As highlighted in the previous sections of this chapter, the goal of the machine learning algorithm is to correctly classify the ion charge Z based on the energy deposited in a single detector. Figure 6.4 shows a scatter plot of the training information provided to the machine learning algorithm. The stopping power measured by the detector is plotted as a function of ion charge. The opacity of the markers on the plot is reduced to 1% of normal to highlight the most densely populated area.

A horizontal line drawn on Figure 6.4 would represent a single measurement of stopping power. It can be seen that a single measurement can lead to many different ion classifications. The *KNeighborsClassifier* algorithm was trained on two thirds of the dataset and tested on the remaining one third.

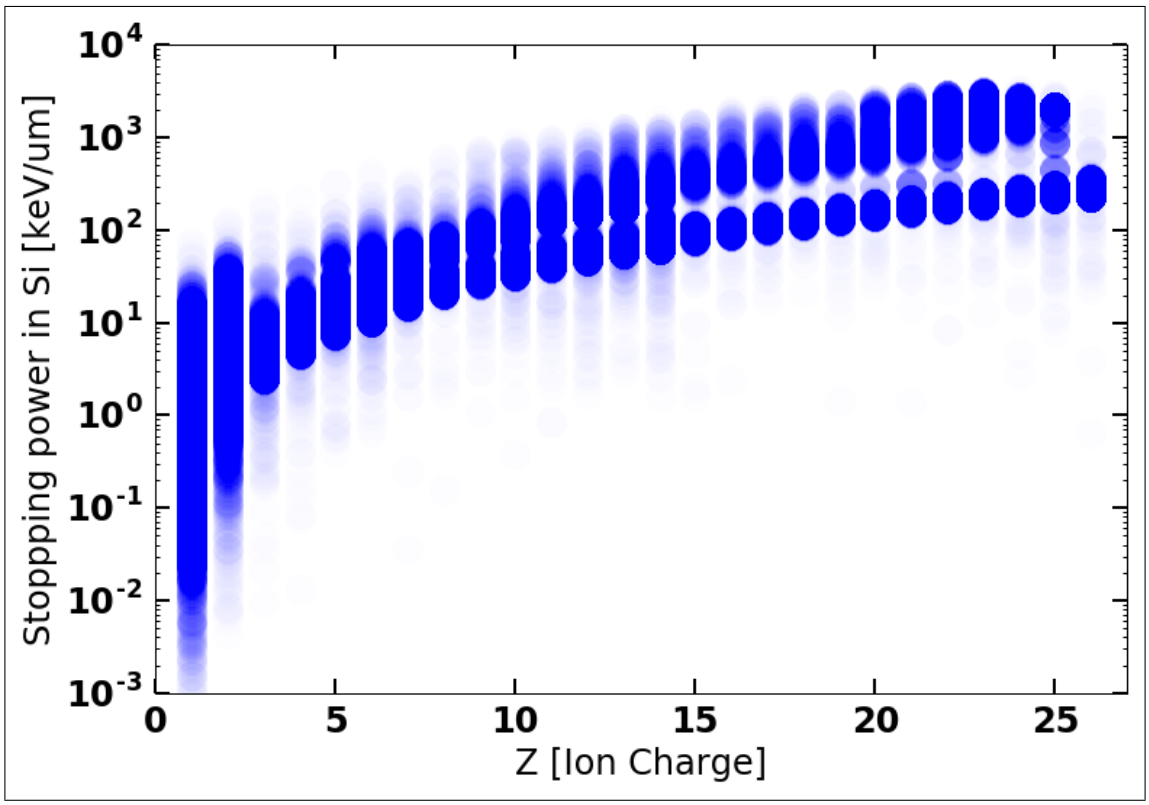

Figure 6.4: Scatter plot of the stopping power of individual particles in the detector with their associated ion charge. The opacity of the markers has been reduced to 1% of normal. This highlights the most densely populated areas of the plot and helps to reduce the prevalence of outliers.

The results of the algorithm applied to the testing set are shown in Figure 6.5. This figure, called a confusion matrix in the field of machine learning, shows the actual label along the columns of the plot and the predicted label along the rows. A machine learning algorithm that perfectly classifies the testing data set would have a confusion matrix that has highest probability along the diagonal of the plot, i.e., the only data in each column (actual) has values only in the corresponding row (predicted). Columns of the confusion matrix should add up to the total number of items or when normalized the value 1. Rows of the matrix are not restricted to adding up to 1 and are not on the

same scale due to the fact the they are normalized based on the number of items in each of the true classes. Insight into how the algorithm is classifying the data can be extracted from the plot.

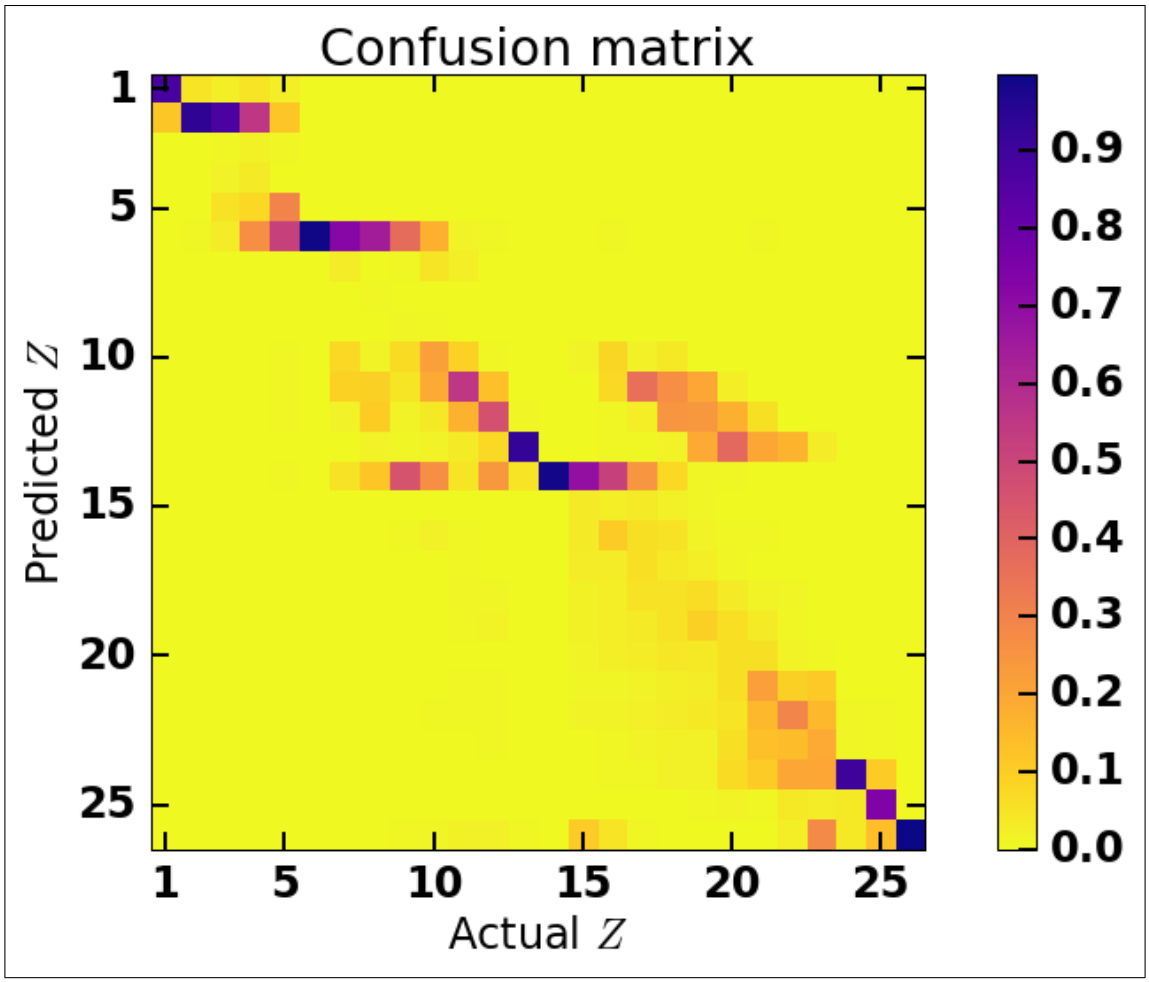

Figure 6.5: Confusion matrix for the one detector case. This plot shows the normalized percentage of classification with the predicted classification on the vertical axis and the actual classification on the horizontal axis.

Looking along the columns of Figure 6.5, the algorithm performed very well for ions of Z = 1, 2, 6, 13, 14, 24, 25 and 26. This is not surprising given the distribution of the data shown in Figures 6.2 and 6.3. The algorithm performed best on ions that had the most representative cases in the data set. Looking at the rows of Figure 6.5, the algorithm classified the data into 4 main groups; a low group for Z= 1 to 2, a group at Z = 6, a group from Z = 11 to 14, and a high group for Z above 20.

Looking at the low group, protons ($Z = 1$) and helium ($Z = 2$) ions were classified correctly almost all of the time. Ions with actual Z values of 3 and 4 were classified as 2 almost all of the time. Boron ions (Z = 5) were classified correctly approximately 40% of the time while being classified as carbon ($Z = 6$) the rest of the time. Ions with actual Z between 5 and 8 were classified as carbon $Z = 6$ in most cases. Interestingly, fluorine $Z = 9$, was classified as $Z = 14$ the majority of the time and $Z = 6$ the rest of the time.

Ions with actual Z between 11 - 14 were classified correctly more often than not while ions with Z of 15 and 16 were classified as silicon $Z = 14$ most often. For ions with actual Z between 16 and 22 the algorithm incorrectly classified the majority of the data. The confusion matrix shows that they were classified mostly to lower Z ions between 10 and 13. Ions with actual Z between 21 and 23 were classified correctly around 20% of the time. However, the predicted classes where generally classified as Z values within 2 of the correct class.

A histogram of the differences between the actual Z value and the predicted Z value is provided in Figure 6.6. This plot re-illustrates the effectiveness of the algorithm with the majority of the ions having no difference, with the next highest percentage within 2 of the actual classification. Although the histogram shows some values incorrectly classified by over 6, this only happened 0.1% of the time.

Output of the algorithm and performance metrics is summarized in Table 6.1. The three measures of performance listed in the table are precision, recall and the f1-score. The ability of the algorithm to correctly identify the charge (Z) of an ion, or predict the true positive results, is defined as the precision. In terms of the true positive tp and false positive values fp, precision is defined as:

$$Precision = \frac{tp}{tp + fp}. \tag{6.1}$$

Precision, with respect to this work, is the fraction of ions correctly classified as a certain Z value, over the total number of ions classified as that Z.

The ability of the algorithm to accurately classify each Z as that Z is the recall or sensitivity. In terms of the true positive tp and false negative values fn, recall is defined as

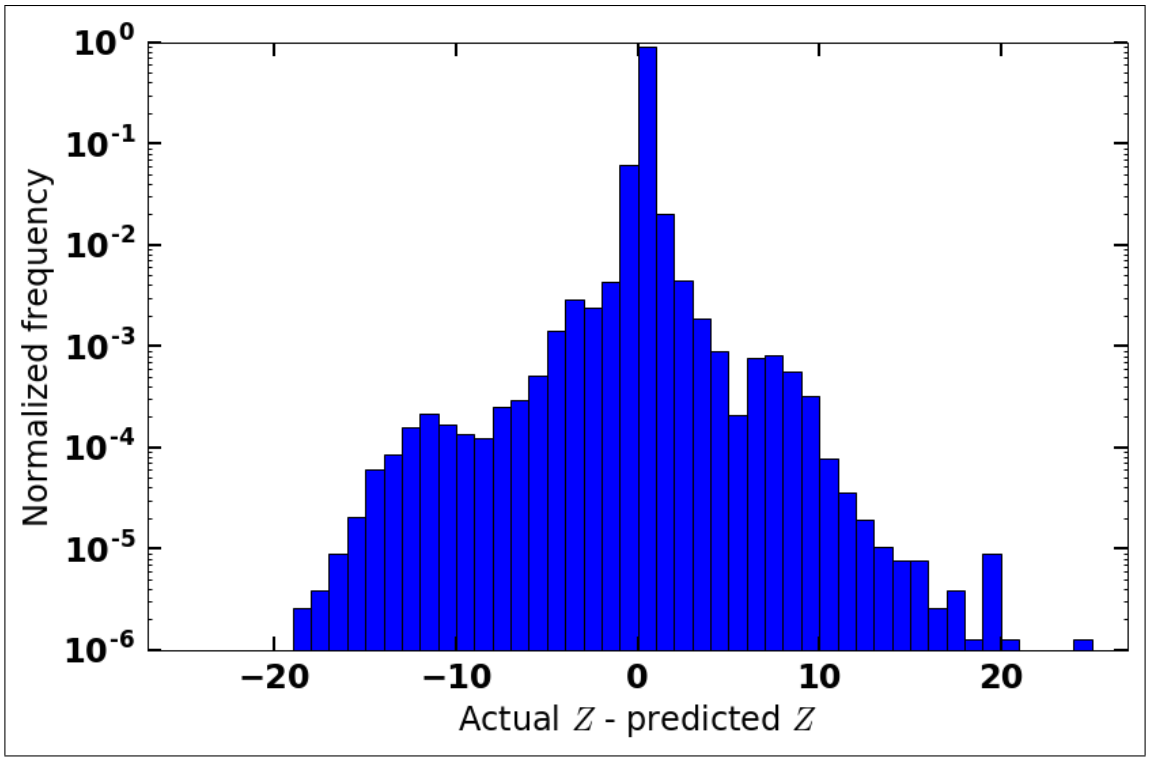

Figure 6.6: Histogram of the difference between the actual Z values and the predicted values. The frequency of events is normalized and the vertical axis is on a log scale.

$$Recall = \frac{tp}{tp + fn}. \tag{6.2}$$

The f1-score takes into account both precision and recall to provide a measure of the classification accuracy.

$$f_1 = 2 \cdot \frac{precision \cdot recall}{precision + recall}. \tag{6.3}$$

The f_1 score can also be interpreted as the weighted average of the precision and recall. Support is the number of instances of the Z value in the testing data set.

For the one detector case, the algorithm had an average precision, recall, and f1 score of 0.89, 0.90 and 0.89 respectively. This level of performance highlights that with a simplistic algorithm, using only the energy deposition events in a single detector, a large percentage of the ions can be correctly identified. In general, the algorithm performed better on ions that had more cases represented in the data set. This was expected based on the properties of the algorithm discussed

earlier. The performance summary also shows areas and particular ions with poor performance metrics. These areas can be further investigated to try and improve the performance at those specific Z values. The desire to improve the capabilities of the algorithm led to the two detector study in this work, presented in Section 6.4.3.

6.4.3 Dual detector machine learning

The two detector system is described in Section 3.3.6. The goal of the two detector system was to investigate if performance of the algorithm could be increased by adding an additional measurement of stopping power. In the language of machine learning this is considered adding an additional feature to the training data set. A scatter plot of the training data set is shown in Figure 6.7. Figure 6.7 is a scatter plot with the stopping power in the first detector along the vertical axis and the stopping power in the second detector along the horizontal axis. The color in the figure corresponds to the charge Z of the ion.

General clustering of the data based on the charge can be seen with lower Z ions depositing less energy in both detectors while higher Z ions deposited more energy. The variance of energy deposition for the two detector system is also much higher for lower Z ions than for higher Z ions. Additionally, the color of the points shows that there is considerable overlap in the distribution of each ion. Many of the points are grouped along the diagonal of the plot which corresponds to similar energy deposition in both of the detectors.

The confusion matrix plot for the two detector case is shown in Figure 6.8. In contrast to the one detector case shown in Figure 6.5, the two detector case shows a much better visual agreement of the data along the diagonal of the plot. The diagonal of the confusion matrix represents cases when the predicted class was the actual class. Looking across the columns of the confusion matrix, the class with highest frequency was generally equivalent to the actual Z. Some exceptions to this were the cases of Z = 7, 8, 9, 16 and 20. Ions with a Z of 7, 8 were classified down to carbon $Z = 6$. While fluorine ($Z = 9$) was classified as either Z = 6, 10 or 15.

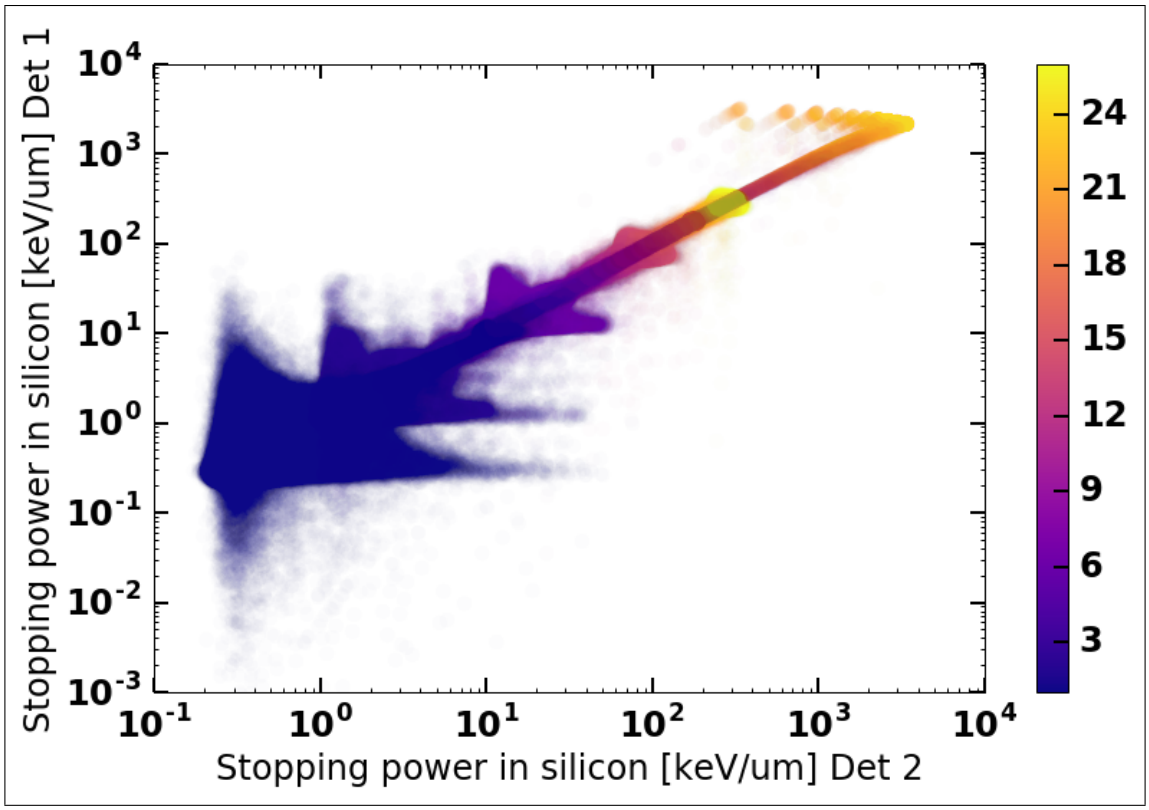

Figure 6.7: Scatter plot of the stopping power of individual particles in each detector. The stopping power measured in the first detector is plotted along the vertical axis. While the stopping power measured in the second detector is plotted along the horizontal axis. The color of each point represents the ion charge Z. The opacity of the markers has been reduced to 1% of normal and a color based on the ion charge has been added.

Ions that were incorrectly classified are closer to their correct classification value than the one detector case. Furthermore, there are less distinct groupings of the classifications. The difference between the true classification label and the predicted classification label, shown in Figure 6.9, was also reduced in the two detector case. The range of the difference in misclassification was reduced along with the overall frequency.

The algorithm's performance for the two detector case is summarized in Table 6.2. Overall, the summary shows an increase in all three performance metrics. Ions such as Z = 4, 8, 9 and 15 increased in recall values from near zero to above 10 percent. For the two detector case, the algorithm had an average precision, recall, and f1 score of 0.92, 0.93 and 0.92 respectively. Ions

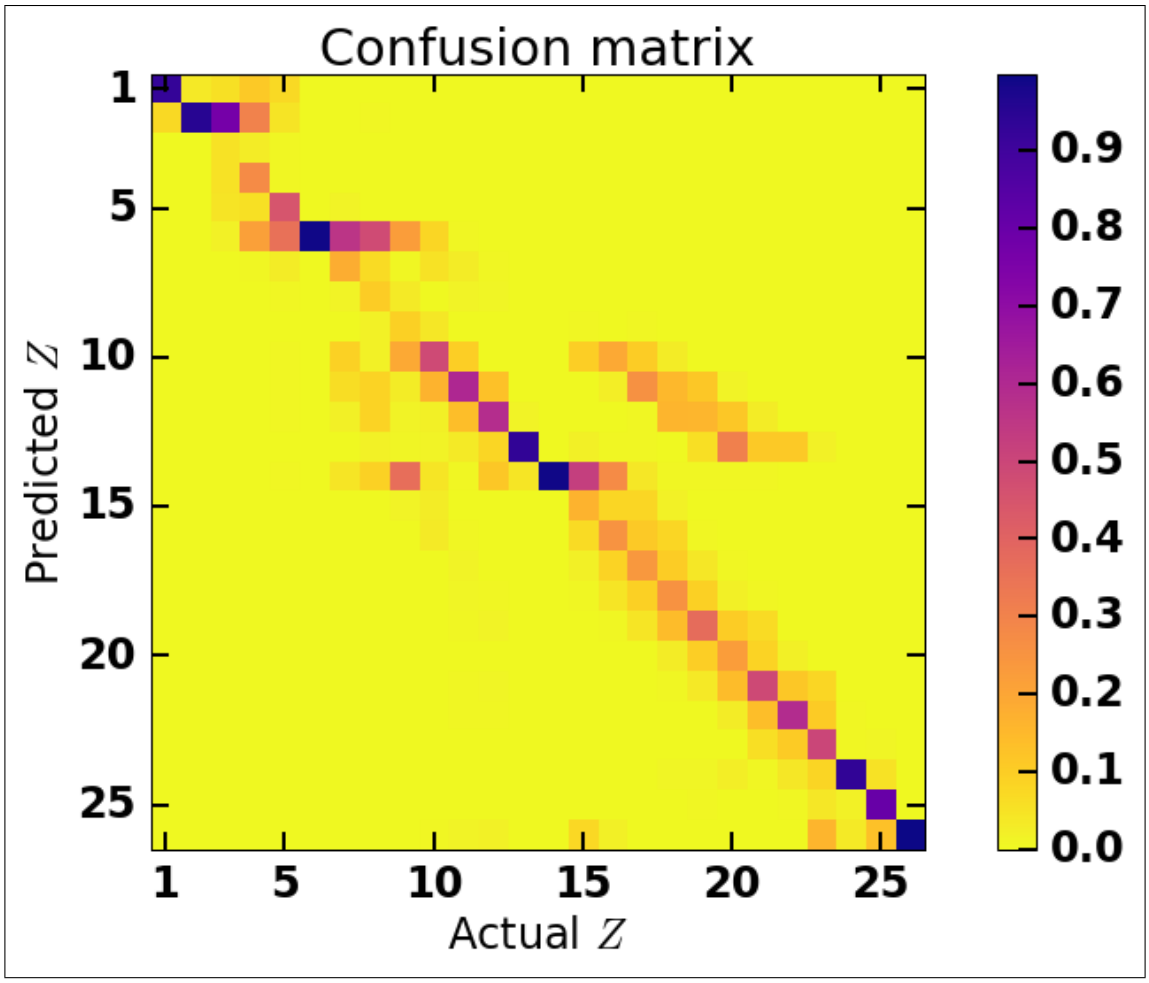

Figure 6.8: Confusion matrix for the two detector case. This plot shows the normalized percentage of classification with the actual classification on the horizontal axis and the predicted classification on the vertical axis.

that performed well in the one detector case also performed well in the two detector case, often showing an increase in precision and recall.

6.5 Machine Learning Conclusions

The precision, recall and f1-score for the single and double detector system as a function of ion charge Z are plotted in Figures 6.10, 6.11 and 6.12. Without exception the precision, recall and f_1-score increased from the one to the two detector case. For ions with low classification precision in the one detector case (less than 30%), the precision doubled for the two detector case. Ions that

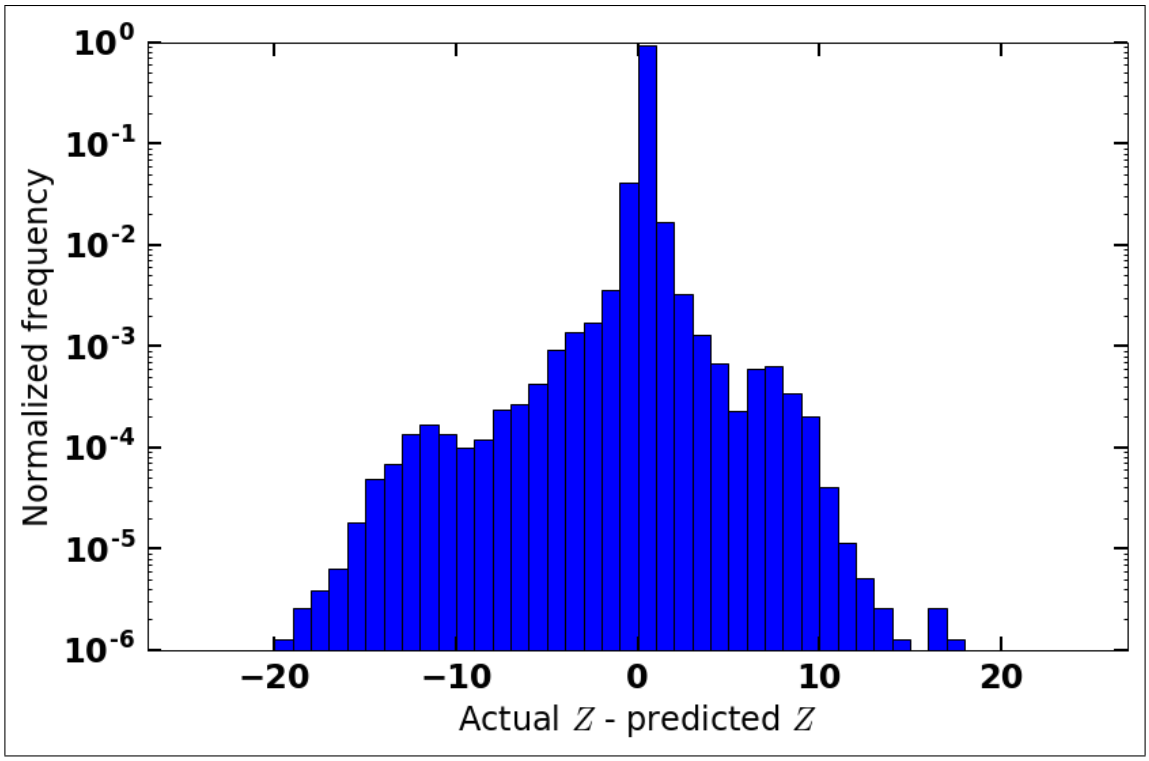

Figure 6.9: Histogram of the difference between the true Z value and the predicted values for the two detector case. The frequency of events is normalized and the vertical axis is on a log scale.

exhibited good precision in the one detector case had marginal but distinct increases in precision for the two detector case.

Similar to the precision, ions with good recall in the one detector case had small but noticeable increases in the two detector case. The recall plot also highlights the low recall for some ions. While this recall was greatly increased for the two detector case, the recall still remained low for some ions. Ions with poor recall were less represented in the data set and were more often classified as neighboring ions with higher support. In terms of radiation protection metrics, such as the NASA quality factor, a mis-classification by one or two Z may not introduce significant error into risk estimations.

By definition, the f_1 score is a weighted average of the precision and recall. The f_1 plot shows many of the same features of the recall and the precision plots. Overall, the f_1 plot shows increased performance for the two detector case when compared to the one detector case.

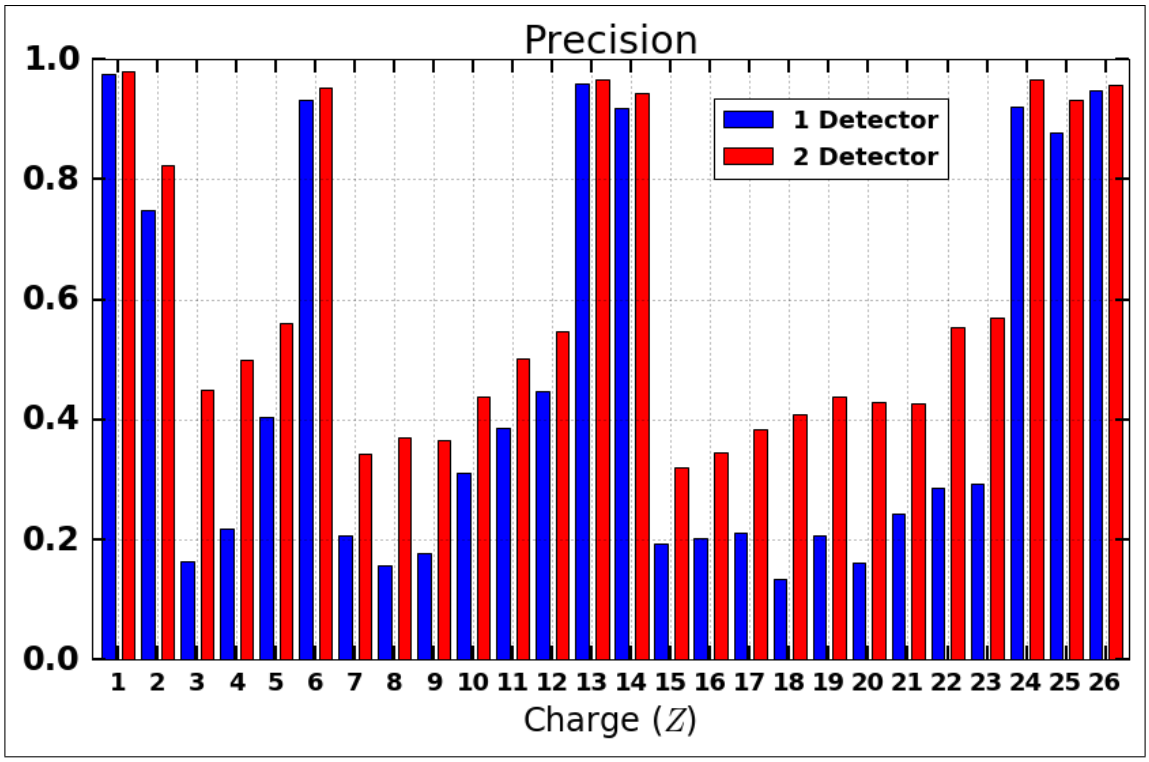

Figure 6.10: Machine learning algorithm precision plotted as a function of ion charge for the one and two detector case. Precision was increased without exception from the one detector case to the two detector case.

The above machine learning results show that it is possible to accurately and reliably identify ions using a simple stopping power detector. One criticism of this study could be that the data set is highly unbalanced and that the good results are only due to this fact. For some problems, this result could be concerning and an example of the algorithm over fitting. However, in this case the GCR and associated spectra behind shielding will always be unbalanced. Good performance in this case does not limit the algorithm's abilities in real world situations. Further investigation with a full GCR data set in different shielding conditions should be done to extend these results. Additionally, the effects of incorrect classification on risk assessment, such as the use of the NASA quality factor, should be studied. With regard to quality factors, this work shows that the majority of the time ions can be correctly classified. If they are not correctly classified they are often classified as a neighboring ion, which should have small effects in the calculation of quality factors.

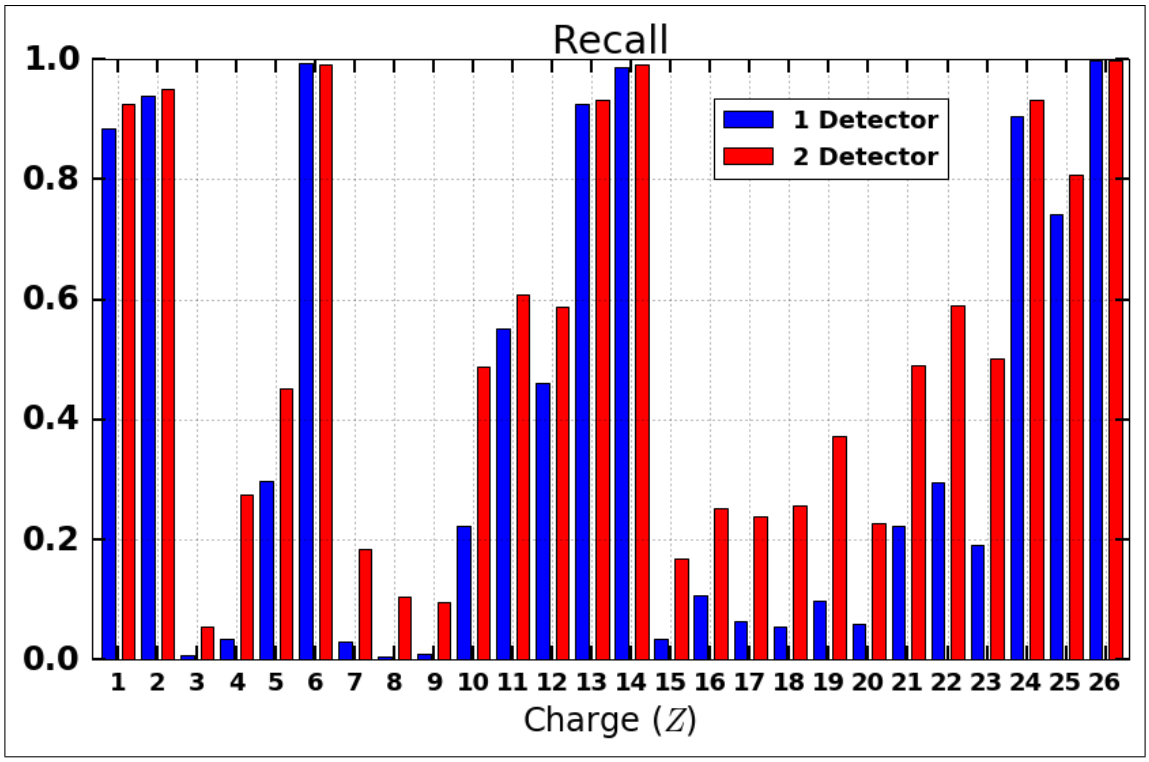

Figure 6.11: Machine learning algorithm recall plotted as a function of ion charge for the one and two detector case. Recall was increased without exception from the one detector case to the two detector case.

Table 6.1: Performance summary of the machine learning algorithm for the single detector case.

Z	precision	recall	f1-score	support
1.0	0.98	0.88	0.93	353564
2.0	0.75	0.94	0.83	147196
3.0	0.16	0.01	0.01	4559
4.0	0.22	0.03	0.06	2605
5.0	0.40	0.30	0.34	2985
6.0	0.93	0.99	0.96	88198
7.0	0.21	0.03	0.05	1818
8.0	0.16	0.00	0.01	1256
9.0	0.18	0.01	0.02	1170
10.0	0.31	0.22	0.26	1806
11.0	0.39	0.55	0.45	2309
12.0	0.45	0.46	0.45	2790
13.0	0.96	0.93	0.94	29366
14.0	0.92	0.99	0.95	53600
15.0	0.19	0.03	0.06	799
16.0	0.20	0.11	0.14	672
17.0	0.21	0.06	0.10	626
18.0	0.13	0.05	0.08	642
19.0	0.21	0.10	0.13	671
20.0	0.16	0.06	0.08	678
21.0	0.24	0.22	0.23	732
22.0	0.29	0.29	0.29	1102
23.0	0.29	0.19	0.23	1331
24.0	0.92	0.90	0.91	20091
25.0	0.88	0.74	0.80	8304
26.0	0.95	1.00	0.97	50871
avg / total	0.89	0.90	0.89	779741

Table 6.2: Performance summary of the machine learning algorithm for the two detector system.

Z	precision	recall	f1-score	support
1.0	0.98	0.93	0.95	353564
2.0	0.82	0.95	0.88	147196
3.0	0.45	0.05	0.10	4559
4.0	0.50	0.28	0.35	2605
5.0	0.56	0.45	0.50	2985
6.0	0.95	0.99	0.97	88198
7.0	0.34	0.18	0.24	1818
8.0	0.37	0.11	0.16	1256
9.0	0.36	0.10	0.15	1170
10.0	0.44	0.49	0.46	1806
11.0	0.50	0.61	0.55	2309
12.0	0.55	0.59	0.57	2790
13.0	0.97	0.93	0.95	29366
14.0	0.95	0.99	0.97	53600
15.0	0.32	0.17	0.22	799
16.0	0.34	0.25	0.29	672
17.0	0.38	0.24	0.29	626
18.0	0.41	0.26	0.31	642
19.0	0.44	0.37	0.40	671
20.0	0.43	0.23	0.30	678
21.0	0.43	0.49	0.46	732
22.0	0.55	0.59	0.57	1102
23.0	0.57	0.50	0.53	1331
24.0	0.97	0.93	0.95	20091
25.0	0.93	0.81	0.87	8304
26.0	0.96	1.00	0.98	50871
avg / total	0.92	0.93	0.92	779741

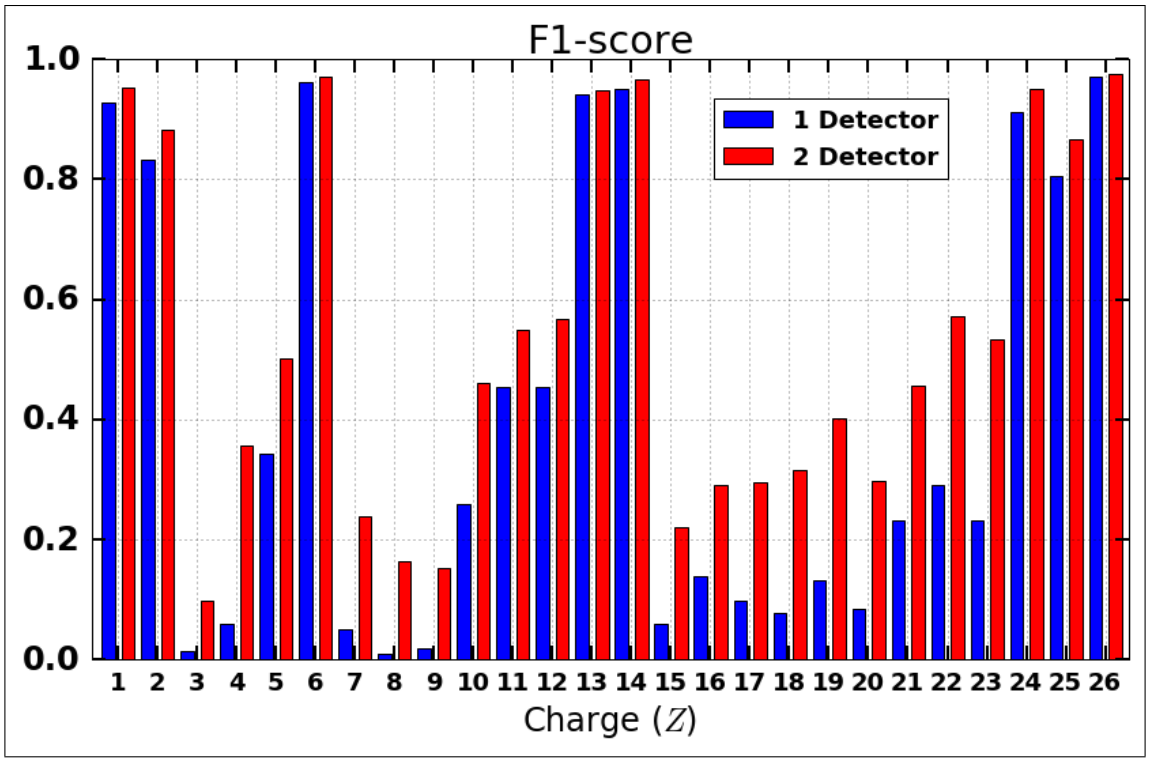

Figure 6.12: Machine learning algorithm f_1 score plotted as a function of ion charge for the one and two detector case. The f_1 score was increased without exception from the one detector case to the two detector case.

Chapter 7

Conclusion

In this dissertation, the requirements for radiation detection and analysis systems to meet future radiation protection objectives for missions beyond low earth orbit were studied. This is important because existing space dosimetry systems do not satisfy the new paradigms of risk assessment proposed by NASA (Cucinotta et al., 2013) and discussed in Section 2.4.3. Specifically, this dissertation investigated the required detector spatial resolution, the effects of energy straggling and dose conversion on estimations of stopping power, and methods for ion identification.

Chapter 4 quantified the measurement error that results from coincident events in a detection system. First, the proximity analysis methods analyzed the spatial resolution or detector pixel size necessary to reduce the number of coincident events in a detection system. The results of the proximity analysis for various experimental conditions recommend a pixel size of no more than 0.1 cm to ensure that single events are being measured with high probability. Next, the stopping power spectra were shown for various incident ions, shielding conditions and detector pixel sizes. It was shown that detection systems without appropriate segmentation, such as those used on previous space missions, are subject to error in the measurement of stopping power from coincident events. Dose mean stopping power values for the recommended pixel size 0.1 cm were then shown to be nearly equivalent to those of an idealized detector system.

A detection system that is designed to measure individual particles, i.e., has appropriate spatial resolution, will also need to have appropriate energy resolution. Energy resolution in thin detectors will be limited by the variance in stopping power due to energy straggling. Energy straggling in thin detectors is also unavoidable and cannot be eliminated unless thicker detection systems are used. Measurements of stopping power in silicon will also need to be converted to stopping power in biologically equivalent materials, i.e., LET. The effects of energy straggling and conversion of stopping power from silicon to water were discussed in Chapter 5. Plots of the stopping power spectra for the idealized detector system were compared to those of the physical detector system.

The results confirmed that energy straggling will render the accurate determination of stopping power challenging. The errors introduced into estimates of stopping power after conversion from silicon to water were also presented, and a conversion factor of 0.53 was proposed.

Chapter 6 presented results of the classification of ion charge based on detector measurements. Results were promising for a single detector system using a basic machine learning algorithm. Further improvements were made with the addition of a second detector. Although lower probability ions were not as accurately classified, the results of these methods are very encouraging.

This study provides insight into the specific design requirements for future space radiation detection systems. In contrast to the highly segmented Timepix detection system and the work of Pinsky et al., the spatial resolution results of this study shows that a highly pixelated detection system may not be necessary. This work also confirms and quantifies the known effects of energy straggling in thin detectors.

To the knowledge of the author, this is the first study to propose and confirm the ability of a machine learning algorithm to classify ions using a simple radiation detection system. The identification methods significantly expanded on previous work by classifying a spectrum that includes ions from $Z = 1$ to 26. This study, to the author's knowledge, is the first to make specific recommendation on detector design based on the revised NASA radiation protection paradigm.

The results from this work can be used to assist in the creation of the next generation of radiation detection systems. Future radiation detection systems used beyond low earth orbit will need to measure the individual velocity and ion charge of HZE ions in a complex field. It will be possible to create cost effective radiation detection systems that meet these needs by utilizing the results of this work. In particular, the methods of machine learning show tremendous promise for the identification of particle charge Z. Machine learning methods may also help with the conversion of stopping power in silicon to water.

The results of this work can also be applied to the field of heavy ion radiation therapy. In the context of heavy ion therapy, accurate detection of the fragmentation spectra produced from clinical beams will be important for routine quality assurance. In addition, patient specific dosimetry

verification may be possible with a combination of detector and machine learning analysis methods.

The proximity analysis results are encouraging but should be further validated under additional shielding conditions and with the complete GCR spectrum incident on the shielding. Similarly, the classification results are promising but should also be validated further. Classification will be more difficult as more closely spaced data points are added to the spectrum. Future work could use significantly more sophisticated machine learning techniques to handle these challenges. We believe that machine learning techniques will eventually be capable of accurately identifying ions in all situations. Further work is also needed to determine how sensitive radiation risk assessment models are to incorrect classification of ions.

In summary, the main results of this dissertation are as follows:

- Pixel size on the order of 0.1 cm is appropriate to ensure that coincident events do not change the measured stopping power.
- With appropriate pixel size, the next major influence on errors is energy straggling effects.
- If it is important to estimate the stopping power in biological media (LET), and compute quality factors, the values measured by a silicon detector will need to be adjusted. An adjustment factor based on Z or energy is recommended. If a single adjustment factor is to be used, the data suggest it should be a value of 0.53.
- Machine learning techniques are capable of identifying particles using basic detector designs. These results can be expanded and have potential for full spectrum classification using cost effective detector designs.

Bibliography

Sea Agostinelli, John Allison, K al Amako, J Apostolakis, H Araujo, P Arce, M Asai, D Axen, S Banerjee, G Barrand, et al. Geant4âĂŤa simulation toolkit. *Nuclear instruments and methods in physics research section A: Accelerators, Spectrometers, Detectors and Associated Equipment*, 506(3):250–303, 2003.

J Allison, K Amako, J Apostolakis, P Arce, M Asai, T Aso, E Bagli, A Bagulya, S Banerjee, G Barrand, et al. Recent developments in geant4. *Nuclear Instruments and Methods in Physics Research Section A: Accelerators, Spectrometers, Detectors and Associated Equipment*, 835: 186–225, 2016.

John Allison, K Amako, J e a1 Apostolakis, HAAH Araujo, P Arce Dubois, MAAM Asai, GABG Barrand, RACR Capra, SACS Chauvie, RACR Chytracek, et al. Geant4 developments and applications. *Nuclear Science, IEEE Transactions on*, 53(1):270–278, 2006.

Gautam D Badhwar. Martian radiation environment experiment (marie). *Space Science Reviews*, 110(1-2):131–142, 2004.

Niels Bohr. Lx. on the decrease of velocity of swiftly moving electrified particles in passing through matter. *The London, Edinburgh, and Dublin Philosophical Magazine and Journal of Science*, 30(178):581–612, 1915.

Thomas B Borak, Lawrence H Heilbronn, Lawrence W Townsend, Rafe A McBeth, and Wouter de Wet. Quality factors for space radiation: A new approach. *Life Sciences in Space Research*, 1:96–102, 2014.

PD Bradley and Anatoly B Rosenfeld. Tissue equivalence correction for silicon microdosimetry detectors in boron neutron capture therapy. *Medical Physics*, 25(11):2220–2225, 1998.

Murray Campbell, A Joseph Hoane, and Feng-hsiung Hsu. Deep blue. *Artificial intelligence*, 134 (1-2):57–83, 2002.

CERN. Medipix. URL http://medipix.web.cern.ch/medipix/.

RBE Committee et al. Report of the rbe committee to the international commissions on radiological protection and on radiological units and measurements. *Health Physics*, 9:357, 1963.

Francis A Cucinotta. Space radiation risks for astronauts on multiple international space station missions. *PloS one*, 9(4):e96099, 2014.

Francis A Cucinotta, MY Kim, and Lori J Chappell. Space radiation cancer risk projections and uncertainties–2012. *NASA TP*, 2013.

Marco Durante. Eighth warren k. sinclair keynote address: heavy ions in therapy and space: benefits and risks. *Health physics*, 2012.

Marco Durante. Space radiation protection: destination mars. *Life sciences in space research*, 1: 2–9, 2014.

Marco Durante and Francis A Cucinotta. Heavy ion carcinogenesis and human space exploration. *Nature Reviews Cancer*, 8(6):465–472, 2008.

Marco Durante and Francis A Cucinotta. Physical basis of radiation protection in space travel. *Reviews of Modern Physics*, 83(4):1245, 2011.

Geant4. Geant4. URL http://geant4.web.cern.ch/geant4/.

Douglas Grahn. *HZE particle effects in manned spaceflight*. National Academy of sciences, 1973.

Susanna Guatelli, Mark I Reinhard, B Mascialino, Dale A Prokopovich, Andrew S Dzurak, M Zaider, and Anatoly B Rosenfeld. Tissue equivalence correction in silicon microdosimetry for protons characteristic of the leo space environment. *IEEE Transactions on Nuclear Science*, 55(6):3407–3413, 2008.

P Gueth, D Dauvergne, N Freud, JM Létang, C Ray, E Testa, and D Sarrut. Machine learning-based patient specific prompt-gamma dose monitoring in proton therapy. *Physics in medicine and biology*, 58(13):4563, 2013.

Sarah L Gulliford, Steve Webb, Carl G Rowbottom, David W Corne, and David P Dearnaley. Use of artificial neural networks to predict biological outcomes for patients receiving radical radiotherapy of the prostate. *Radiotherapy and oncology*, 71(1):3–12, 2004.

DM Hassler, C Zeitlin, RF Wimmer-Schweingruber, S Böttcher, C Martin, J Andrews, E Böhm, DE Brinza, MA Bullock, S Burmeister, et al. The radiation assessment detector (rad) investigation. *Space science reviews*, 170(1-4):503–558, 2012.

S Hoang, L Pinsky, R Vilalta, and J Jakubek. Let estimation of heavy ion particles based on a timepix-based si detector. In *Journal of Physics: Conference Series*, volume 396, page 022023. IOP Publishing, 2012.

S Hoang, R Vilalta, L Pinsky, M Kroupa, N Stoffle, and J Idarraga. Data analysis of tracks of heavy ion particles in timepix detector. In *Journal of Physics: Conference Series*, volume 523, page 012026. IOP Publishing, 2014.

Son M Hoang. *A Pattern Recognition Approach to Learning Tracks of Heavy-ion Particles in Timepix Detectors*. PhD thesis, 2013.

Kathryn Hurlbert, Bob Bagdigian, Carol Carroll, Antony Jeevarajan, Mark Kliss, and Bhim Singh. Human health, life support and habitation systems, 2012.

ICRP. *Recommendation of the ICRP*. ICRP Publication 26, 1977.

ICRP. *1990 Recommendation of the ICRP*. ICRP Publication 60, 1990.

ICRP. Relative biological effectiveness (rbe), quality factor (q), and radiation weighting factor (w_r): Icrp publication 92. *Annals of the ICRP*, 33(4):1–121, 2003.

ICRU. Report 85. *Journal of the ICRU*, 11(1):NP, 2011.

Linear Energy Transfer ICRU. Report 16. *International Commission on Radiation Units and Measurements, Bethesda, MD*, 1970.

Quantities ICRU. Units in radiation protection dosimetry. *ICRU Report No. 51*, 1993.

Anton V Ivantchenko, Vladimir N Ivanchenko, Jose-Manuel Quesada Molina, and Sebastien L Incerti. Geant4 hadronic physics for space radiation environment. *International journal of radiation biology*, 88(1-2):171–175, 2012.

Eric Jones, Travis Oliphant, Pearu Peterson, et al. SciPy: Open source scientific tools for Python, 2001–. URL http://www.scipy.org/.

Lars J Kangas, Paul E Keller, Edward R Siciliano, Richard T Kouzes, and James H Ely. The use of artificial neural networks in pvt-based radiation portal monitors. *Nuclear Instruments and Methods in Physics Research Section A: Accelerators, Spectrometers, Detectors and Associated Equipment*, 587(2):398–412, 2008.

Iwan Kawrakow. The monte carlo simulation of radiation transport. In *AAPM Conference Presentation*, 1999.

Chiara La Tessa, S Guetersloh, L Heilbronn, Jack Miller, Lembit Sihver, and Cary Zeitlin. Fragmentation of 1gev/nucleon iron ions in thick targets relevant for space exploration. *Advances in Space Research*, 35(2):223–229, 2005.

L. Landau. On the energy loss of fast particles by ionization. *J. Phys.(USSR)*, 8:201–205, 1944.

KT Lee, Victor Andersen, Lawrence Pinsky, Cary Zeitlin, Tim Cleghorn, Francis Cucinotta, Premkumar Saganti, William Atwell, and Ron Turner. Cosmic ray flux measurements made by marie in mars orbit. In *International Cosmic Ray Conference*, volume 4, page 1769, 2003.

Xavier Llopart, Michael Campbell, D San Segundo, E Pernigotti, and R Dinapoli. Medipix2, a 64k pixel read out chip with 55/spl mu/m square elements working in single photon counting mode. In *Nuclear Science Symposium Conference Record, 2001 IEEE*, volume 3, pages 1484–1488. IEEE, 2001.

Xavier Llopart, Rafael Ballabriga, Michael Campbell, Lukas Tlustos, and Winnie Wong. Timepix, a 65k programmable pixel readout chip for arrival time, energy and/or photon counting measurements. *Nuclear Instruments and Methods in Physics Research Section A: Accelerators, Spectrometers, Detectors and Associated Equipment*, 581(1):485–494, 2007.

Howard D Maccabee, Mudundi R Raju, and Cornelius A Tobias. Fluctuations of energy loss by heavy charged particles in thin absorbers. *Physical Review*, 165(2):469, 1968.

R McBeth and T Borak. Su-e-t-709: Spatial resolution requirements for fragment identification in a carbon ion spread out bragg peak. *Medical Physics*, 42(6):3500–3500, 2015. ISSN 2473-4209. doi: 10.1118/1.4925073. URL http://dx.doi.org/10.1118/1.4925073.

Nicholas Metropolis. The beginning of the monte carlo method. *Los Alamos Science*, 15(584): 125–130, 1987.

NCRP. *National Council on Radiation Protection and Measurements: Guidance on Radiation Received in Space Activities*. NCRP Report No. 98, 1989.

NCRP. *National Council on Radiation Protection and Measurements: Limitation of Exposure to Ionizing Radiation*. NCRP Report No. 116, 1993.

NCRP. *National Council on Radiation Protection and Measurements: Radiation Protection Guidance for Activities in Low-Earth Orbit*. NCRP Report No. 132, 2000.

NCRP. *National Council on Radiation Protection and Measurements: Operational Radiation Safety Program for Astronauts in Low-Earth Orbit: A Basic Framework*. NCRP Report No. 142, 2002.

NCRP. *National Council on Radiation Protection and Measurements: Information Needed to Make Radiation Protection Recommendations for Space Missions Beyond Low-earth Orbit*. NCRP Report No. 153, 2006.

NCRP. *National Council on Radiation Protection and Measurements: Radiation Protection For Space Activities: Supplement to Previous Recommendations*. NCRP Commentary No. 23, 2014.

Jennifer L Parsons and Lawrence W Townsend. Interplanetary crew dose rates for the august 1972 solar particle event. *Radiation research*, 153(6):729–733, 2000.

F. Pedregosa, G. Varoquaux, A. Gramfort, V. Michel, B. Thirion, O. Grisel, M. Blondel, P. Prettenhofer, R. Weiss, V. Dubourg, J. Vanderplas, A. Passos, D. Cournapeau, M. Brucher, M. Perrot, and E. Duchesnay. Scikit-learn: Machine learning in Python. *Journal of Machine Learning Research*, 12:2825–2830, 2011.

Lawrence Pinsky, Nicholas Stoffle, Anton Empl, Jan Jakubek, Stanislav Pospisil, Claude Leroy, Hisashi Kitamura, Nakahiro Yasuda, and Yukio Uchihori. Application of the medipix2 technology to space radiation dosimetry and hadron therapy beam monitoring. *Radiation Measurements*, 46(12):1610–1614, 2011a.

Lawrence S Pinsky and Jeffrey Chancellor. Development of a new active personal dosimeter for use in space radiation environments. In *Aerospace Conference, 2007 IEEE*, pages 1–4. IEEE, 2007.

Lawrence S Pinsky, Anton Empl, Andrea Gutierrez, Jan Jakubek, Hisashi Kitamura, Jack Miller, Claude Leroy, Nicholas Stoffle, Stanislav Pospisil, Yukio Uchihori, et al. Penetrating heavy ion charge and velocity discrimination with a timepix-based si detector (for space radiation applications). *Nuclear Instruments and Methods in Physics Research Section A: Accelerators, Spectrometers, Detectors and Associated Equipment*, 633:S190–S193, 2011b.

Arthur L Samuel. Some studies in machine learning using the game of checkers. *IBM Journal of research and development*, 3(3):210–229, 1959.

Harlan E Spence, AW Case, MJ Golightly, T Heine, BA Larsen, JB Blake, P Caranza, WR Crain, J George, M Lalic, et al. Crater: The cosmic ray telescope for the effects of radiation experiment on the lunar reconnaissance orbiter mission. *Space science reviews*, 150(1-4):243–284, 2010.

N Stoffle, L Pinsky, S Hoang, J Idarraga, M Kroupa, J Jakubek, D Turecek, and S Pospíšil. Initial results on charge and velocity discrimination for heavy ions using silicon-timepix detectors. *Journal of Instrumentation*, 7(12):C12009, 2012.

Min Su, Moyed Miften, Curtis Whiddon, Xuejun Sun, Kim Light, and Lawrence Marks. An artificial neural network for predicting the incidence of radiation pneumonitis. *Medical physics*, 32(2):318–325, 2005.

Alan M Turing. Computing machinery and intelligence. *Mind*, 59(236):433–460, 1950.

PV Vavilov. Ionization losses of high-energy heavy particles. *Soviet Phys. JETP*, 5, 1957.

R Vilalta, S Kuchibhotla, R Valerio, and L Pinsky. Development of pattern recognition software for tracks of ionizing radiation in medipix2-based (timepix) pixel detector devices. In *Journal of Physics: Conference Series*, volume 331, page 032052. IOP Publishing, 2011.

Zdenek Vykydal and Jan Jakubek. Usb liteâĂŤminiaturized readout interface for medipix2 detector. *Nuclear Instruments and Methods in Physics Research Section A: Accelerators, Spectrometers, Detectors and Associated Equipment*, 633:S48–S49, 2011.

C Zeitlin, T Cleghorn, F Cucinotta, P Saganti, V Andersen, K Lee, L Pinsky, W Atwell, and R Turner. Results from the martian radiation environment experiment marie. In *Lunar and Planetary Science Conference*, volume 34, 2003.

C Zeitlin, T Cleghorn, F Cucinotta, P Saganti, V Andersen, K Lee, L Pinsky, W Atwell, R Turner, and G Badhwar. Overview of the martian radiation environment experiment. *Advances in Space Research*, 33(12):2204–2210, 2004.

C Zeitlin, W Boynton, I Mitrofanov, D Hassler, W Atwell, TF Cleghorn, FA Cucinotta, M Dayeh, M Desai, SB Guetersloh, et al. Mars odyssey measurements of galactic cosmic rays and solar particles in mars orbit, 2002–2008. *Space Weather*, 8(11), 2010.

C Zeitlin, DM Hassler, FA Cucinotta, B Ehresmann, RF Wimmer-Schweingruber, DE Brinza, S Kang, G Weigle, S Böttcher, E Böhm, et al. Measurements of energetic particle radiation in transit to mars on the mars science laboratory. *Science*, 340(6136):1080–1084, 2013.

Cary Zeitlin and Chiara La Tessa. The role of nuclear fragmentation in particle therapy and space radiation protection. *Frontiers in oncology*, 6, 2016.

Glossary

coincident A coincident event occurs when one or more particles intercept a detection system simultaneously.For this work, all particles generated from a same incident ion are considered to hit the detector at the same time.

fragment A secondary particle generated from interaction of the primary ions. Fragments can be produced from the primary ion, e.g., carbon (Z = 6) ion breaking into two helium ions (Z = 2) and two protons (Z = 1), or a target fragment, e.g. aluminum (Z = 13) in shielding creating a nitrogen (Z=7) and carbon ion (Z=6). Secondary fragments can also produce their own secondary particles when they interact.

idealized detector system A detector system created to investigate various physical phenomena that does not include the effects of an actual detector system. In the idealized system stopping power values are found by capturing the particle with the virtual detector and looking up the stopping power results from Geant4 tabulated values.

incident ion The primary ion of the simulation. These ions are incident generated with specific kinetic energy, e.g., 300 MeV/n, 900 MeV/n or 2400 MeV/n and directed at the Aluminum shielding at a 90 degree angle to the surface.

particle identification detector system A detector system created to investigate the ability to perform particle identification based on energy deposition in a real detector

physical detector system A detector system created to investigate the effects of introducing a detector system with physical parameters, i.e., thickness, density, mass. In the physical detector system stopping power values are found by recording the energy deposited in the real detector.

real detector A detector that has physical properties and interacts with particles as they pass through. This type of detector is used to record particle parameters as they intercept as well as energy deposition in the physical dimensions of the detector.

virtual detector A detector that has no physical properties and does not interact with particles as they pass through. This type of detector is used to record particle parameters as they intercept but it cannot record energy deposition due to the detector having no physical properties, i.e., mass, density, thickness.